

COLLABORATIVE RESEARCH: HIGH-RESOLUTION SEISMIC VELOCITY AND ATTENUATION MODELS OF WESTERN CHINA

Eric Sandvol, et al.

**Department of Geological Science
University of Missouri
Columbia, MO 65211**

20 July 2014

Final Report

APPROVED FOR PUBLIC RELEASE; DISTRIBUTION IS UNLIMITED.



**AIR FORCE RESEARCH LABORATORY
Space Vehicles Directorate
3550 Aberdeen Ave SE
AIR FORCE MATERIEL COMMAND
KIRTLAND AIR FORCE BASE, NM 87117-5776**

DTIC COPY

NOTICE AND SIGNATURE PAGE

Using Government drawings, specifications, or other data included in this document for any purpose other than Government procurement does not in any way obligate the U.S. Government. The fact that the Government formulated or supplied the drawings, specifications, or other data does not license the holder or any other person or corporation; or convey any rights or permission to manufacture, use, or sell any patented invention that may relate to them.

This report was cleared for public release by the 377 ABW Public Affairs Office and is available to the general public, including foreign nationals. Copies may be obtained from the Defense Technical Information Center (DTIC) (<http://www.dtic.mil>).

AFRL-RV-PS-TR-2014-0187 HAS BEEN REVIEWED AND IS APPROVED FOR PUBLICATION IN ACCORDANCE WITH ASSIGNED DISTRIBUTION STATEMENT.

//SIGNED//

Robert Raistrick
Project Manager, AFRL/RVBYE

//SIGNED//

Glenn M. Vaughan, Colonel, USAF
Chief, Battlespace Environment Division

This report is published in the interest of scientific and technical information exchange, and its publication does not constitute the Government's approval or disapproval of its ideas or findings.

This page is intentionally left blank.

Table of Contents

1. Summary	1
2. Introduction	2
2.1. Tectonic Setting	2
2.2. Attenuation (Q) Tomography	6
3. Methodology	8
3.1. Two Plane Wave Tomography (TPWT).....	8
3.2. Pn and Sn Travel Time Tomography	12
3.3. Two and Reverse Two Station Q Tomography	12
3.4. Q-Anisotropy Method.....	18
3.5 Catalog Amplitude Tomography (ML tomography)	23
3.6 Joint Inversion of Receiver Functions and Surface Waves	24
4. Results and Discussion	25
4.1. Two Plane Wave Rayleigh Wave Tomography.....	25
4.2. Pn and Sn Travel Time Tomography	33
4.3. Lg and Pg Q Tomography	41
4.4. Sn Q Tomography (Tibet and Northeastern China)	54
4.5. ML Amplitude Tomography	67
4.6 Joint Inversion of Receiver Functions and Surface Wave Dispersion Curves.....	69
5. Conclusions.....	73
5.1. Seismic Velocity Studies.....	73
5.2. Interpretation of the Pn and Sn Tomography	74
5.3. Q Tomography	76
References.....	78
List of Symbols, Abbreviations, and Acronyms	87

Figures

1. Rayleigh wave phase dispersion curves from northern and southern Tibet.	2
2. A simple tectonic map for the Tibetan Plateau.	3
3. A plot of seismic stations in the NETS(blue) and ASCENT (green) broadband arrays.....	5
4. A plot of the NECESS broadband array.	5
5. Lg Q estimates using spectral methods and attenuation (Q) tomography (Xie et al., 2006).	6
6. Q estimated using 1-Hz Lg amplitudes obtained from digital waveform data (Phillips et al., 2005).	7
7. A schematic of local Cartesian coordinate system.	9
8. Map views of amplitude and phase sensitivity kernels for 20 mHz Rayleigh waves, obtained using the Born approximation.	10
9. Schematic drawing of the geometry of RTS and RTE.	14
10. A resolution test to determine whether we are able to resolve azimuthal Q anisotropy given our reverse two station path coverage.....	22
11. An example of the grid search result on the co-influence of damping factors λ_1 and λ_2 on the residual ratios of isotropic and anisotropic coefficients A and B when (a) no random noise, (b) 15% random noise, and (c) 25% random noise are added, respectively. .	23
12. The difference between isotropic phase velocities obtained using ambient noise tomography (ANT) [Yang et al., 2010] and two-plane wave approach (TWPT) for periods of a) 25, b) 30, and c) 40 s.	26
13. Ray path coverage for each period (T) with the number of events (N). Isotropic phase velocities are stable for $T \geq 25$ s (the periods with $N \geq 60$ earthquakes).	27
14. The resolution test results for different periods using checkerboard synthetic model. ..	28
15. Anisotropic phase velocity maps for 12 periods (22-143 s).	29
16. Shear wave velocities (km/s) for depths between 30 and 210 km.	30
17. Standard Error (left vertical axis) vs. period for different damping parameter values..	32

18. Our final tomographic Pn velocity model for ray paths between 3 and 15 degrees using data from the Chinese National catalog as well as picks from all temporary stations deployed throughout the Tibetan plateau.	33
19. Our final list of average station delays for all stations used to construct the tomographic model shown in Figure 18.	34
20. Our final tomographic Pn velocity model for ray paths between 3 and 9 degrees.	35
21. Our final tomographic Pn velocity model for ray paths between 6 and 12 degrees.	35
22. Our final tomographic Pn velocity model for ray paths between 9 and 15 degrees.	36
23. A map of eastern Tibet showing the major physiographic features (left) and a plot of the ray path coverage where we observe both Pn and Sn arrival times (Lü et al, 2012).	37
24. Sn lateral velocity variations for the uppermost mantle layer. The average Sn velocity is 4.60 km/s.	38
25. Pn lateral velocity variations for the uppermost mantle layer. Average Pn velocity is 8.10 km/s.	38
26. A tomographic model of the V_p/V_s ratio for the uppermost mantle beneath eastern Tibet and the surrounding regions.	39
27. Map showing seismic stations, regional seismic events, and two-station or two-event paths in this study.	41
28. Q_{Lg} (a) and Q_{Pg} (b) tomographic images at 1 Hz.	43
29. Models of Q_{Lg} at 0.5 Hz (a), 1 Hz (b), and 2 Hz (c).	44
30. Lg site term maps at frequencies of 0.5 Hz (a), 1 Hz (b), and 2 Hz (c).	46
31. The linear relationship between normalized logarithmic source terms solved from Lg RTM and magnitude M_L	48
32. Examples of the RTM $1/Q_{Lg} \sim \varphi$ correlation.	49
33. Imaged variations of isotropic Q ($1/A$), anisotropy magnitude (B), and high- Q direction (θ) in the crust of eastern Tibetan Plateau at different frequencies of (a) 0.6 Hz, (b) 0.8 Hz, (c) 1 Hz, and (d) 1.2 Hz.	50
34. Comparison of azimuthal anisotropy of $1/Q_{Lg}$, for different frequencies, in the eastern Tibetan Plateau.	51

35. Sn efficiency map for Tibet with all efficient paths shown on top of the blocked and inefficient paths.	55
36. Sn Q tomography of northeastern Tibet at 1 Hz.	56
37. Top: RTM Sn Q tomography of northeastern Tibet at 1 Hz; Bottom: RTM Sn Q tomography of northeastern Tibet at 0.5 Hz.	57
38. A map shows the Sn raypaths across northeastern China using broadband data from the NECESS array.....	58
39. Sample record section for an earthquake occuring along the Pacific subduction zone.	59
40. A map of the reverse two-station SN raypaths for the NECESS array.....	60
41. An example of linear regression fitting for interstation RTM Q_0 values for the same station pair NE79-NEA2.....	61
42. RTM Sn Q map at 1 Hz with cell size of $0.5^\circ \times 0.5^\circ$	62
43. Checkerboard test with a $2^\circ \times 2^\circ$ cells using 3000 reverse two-station paths.	63
44. Sn Q at (a) 0.5 Hz and (b) 2.0 Hz with $0.5^\circ \times 0.5^\circ$ cells.	64
45. Our percentage error of Sn Q at 1 Hz across our study region.	65
46. The error for the Q frequency dependence term η across our study region	66
47. Log amplitude versus offset for the raw data set before selection.....	67
48. Tomographic image of Q across Tibet using amplitudes from the Chinese Earthquake Bulletin.....	68
49. Relative station terms for the tomography.....	69
50. The results of one of our Joint Inversions for station C001.	71
51. Our Moho map generated from the optimal 1-D velocity models from 70 stations across northeastern Tibet.	72
52. A rough quantitative comparison of the overlapping regions of the body and surface wave models of the shear wave velocity.	73

1. SUMMARY

Development of high-resolution seismic velocity and attenuation models in the Qinghai-Tibetan plateau and adjacent regions of western China are critical to monitoring efforts because of their close proximity (~380 km) to the nuclear test site at Lop Nor. In this project we have been able to construct and validate attenuation models for the crust and upper mantle in western China. Previous studies have demonstrated the great complexity in crustal and uppermost mantle seismic velocity structure and propagation characteristics beneath much of the Qinghai-Tibet plateau and the surrounding regions. Regional seismic phases show strong lateral variability in traveltimes, amplitude, and frequency content due to this very complex structure. Due to a lack of two-dimensional seismic array data, the three-dimensional seismic structure and propagation characteristics of the crust, lithosphere and upper mantle have been largely unknown. We have helped to remedy this problem using data from relatively new broadband stations in the region, which unlike the previous, linear, seismic transects, covered most of the northeastern portion of the Qinghai-Tibet plateau in a semi-regularly spaced grid. Using data collected by PI's on the NETS (NorthEastern Tibet Seismic experiment) and ASCENT (A Seismic Collaborative Experiment of Northern Tibet) arrays (5/07-6/09) which consisted of more than 110 temporary broadband stations in the northeast Tibetan Plateau, Ordos Plateau, and Qaidam basin, and using a comprehensive set of techniques, we have developed new seismic velocity and attenuation models. Furthermore we have integrated data from the MIT temporary array along with data from the Namche Barwa arrays. These new data sets allow the application of new techniques designed to create robust models of seismic velocity and attenuation in which we reliably estimate the absolute amplitude of the velocity and Q variations across western China.

We have been able to leverage existing resources to significantly extend our work beyond what we proposed to deliver originally. We have extended our regional phase attenuation work to include Northeastern China. Northeast China is a tectonically active continental craton that has been re-activated by Pacific plate subduction and India-Eurasia collision. We have extended the work on Sn propagation in eastern Tibet to regional phase Sn wave propagation across northern China where high frequency Sn is more prevalent and thus allows us to study in more detail high frequency Sn propagation. The temperature and the corresponding anelastic variations in the uppermost mantle are determined by calculating Sn Q. We have collected waveform data recorded by 127 stations from 140 earthquakes in a rectangular region from 30°N to 60°N in latitude, 100°E to 145°E in longitude. We have obtained models of Sn Q for northeast China using two methods: two station method (TSM) and the reverse two-station method (RTM). The former method measurements are contaminated with any relative changes in site effect between two stations, whereas the latter are not and are likely more robust in an absolute sense. The inversion results show high Q values in the Songliao basin, indicating relatively low temperature and low viscosity for its uppermost mantle. Checkerboard resolution shows good resolution at a scale of $2^\circ \times 2^\circ$ within most of the study area.

2. INTRODUCTION

2.1 Tectonic Setting

Western China around the Lop Nor test site has been the focus of many studies related to seismic wave propagation and velocity structure [e.g. Li et al., 2008; Tilman et al., 2003; Mitchell, 1997; Rodgers et al., 1997; Rapine et al. 2003b; McNamara et al., 1997]. Here we summarize some of the current state-of-the-art knowledge of the seismic structure of the Tibetan plateau and its relationship to tectonic hypotheses.

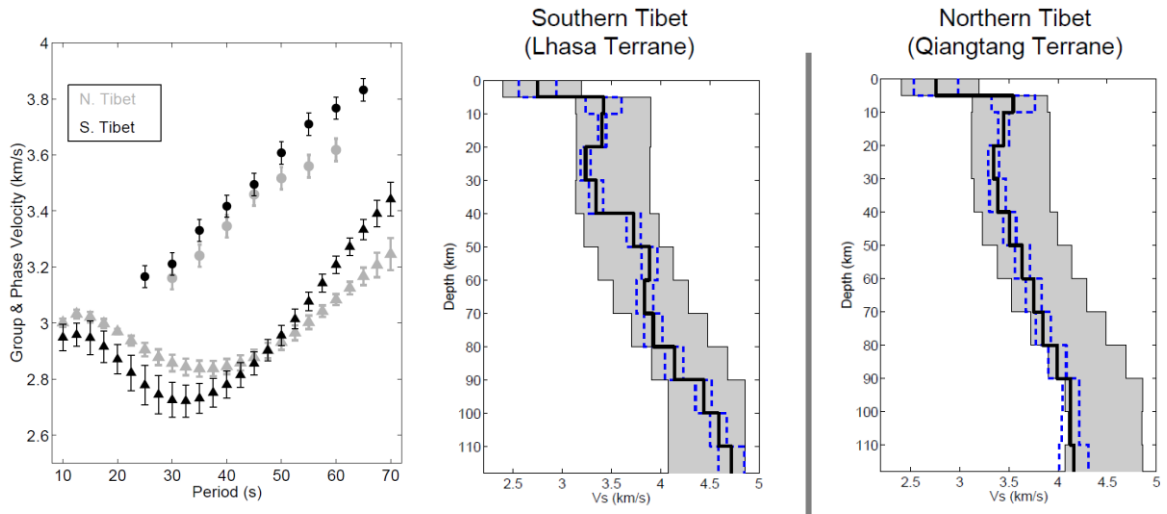


Figure 1. Rayleigh wave phase dispersion curves from northern and southern Tibet. *Diamonds indicate group velocities and circles indicate phase velocities. Notice the divergence in the dispersion curves at approximately 60 second period. This is most likely a result of anomalously slow velocities in the uppermost mantle beneath northern Tibet (Rapine et al., 2003b).*

Body wave and surface wave studies have indicated a seismically slow and highly attenuating uppermost mantle for much of northern Tibet [Ni and Barazangi, 1983; McNamara et al., 1997; Rapine et al., 2003a]. In contrast, in southern Tibet and the Qaidam basin (north of Kunlun fault), colder mantle has been implied [e.g. Ni and Barazangi, 1983; Tilmann et al., 2003; Galve et al., 2002; Li et al., 2008] (Figure 2). Tilmann et al., [2003] successfully imaged the downwelling Indian lithosphere to depths near 400 km beneath central Tibet. This result along with the recent P-wave tomography images of the Tibetan plateau indicate that the Indian continental lithosphere underlies southern Tibet and an estimated minimum of 1000 km of post-collisional convergence between India and Asia has occurred. The Indian lower crust and lithosphere underthrust the Himalayas and southern Tibet without significant internal deformation [e.g. Kind et al., 2002; Tilmann, et al., 2003; Kumar et al., 2006]. In southern Tibet a variety of seismic observations [Makovsky and Klemperer, 1999; Yuan et al., 1997; Kind et al., 2002; Tilmann, et al., 2003; Huang and Zhao; 2006; Li et al., 2008] and electrical conductivity [e.g. Wei et al., 2001] all point to a weak low-velocity middle crust underlain by a strong Indian lithosphere [Nelson et al., 1996]. The predominant cause of

this low-viscosity and low-velocity channel in the mid-crust is wet melting of the subducted Indian sediments and metasediments [Nelson et al., 1996; Cotte et al., 1999; Rapine et al., 2003b]. Therefore, there is a large viscosity contrast vertically, and deformation is confined to a low-viscosity layer that may force lower crustal deformation to be primarily horizontal [Bendick and Flesch, 2007].

Another effect of the mid-crustal low velocity zone is the high attenuation of Lg waves in southern Tibet [McNamara et al., 1996; Reese et al., 1999; Xie, 2002a; Phillips et al., 2000, 2001, 2005]. In contrast, the crust beneath northern Tibet (Qiangtang terrane) is characterized by a monotonically increasing seismic velocity with about 8% lower average velocity than a normal continental crust [Rapine et al., 2003a] (Figure 2). Lg attenuation studies of northern Tibet indicate low Lg attenuation (Q less than 100 at 1 Hz). The reason for such low Lg attenuation is not completely understood, but it seems related to high temperature and a partially melted crust of northern Tibet [Hacker et al., 2000; Fan and Lay, 2003].

A maximum seismogenic thickness of 25 km [Langin et al., 2003] is observed for northern Tibet. The lithosphere thickness is about 140 km according to S-P converted phases [Kumar, et al., 2006]; however, it could be thinner in the interior of the northern Plateau. Rayleigh wave phase velocity inversion indicates a lithosphere thickness of only about 120-140 km thick.

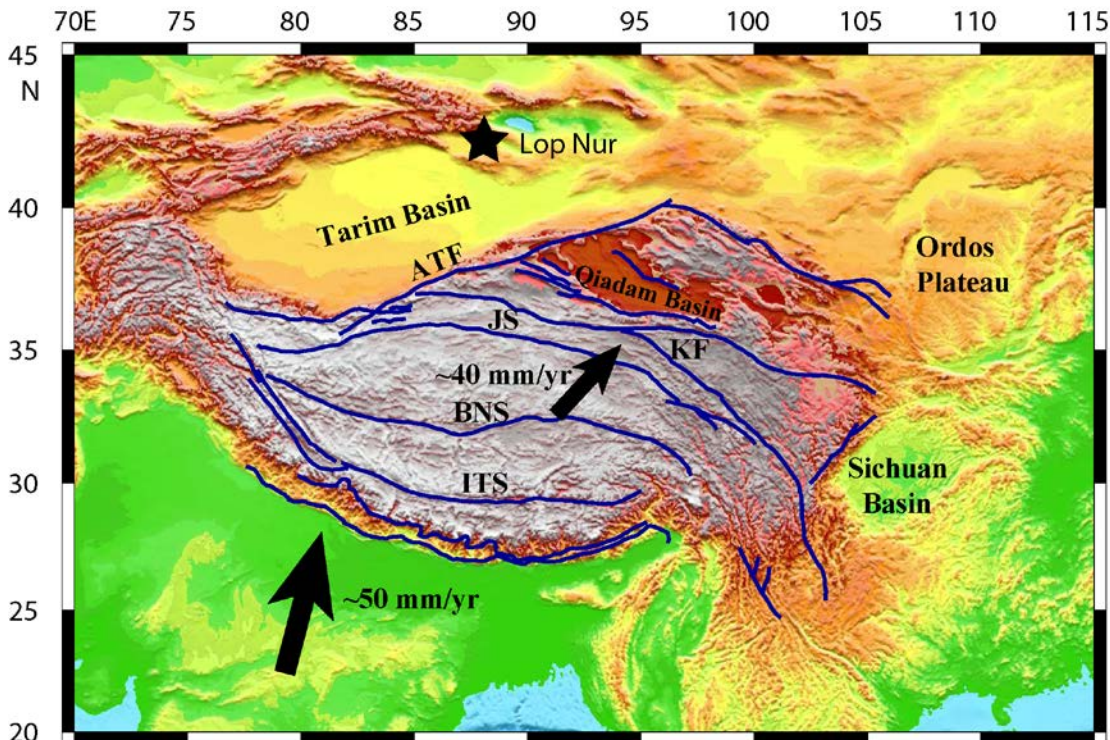


Figure 2. A simple tectonic map for the Tibetan Plateau. The major features shown are ITS- Indus Tsangpo Suture, BNS-Bangong-Nujiang Suture, ATF-Altyn Tagh Fault, KF-Kunlun Fault.

A consequence of the subduction of Indian continental lithosphere in central Tibet is that the downwelling of lithospheric material inevitably would entrain neighboring

asthenospheric materials along which would be induced a downward flow. This downwelling, combined with tentative evidence for southward-directed subduction of the Qaidam block along the northern plateau margin [Tapponnier et al., 2001; Kind et al., 2002], will likewise induce a downward flow. A deficit of asthenosphere must be compensated for by a focused upward return-flow. Such an upward flow would provide an explanation for a low-velocity body imaged by Wittlinger et al. [1996] and the recent volcanism just south of the Kunlun Mountains, and a mechanism for heating the crust and gradual erosion of the remaining Asian lithosphere beneath northern Tibet. Tilmann et al.'s (2003) P-wave tomography image offers only a glimpse of the mantle structure beneath the southern Qiangtang Terrane.

The Qaidam Basin (Figure 3) is a low relief intermontane basin that is probably underlain by relatively thick lithospheric mantle. The sediments in the basin probably are up to 14 km thick (Wang and Coward, 1990). The southern margin of the Qaidam basin is marked by the North Kunlun fault zone which is the major thrust front along the southern edge of the basin where there appear to be very abrupt changes in crustal thickness (~15 km) (e.g. Zhu and Helmberger, 1998). The northeastern edge of deformation of the Tibet plateau is arguably represented by the fold-thrust belts of the Qilian Shan and appears to mark a transition from relatively warm and seismically slow lithospheric mantle of the Qiangtang Terrane to colder and seismically fast lithospheric mantle beneath the Qaidam basin and possibly the Qilian Shan fold and thrust belts.

Dominating the northwestern margin of both the Qaidam Basin and the Tibetan Plateau proper is the Altyn Tagh fault (Figure 3). In scale (1200 km long) and geometry, the Altyn Tagh suggests a truly intracontinental equivalent to the great transform faults like the San Andreas. The Altyn Tagh consists of many strands, not all of which are currently active (e.g. Cowgill et al., 2003). Thrust structures of the Qaidam-Qilian terranes show little evidence of being distorted by the Altyn Tagh, suggesting that the former are stronger than the fault zone (Yin et al., 2008). Although some have argued that the Altyn Tagh is essentially a crust fault, detached from the underlying mantle by a decollement (e.g. Burchfiel et al., 1989), recent seismic tomography has been used to argue that it penetrates to about 140 km (Wittlinger et al., 1996). Quaternary basaltic volcanism near the western Altyn Tagh also suggests a deeply penetrating structure in that region, while the lack of such volcanism adjacent to the Qaidam terrane could be construed as evidence for the lack of deep penetration along its northeastern reaches (e.g. Yin et al., 2008).

All of these terrain sutures are near the Lop Nor test site, which is directly to the northwest of our array. This results in an incredibly heterogeneous lithospheric seismic velocity structure that represents a challenge not only to travel time calibration and seismic event determination but also to amplitude calibration efforts. In this project we have greatly improved the ability to predict both travel times and seismic amplitudes for the purposes of seismic event discrimination in western China.

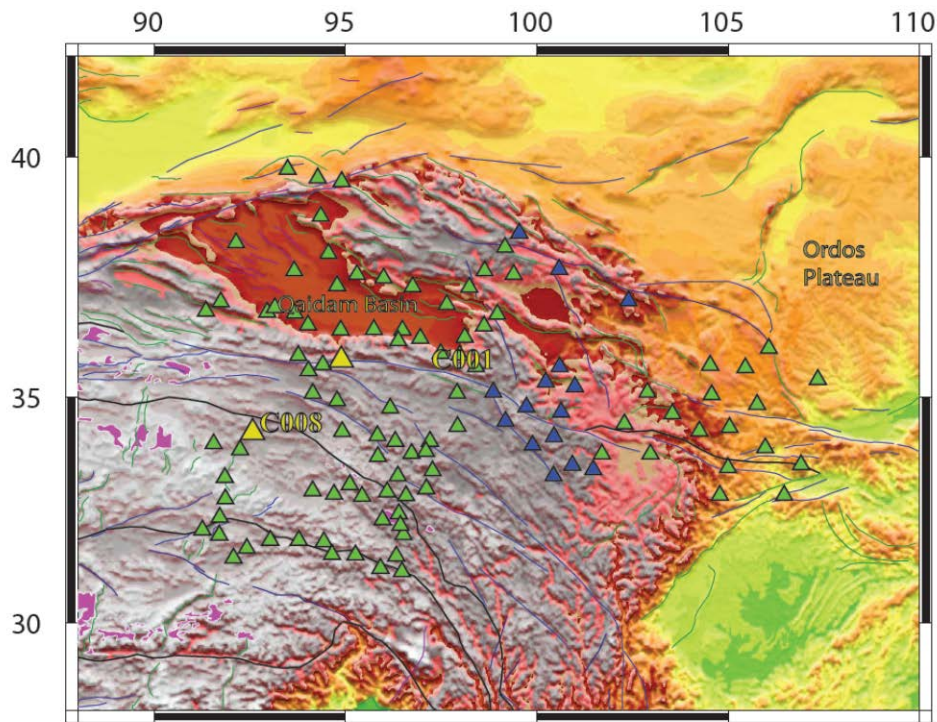


Figure 3. A plot of seismic stations in the NETS(blue) and ASCENT (green) broadband arrays.

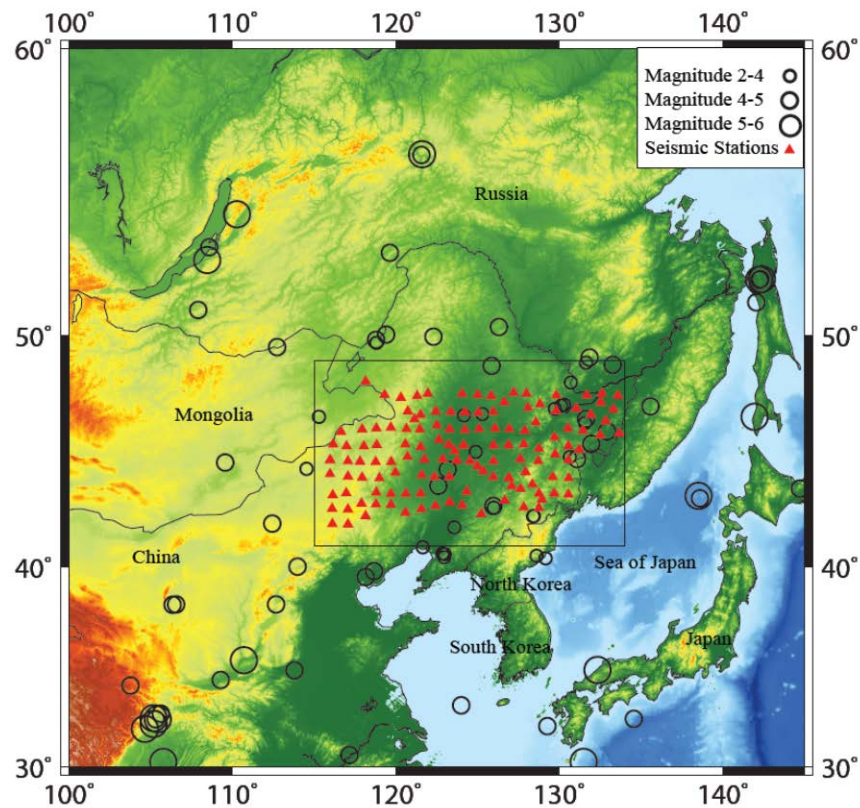


Figure 4. A plot of the NECESS broadband array.

2.2 Attenuation (Q) Tomography

Attenuation tomography uses estimates of path-averaged attenuation to delineate laterally varying Q . This includes most spectral methods (Zor et al., 2007). An example of attenuation tomography for Asia using coarsely spaced stations is shown in Figure 4 (Xie et al., 2006). We have used this method to create phase blockage maps for regions of the Middle East (Sandvol et al., 2001).

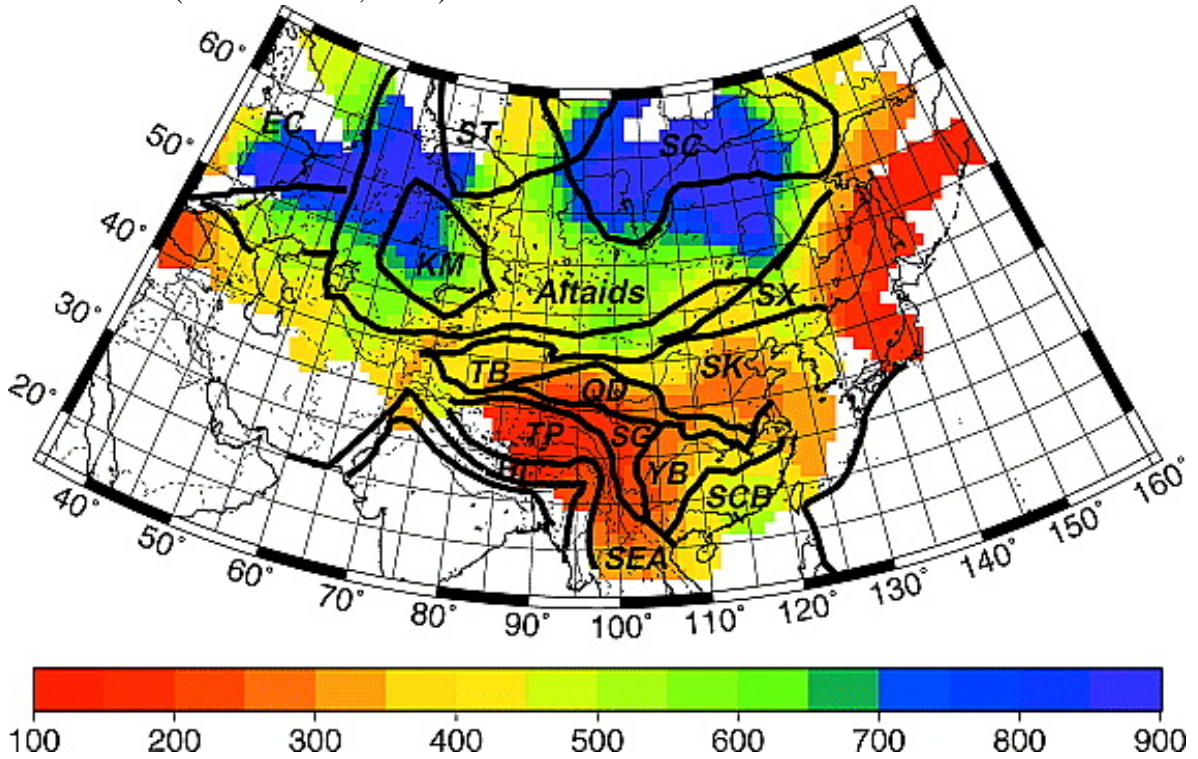


Figure 5. $L_g Q$ estimates using spectral methods and attenuation (Q) tomography (Xie et al., 2006). *This map is accompanied by a map of frequency dependence (not shown).*

Attenuation tomography relies on two-station methods for measuring inter-station Q , which cancel the source effect by using station pairs aligned with the source. These methods are relatively straightforward to apply, and are insensitive to source radiation pattern effects, but alignment requirements reduce the amount of data that can be used. We measure attenuation with the two-station (see Xie and Mitchell, 1990; Xie, 2002b; and Zor et al., 2007 for descriptions of the method, including rigorous error analysis) and reversed two station (Chun et al., 1987) methods. The reversed method eliminates site as well as source effects. Q_0 and η values measured using these methods are of very high quality because they are not subject to the trade-off between source and path parameters, and the smaller data sets can be easily scrubbed with the most rigorous quality control. Measured Q_0 and η values will be used to derive a long-wavelength Q map for the study region. This model can be subsequently used as a priori knowledge during amplitude tomography calculations. Alternately, inter-station Q measurements can be included as constraints in the amplitude tomography. Figure 5 shows a preliminary $L_g Q_0$ attenuation map using two station spectral ratios. Once again, ASCENT is ideally designed to tomographically map Q in this region with a high degree of resolution, and will increase resolution in surrounding areas when included in continental scale studies.

Amplitude tomography uses raw amplitudes rather than Q estimates, assumes an isotropic source radiation pattern, and solves for source and site terms in addition to 2-D attenuation. An example of amplitude based tomography for Asia is shown in Figure 6 from Phillips et al. (2005). The amplitude tomography method has proven successful and performs well even for lower quality data sets such as the surface-wave amplitudes archived by the International Seismological Centre (Hearn et al., 2008). Amplitude tomography does not require any special station geometry and can utilize many more raypaths. Constraints from high quality path averaged Q such as those described above can be incorporated into the inversion.

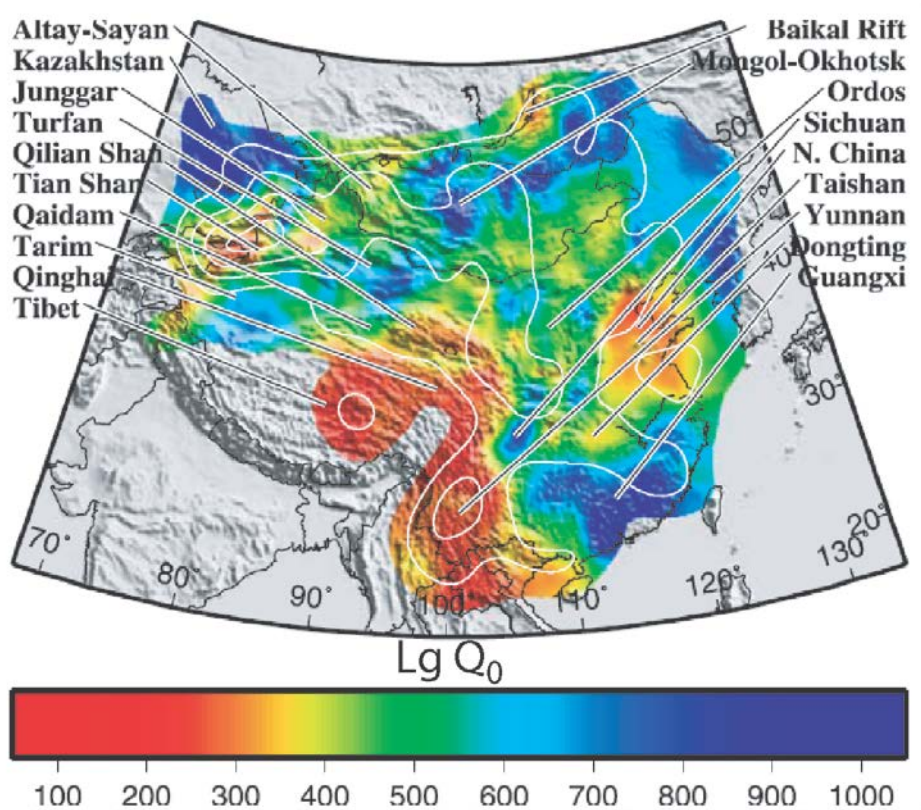


Figure 6 Q estimated using 1-Hz L_g amplitudes obtained from digital waveform data (Phillips et al., 2005). White contours represent the model resolution at levels of 0.1, 0.2, 0.3, and 0.4.

Attenuation causes substantial deviation of station magnitude from the true event magnitude. We have estimated typical ML magnitude corrections using our past tomography results based on 1 Hz peak-energy in the regional waves. These maps show that regional path corrections can be used to account for up to a full magnitude unit. Station gain terms can cause as much as half an additional magnitude unit correction. These are significant corrections from a monitoring viewpoint. Longer period waves, such as 10-20 seconds surface waves, produce proportionately smaller corrections due to

the influence of period on attenuation. Thus, the 10 second surface waves used to image surface-wave Q across China by Hearn et al. (2008), produce corrections of only a tenth of a magnitude unit at most, although the station corrections can again cause shifts of up to half a magnitude unit. Long-period amplitudes are less sensitive to Q variations (Fisk, 2006, 2007; Fisk et al., 2008) than short-period phases. Short-period phases however are essential to regional discrimination, and their use requires accurate attenuation corrections.

3. METHODOLOGY

We have used a large number of different techniques to construct attenuation and velocity images of eastern Tibetan and northeastern China; therefore it is necessary to discuss these approaches concisely.

3.1 Two Plane Wave Tomography (TPWT)

Seismic surface waves travel parallel to earth's surface, sampling different depths with a range of frequencies. Fundamental mode Rayleigh and Love waves are most sensitive to earth structure at depths corresponding to $\sim 1/3$ and $\sim 1/4$ of their dominant wavelengths, respectively (Knopoff et al., 1973). Surface waves are *dispersive*, i.e. relatively longer period surface waves have greater wavelengths, allowing them to travel through deeper parts of the earth at greater wave speeds. Using a range of frequencies, we can take advantage of surface wave dispersion to calculate phase and group wave speeds as a function of depth. These characteristics of surface waves make them valuable tools for studying earth structure in the crust and uppermost mantle.

One of the earliest attempts at measuring surface wave dispersion was the single station method. This method uses only well-dispersed records, relying heavily on the initial phases of waves generated by an earthquake. For this reason, the single station method requires precise knowledge of source parameters. Due to this limitation, it is often unreliable for measuring surface wave dispersion. A more traditional and widely applied technique is the two-station method. This method adapts an approach similar to travel time tomography, employing relative travel times of surface waves between two stations, lying approximately on the same great circle path (within the range of $\pm 15^\circ$). One advantage of this approach is ease of implementation, as the forward problem of surface wave propagation is reduced to seismic ray theory, which assumes seismic waves consist of infinite frequencies. However, surface waves have finite frequencies. Therefore, traditional surface wave tomography breaks down when the wavelengths of heterogeneities are similar to wavelengths of surface waves (Li, 2011; Zhou and Murphy, 2005). Additionally, lateral heterogeneities between events and seismic arrays may cause scattering and multipathing. Consequences of these finite frequency effects include distortion of ray paths and variations in amplitudes (Forsyth and Li, 2005). For these reasons, amplitude information is ignored in traditional methods. Moreover, since the traditional method requires stations to be on the same great circle path as events, not all the station-event pairs can be included in tomographic inversions. Therefore, resolution and robustness of phase velocity measurements are highly affected by number and spatial distribution of ray paths.

The Two Plane Wave Method TPWT (Forsyth et al., 1998) does not share these limitations. Rather, it uses both amplitude and phase variations, assuming that distortion of a wavefront at any location within a seismic array (i.e. receiver locations and inversion nodes) can be expressed as the sum of two plane waves (Forsyth et al., 1998; Forsyth and Li, 2005). This assumption can be expressed as follows:

$${}^k_i U = {}_i A_1 \exp(-i {}^k_i \phi_1) + {}_i A_2 \exp(-i {}^k_i \phi_2), \quad (1)$$

where U is the displacement at k^{th} station caused by i^{th} event, and A and ϕ are amplitudes and phases of two plane waves, respectively. Further, the phase (ϕ) terms in Equation (1) can be expressed as:

$${}^k_i \phi_{1,2} = {}^0_i \phi_{1,2} + \overline{{}^k_i S} \omega \{ {}^k_i r \cos({}^k_i \psi - {}_i \theta_{1,2}) - {}^k_i x \} - \omega({}^k_i \tau - {}^0_i \tau) \quad (2)$$

where ${}^0_i \phi_{1,2}$ represents phases of first and second plane waves at a reference station, and $\overline{{}^k_i S}$ is the average slowness. ${}^k_i \tau - {}^0_i \tau$ is the difference between travel times along the great circle path, measured from the edge of study area to the k^{th} and reference station. ${}_i \theta_{1,2}$ denotes deviation from the great circle path for both plane waves (Forsyth and Li, 2005). Hence, the wavefield at each station for a single frequency can be described by three unknowns for each plane wave: relative amplitudes and phases with respect to a reference station, and deviation angles from the great circle path.

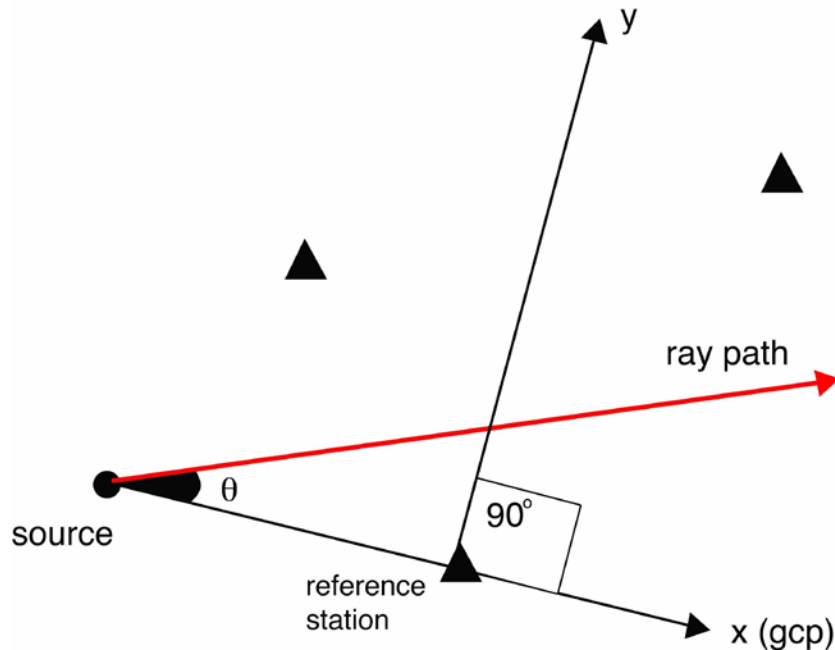


Figure 7. A schematic of local Cartesian coordinate system. The reference station is chosen using the minimum RMS misfit in amplitude with respect to mean value, x-axis is along the great circle path (gcp) with the source, and y-axis is 90° counterclockwise. Triangles show stations. The distance between the source and the center of the seismic array is greater than 20° .

To invert for these unknowns, a local Cartesian coordinate system is set up for each event (Figure 7), where the reference station is the origin, the x direction is along the great circle path between source and reference station, and the y direction is 90° counterclockwise from x. The reference station is determined using the lowest root mean square error of amplitudes with respect to the mean value. Alternate methods for the reference station decision include using the shortest event-receiver distance or maximum amplitude.

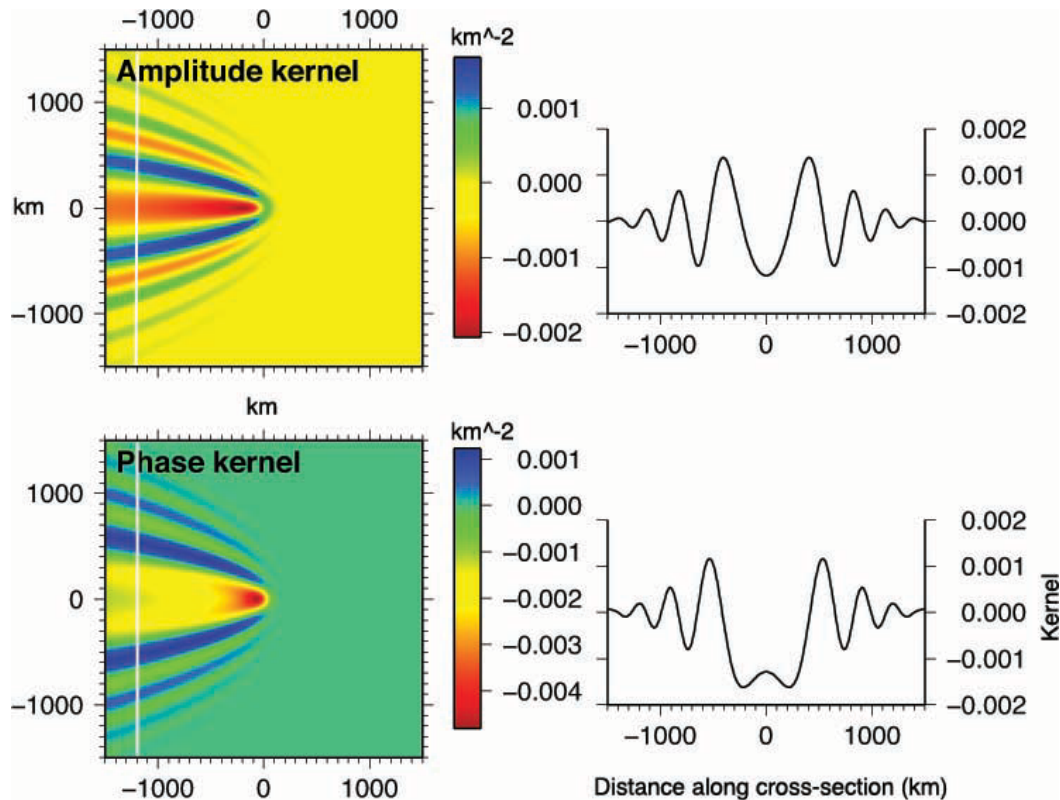


Figure 8. Map views of amplitude and phase sensitivity kernels for 20 mHz Rayleigh waves, obtained using the Born approximation. *Panels on the right side show cross-sections along -1200 km (white solid line on map views). The hypothetical station is located at the center, and source is to the west.*

Following the standard procedure, we calculated the phase wave speeds using both Rayleigh (vertical component) and/or Love (transverse component) waves for a set of frequencies at defined points within a study area. Then, we used these 1D dispersion results for obtaining a 3D shear wave structure. More specifically, we employed the DISPER80 algorithm (Saito, 1988) for each individual dispersion curve to obtain a 1D shear wave profile. Next, these shear wave profiles are combined to construct a 3D model. To account for finite frequency effects, we incorporate sensitivity kernels at the phase velocity inversion stage.

In order to account for the finite frequency effects, earlier versions of TPWT implemented Gaussian kernels. These kernels do not accurately represent finite frequency

effects as they assume a constant Gaussian-shaped sensitivity function perpendicular to the ray path (Forsyth et al., 1998). On the other hand, modified versions of TPWT use single scattering (Born) approximation sensitivity kernels (Yang and Forsyth, 2006) of Zhou et al. (2004) (Figure 8). 2D sensitivity kernels for fundamental mode surface waves using the Born approximation can be described as (Zhou et al., 2004):

$$K(r, \omega) = \frac{2k^2 S' R'' \exp\{-i[k(\Delta' + \Delta'' - \Delta) - \pi/2(n' + n'' - n) + \pi/4]\}}{SR \sqrt{8\pi k \left(\frac{|\sin\Delta'| |\sin\Delta''|}{|\sin\Delta|} \right)}} \quad (3)$$

where K is the sensitivity kernel as a function of propagation direction (r) and angular frequency (ω). Single and double primed symbols denote waves from source to scatterer, and from scatterer to receiver, respectively. Symbols with no primes indicate direct waves from source to station. The integer n is the polar passage index, indicating how many times a wave train passes thorough the source or its antipode. Δ shows the distance between source-scatterer (Δ'), scatterer-receiver (Δ''), or source-receiver (Δ). Source and receiver polarization terms are indicated using S and R , respectively.

The real and imaginary parts of Equation (3) give amplitude and phase kernels, respectively. These are:

$$K_\phi(r, \omega) = \text{Im}\{K(r, \omega)\} \quad (4)$$

$$K_A(r, \omega) = -\text{Re}\{K(r, \omega)\} \quad (5)$$

In the above equations, scattered and direct arriving waves are due to the same earthquake. Therefore, source terms (S and S') can be neglected. In our case, surface wave tomography is a minor arc problem. Therefore, a wave train never passes through the source or its antipode again. Hence, the polar passage index is zero ($n = 0$), and vanishes from Equation (3). Moreover, in the case of Rayleigh waves, only vertical components of seismograms are used. For this reason, receiver polarization vectors (R) for direct and scattered waves are equal (Yang and Forsyth, 2006). However, Love wave energy is concentrated on the transverse plane; and polarization terms are functions of scattering angle (Snieder, 1986).

In reality, sensitivity kernels are not the same for the whole earth. Rather, they are functions of earth structure and may change along the propagation path in their amplitudes and geometry. However, in regional tomography studies, research areas are relatively small. Most probably, variations in sensitivity kernels have a minor role in tomography results, and therefore I make a final assumption and neglect these variations.

3.2 Pn and Sn Travel Time Tomography

For each layer, we followed the Pn tomography technique developed by Hearn and Ni (1994). The uppermost layer of the mantle is divided into a set of two-dimensional cells, in which the slownesses (inverse velocities) are estimated. The Pn travel time residuals are described approximately by the perturbation equation

$$t_{ij} = a_i + b_j + \sum d_{ijk} S_k \quad (6),$$

where t_{ij} is the travel time residual for event j and station i , a_i is the static delay for station i , b_j is the static delay for event j , d_{ijk} is the travel distance of ray ij in mantle cell k , and S_k is the slowness perturbation for cell. The unknown quantities in equation (6) are the mantle slowness perturbation S_k and the station and event delays a_i and b_j , respectively. The station and event delays accommodate variations in crustal velocity and thickness.

For the inversion, we used a cell size of $0.5^\circ \times 0.5^\circ$. The slowness values in each cell were resolved using the LSQR algorithm (Paige and Saunders, 1982; Yao et al., 1999). While we attempted to resolve azimuthal anisotropy, we could not obtain sufficient resolution to tightly constrain azimuthal anisotropy fast directions and magnitude, in this project, we have focused on the Pn and Sn velocity variations and the velocity ratio, assuming a spatially varying isotropic velocity model. It is important to note that one of the difficulties in measuring Pn and Sn azimuthal anisotropy is the difference in sampling depths for different epicentral distances. Often this can bias these types of measurements requiring that a relatively narrow range of distances be used to solve for Pn or Sn anisotropy. Typically, including the anisotropic terms (cosine and sine terms) (Lü et al., 2012), has a marginal impact on the major isotropic velocity variations. Therefore, our tomography can most likely provide a reliable uppermost mantle velocity structure of the study area.

3.3 Two and Reverse Two Station Q Tomography

The amplitude of a seismic wave may be described by an exponential attenuation equation that accounts for both geometric spreading and attenuation,

$$A_{ij}(f) = I_i(f) S_{si}(f) S_j(f) G(\Delta_{ij}) \exp\left(-\frac{\pi f \Delta_{ij}}{v Q(f)}\right) \quad (7)$$

where A is the observed amplitude between source (indices j) and receiver (indices i) for a wave of frequency f recorded at distance Δ . Here, I_i is the instrument response, S_j is the source amplitude, S_{si} is the site amplification response, and v is the wave group speed. Geometric spreading is defined as the following:

$$G(\Delta) = \frac{1}{\Delta^m} \quad (8)$$

For cylindrical spreading m is 0.5 and for spherical spreading m is 1.0. When dispersion is accounted for, these can increase by up to 0.3 depending on signal bandwidth. We assume this function is frequency independent; however, this may be a poor assumption

in many cases and these differences will be mapped into our effective Q or more specifically the scattering component of our effective Q . Spreading relations are important but poorly documented and must be given explicit attention in attenuation problems. The attenuation quality factor, Q , can be assumed to be frequency dependent, $Q=Q_0 f^\eta$ with Q_0 being the attenuation quality factor at 1 Hz, f the wave frequency, and η the frequency dependence. Values for Q_0 and η depend on the type of wave used but generally η lies between zero and one. This equation does not account for radiation pattern, focusing, or anisotropic effects. However, with good azimuthal coverage, these effects should average out. Both Q and amplitude tomography methods are based on this equation, with appropriate modifications.

The TSM was presented by Mitchell (1995) and has been widely used (e.g., Nuttli, 1986). Xie and Mitchell (1990) use the assumption of spreading such as that shown in equation 8 and that $Q(f)=Q_0^{-\eta}$:

$$(1-\eta)\ln f - \ln Q_0 = \frac{v}{\pi(d_j - d_i)} \ln \left(\frac{A_i(f)I_j(f)d_i^m}{A_j(f)I_i(f)d_j^m} \right) \quad (9)$$

where $d_j-d_i=\Delta$. The real situation for applying the TSM is more complicated because the perfect alignment geometry is typically not obtainable, especially for passive seismic experiments. In practice, event to station paths differ by a small angle $\delta\theta$. A detailed analysis of this angle has been presented by Xie et al. (2004). Systematic errors could be introduced into Q_0 and η values determined by the TSM because of effects of attenuation out of the path and anisotropic source radiation patterns. These errors can be minimized if a threshold value $\delta\theta_{\max}$ is used to limit the angle $\delta\theta$. Xie et al. (2004) used a $\delta\theta_{\max}$ of $\pm 15^\circ$ in their study, which had been estimated by Der et al. (1982). Xie et al. (2004) also derived an equation to minimize an error related to the variation of inter-station distance at 1 Hz. This equation (Xie et al., 2004) is reorganized here:

$$\frac{\delta Q}{Q^2} = \frac{v}{\pi f} \frac{1}{(d_j - d_i)} \delta x \quad (10)$$

where d_j-d_i is the inter-station distance, δQ_0 is the error in the measured Q_0 , and δx is the total unaccounted for error in equation (3), which assumes an ideal geometry and 1D structure. In this study, we follow Xie et al. (2004) by setting $\delta\theta$ to 15° and δx smaller than 0.4. Also, the equation indicates that to reduce the Q error, it is preferable to maximize the inter-station distance.

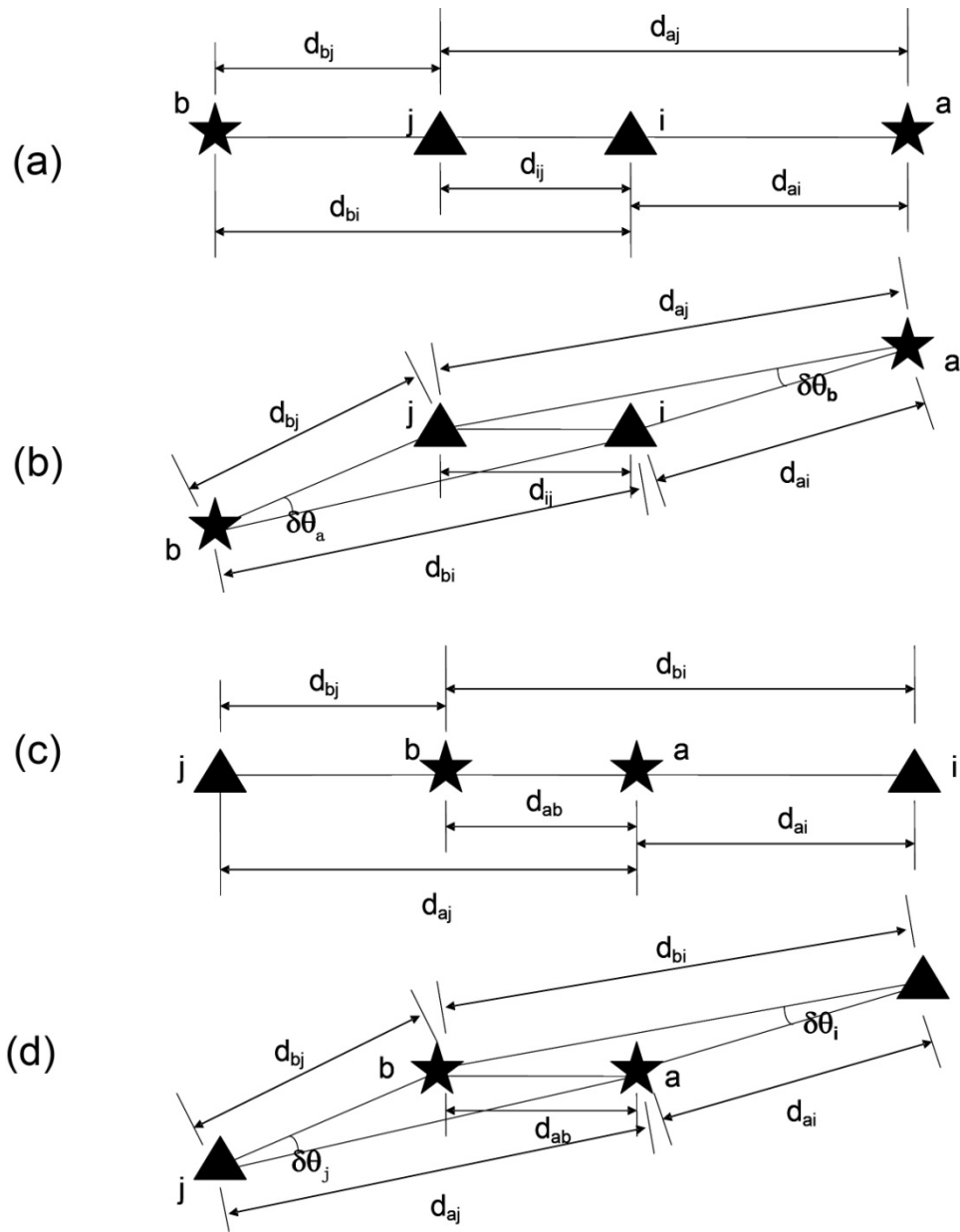


Figure 9 Schematic drawing of the geometry of RTS and RTE. *RTS-* (a) the ideal situation where the source a (star on the right), the station i and j (triangles), and source b (star on the left) are aligned along a great circle, and (b) the more common situation where the azimuth difference angles from sources a and b to the stations are denoted by $\delta\theta_a$ and $\delta\theta_b$ respectively. *RTE-* (c) the ideal situation where the station i (triangle on the right), the sources a and b (stars), and station j (triangle on the left) are aligned along a great circle, and (d) the more common situation where the azimuth difference angles from stations i and j to the events are denoted by $\delta\theta_i$ and $\delta\theta_j$ respectively.

The main disadvantage of the TSM is caused by the remaining instrument response I and neglected site response $S_S(f)$. The instrument responses are only theoretically identical for stations with identical seismometers and data loggers. In practice, instrument calibration is commonly impossible during deployment, which also does not preclude the influence

of various time-varying uncalibrated instabilities on the recorded amplitude. It is also difficult to guarantee the operability of calibration of all instruments. The site effects have been suggested to have strong lateral variations and are likely associated with shallow geological structures, especially in tectonically active zones (Wald and Allen, 2007; Pasyanos et al., 2009). Therefore, the site effects independent of instruments can contaminate the measurements of Q if we use the TSM. It is probably an oversimplification to assume the complicated instrument response and site response with a merely theoretically consistent model of instrument response and a neglected site response.

The RTM was suggested to avoid the effects of neglected S_s terms and inaccurate I terms in the TSM by involving one more event. The RTM was initially suggested by Chun et al. (1987). Figure 9 shows the geometry of the RTM including its two cases: the Reverse Two Station (RTS) paths and Reverse Two Event (RTE) paths. The ideal case for RTS is that both events are aligned with the inter-station path, and requires the four epicentral distances involved to be within a regional distance range. In such a situation, we use A_{ai} , A_{aj} , A_{bi} , and A_{bj} to denote spectral amplitudes of Lg recorded at stations i and j for events a and b , and d_{ai} , d_{aj} , d_{bi} , and d_{bj} the corresponding distances. The four spectral amplitudes can be expressed as:

$$\begin{aligned} A_{ai}(f, d_{ai}) &= S_a(f)R_a(f, \varphi)I_i(f)S_{Si}(f)G_{ai}(d_{ai})\exp\left[-\frac{\pi f d_{ai}}{vQ_i}\right] \\ A_{aj}(f, d_{aj}) &= S_a(f)R_a(f, \varphi)I_j(f)S_{Sj}(f)G_{aj}(d_{aj})\exp\left[-\frac{\pi f d_{aj}}{vQ_j}\right] \\ A_{bi}(f, d_{bi}) &= S_b(f)R_b(f, \varphi)I_i(f)S_{Si}(f)G_{bi}(d_{bi})\exp\left[-\frac{\pi f d_{bi}}{vQ_i}\right] \\ A_{bj}(f, d_{bj}) &= S_b(f)R_b(f, \varphi)I_j(f)S_{Sj}(f)G_{bj}(d_{bj})\exp\left[-\frac{\pi f d_{bj}}{vQ_j}\right] \end{aligned} \quad (11)$$

If A_{ai} is divided by A_{aj} and A_{bi} is divided by A_{bj} , we get (note the exponents are negative):

$$\begin{cases} \frac{A_{ai}}{A_{aj}} = \frac{S_a}{S_a} \frac{R_a}{R_a} \frac{I_i}{I_j} \frac{S_{Si}}{S_{Sj}} \frac{G_{ai}}{G_{aj}} \exp\left(\frac{\pi f d_{aj}}{v_j Q_j} - \frac{\pi f d_{ai}}{v_i Q_i}\right) = \frac{I_i}{I_j} \frac{S_{Si}}{S_{Sj}} \frac{G_{ai}}{G_{aj}} \exp\left(\frac{\pi f d_{aj}}{v_j Q_j} - \frac{\pi f d_{ai}}{v_i Q_i}\right) \\ \frac{A_{bi}}{A_{bj}} = \frac{S_b}{S_b} \frac{R_b}{R_b} \frac{I_i}{I_j} \frac{S_{Si}}{S_{Sj}} \frac{G_{bi}}{G_{bj}} \exp\left(\frac{\pi f d_{bj}}{v_j Q_j} - \frac{\pi f d_{bi}}{v_i Q_i}\right) = \frac{I_i}{I_j} \frac{S_{Si}}{S_{Sj}} \frac{G_{bi}}{G_{bj}} \exp\left(\frac{\pi f d_{bj}}{v_j Q_j} - \frac{\pi f d_{bi}}{v_i Q_i}\right) \end{cases} \quad (12)$$

Like the TSM, we assume that the velocity structure is one-dimensional and apparent Q values are identical for the path between stations i and j . We divide the two ratios in (11), substitute, and obtain

$$\frac{A_{ai}A_{bj}}{A_{aj}A_{bi}} = \left(\frac{d_{ai}d_{bj}}{d_{aj}d_{bi}}\right)^{-m} \exp\left[\frac{\pi f}{vQ}(d_{aj} - d_{ai} - d_{bj} + d_{bi})\right]. \quad (13)$$

where all of the Q parameters above are a function of frequency and m is the exponent from equation 8. Therefore, the inter-station (between i and j) apparent $1/Q$ value can be derived as

$$\frac{1}{Q} = \frac{v}{\pi f (d_{aj} - d_{ai} - d_{bj} + d_{bi})} \ln \left[\frac{A_{ai} A_{bj}}{A_{aj} A_{bi}} \left(\frac{d_{ai} d_{bj}}{d_{aj} d_{bi}} \right)^m \right], \quad (14)$$

whose reciprocal is the inter-station apparent Q . Like the TSM, (11) to (14) are all in the frequency domain. The $1/Q$ as a function of the frequency f is

$$\frac{1}{Q(f)} = \frac{v}{\pi f (d_{aj} - d_{ai} - d_{bj} + d_{bi})} \ln \left[\frac{A_{ai}(f) A_{bj}(f)}{A_{aj}(f) A_{bi}(f)} \left(\frac{d_{ai} d_{bj}}{d_{aj} d_{bi}} \right)^m \right]. \quad (15)$$

(15) shows that the RTS does not require any assumptions on the instrument responses and site responses. (15) is similar to (16), but it requires four spectra and four distances, not the two spectra and two distances in the TSM. A pre-determination of m is also required, as it is with the TSM.

Figure 9c shows that the geometry of ideal RTE closely resembles that of RTS except that the positions of stations and events are switched. This case was not presented until the study of Fan and Lay (2003). Similar to (11), we can write

$$\begin{cases} A_{ai}(f, d_{ai}) = S_a(f) R_a(f, \varphi) I_i(f) S_{si}(f) G_{ai}(d_{ai}) e^{\frac{\pi f d_{ai}}{v_a Q_a}} \\ A_{aj}(f, d_{aj}) = S_a(f) R_a(f, \varphi) I_j(f) S_{sj}(f) G_{aj}(d_{aj}) e^{\frac{\pi f d_{aj}}{v_a Q_a}} \\ A_{bi}(f, d_{bi}) = S_b(f) R_b(f, \varphi) I_i(f) S_{si}(f) G_{bi}(d_{bi}) e^{\frac{\pi f d_{bi}}{v_b Q_b}} \\ A_{bj}(f, d_{bj}) = S_b(f) R_b(f, \varphi) I_j(f) S_{sj}(f) G_{bj}(d_{bj}) e^{\frac{\pi f d_{bj}}{v_b Q_b}} \end{cases}. \quad (16)$$

Similar to the RTS, we assume that the velocity structure is one-dimensional and apparent Q values are identical at events a and b in the RTE case, which leads from (15) to (17), the same equation as in the RTS case. The RTM allows the event locations to deviate from the inter-station great circle by two small angles $\delta\theta_a$ and $\delta\theta_b$ in the RTS, and the station locations to deviate from the inter-event great circle by two small angles $\delta\theta_i$ and $\delta\theta_j$ in the RTE. We set maximum values of $\pm 15^\circ$ (the same as that in the TSM) for those four angles. And the procedure of RTM is also very similar to that of TSM. We follow steps as used in the TSM, and use (15) as the equation to calculate Q using a linear regression.

The main disadvantage of RTS is the typically poor path coverage because of its rigorous geometrical requirement. Thus its feasibility strongly depends on the seismic network. To satisfy the geometry of RTS, continental ray paths of regional distances, inter-station or inter-event distance not less than 150 km, and angle difference within $\pm 15^\circ$ are required for all the two stations and two events. The RTE provides a dramatic advantage over the

rigorous requirements of the RTS. The stations are not required to be deployed in the study area, and can be deployed around a seismic zone within regional distances, which greatly increases the practicability and accuracy of the generalized RTM. Particularly, the RTE can become very efficient in regions with relatively active seismicity and a relatively difficult natural environment for dense seismic networks. The disadvantage is that its resolution is reduced by probable earthquake mislocations in event catalogs.

The second application of the RTM is that we can use it to solve relative site responses. From equation 10 we obtain

$$\frac{A_{ai}A_{bi}}{A_{aj}A_{bj}} = \left(\frac{I_i}{I_j} \frac{S_{Si}}{S_{Sj}} \right)^2 \left(\frac{G_{ai}G_{bi}}{G_{aj}G_{bj}} \right) \exp \left(\frac{\pi f d_{aj}}{v_j Q_j} - \frac{\pi f d_{ai}}{v_i Q_i} + \frac{\pi f d_{bj}}{v_j Q_j} - \frac{\pi f d_{bi}}{v_i Q_i} \right). \quad (17)$$

Using equation 17 we can solve for the logarithm of the ratio of the site response which gives us a relationship for the relative site response:

$$\begin{aligned} \ln \frac{S_{Si}}{S_{Sj}} = & \ln \frac{I_j}{I_i} + \frac{d_{aj} - d_{ai}}{d_{aj} + d_{bi} - d_{ai} - d_{bj}} \ln \frac{A_{ai}d_{ai}^m}{A_{aj}d_{aj}^m} \\ & + \frac{d_{bi} - d_{bj}}{d_{aj} + d_{bi} - d_{ai} - d_{bj}} \ln \frac{A_{bi}d_{bi}^m}{A_{bj}d_{bj}^m}. \end{aligned} \quad (18)$$

And can be further transferred to

$$\begin{aligned} \ln S_{Si} - \ln S_{Sj} = & \ln \frac{I_j}{I_i} + \frac{d_{aj} - d_{ai}}{d_{aj} + d_{bi} - d_{ai} - d_{bj}} \ln \frac{A_{ai}d_{ai}^m}{A_{aj}d_{aj}^m} \\ & + \frac{d_{bi} - d_{bj}}{d_{aj} + d_{bi} - d_{ai} - d_{bj}} \ln \frac{A_{bi}d_{bi}^m}{A_{bj}d_{bj}^m}. \end{aligned} \quad (19)$$

Tomographic inversions generally use least squares algorithms such as LSQR (Paige and Saunders, 1982). Constraints on the problem are of great importance and can be introduced using regularization and damping techniques. For example, spatial variations in attenuation are regularized using first or second difference smoothing constraints. Source models, such as MDAC (Walter and Taylor, 2002), can also be included in tomographic inversions for Q. Moments and corner frequencies can be damped to known levels for special events, or regularized to follow a best-fit scaling model. Resolution and covariance are quantified using impulse responses, checkerboard tests, and matrix inversion techniques. Such estimates assume that the model equations describe the physics perfectly, which we know is not completely true. Dense networks such as the Iranian combined networks have allowed us to investigate what are very often unmodeled effects, such as the source radiation, focusing, and medium anisotropy effects mentioned earlier.

Attenuation tomography uses estimates of path-averaged attenuation to delineate laterally varying Q . This includes most spectral methods (e.g. Zor et al., 2007). An example of attenuation tomography for Asia using coarsely spaced stations can be found in Xie et al., 2006. Our attenuation (Q) tomography relies on two-station methods for measuring inter-station Q , which cancel the source effect by using station pairs aligned with the source. These methods are relatively straightforward to apply, and are insensitive to source radiation pattern effects, but alignment requirements reduce the amount of data that can be used. We have measured attenuation with the two-station (see Xie and Mitchell, 1990; Xie, 2002b; and Zor et al., 2007 for descriptions of the method, including rigorous error analysis) and reversed two station (Chun et al., 1987) methods.

As our derivation of the RTM terms has shown, the reversed method eliminates site as well as source effects. Furthermore we have been able to use the reverse two station approach to isolate the site and calculate the relative site effect. Thus, after correcting for geometrical spreading, we were able to isolate relative site terms and thereby create maps of relative site terms for much of the eastern Tibetan plateau. We can use these relations to determine both path based Q values that are independent of the site effect as well as a relative site effect term. We have found this to improve attenuation models in particular for Pg attenuation in eastern Tibet. This has been previously difficult in the Tibetan plateau because of a lack of contemporaneously recording stations.

Q_0 and η values measured using these methods are of very high quality because they are not subject to the trade-off between source and path parameters, and the smaller data sets can be easily scrubbed with the most rigorous quality control. Measured Q_0 and η values are used to derive a long-wavelength Q map for the eastern Tibetan Plateau. This model can be subsequently used as a priori knowledge during amplitude tomography calculations. Alternately, inter-station Q measurements can be included as constraints in the amplitude tomography. Once again, the combined ASCENT, NETS, and Namche Barwe arrays are ideally designed to tomographically map Q in this region with a high degree of resolution, and have increased resolution in surrounding areas when included in continental scale studies.

3.4 Q Anisotropy Method

Given the reliability of our reverse two station Q estimates, we determined that we should be able, given sufficient ray path coverage, to resolve azimuthal variations in Q . We suggest that the azimuthal anisotropy of $1/Q_{Lg}$ can be described as

$$1/Q_{Lg} = A + B \sin^2(\varphi - \theta) + C \sin^4(\varphi - \theta), \quad (20)$$

where A is the isotropic coefficient and B and C are the 2nd order and 4th order anisotropic coefficients respectively. The angles φ and θ denote the path azimuth and high- Q direction, respectively. Furthermore, (20) can be transformed to

$$\begin{aligned}
1/Q_{Lg} = & \left(A + \frac{1}{2}B + \frac{3}{8}C \right) \\
& + \left(-\frac{B+C}{2} \right) \cos 2\theta \cos 2\varphi + \left(-\frac{B+C}{2} \right) \sin 2\theta \sin 2\varphi. \quad (21) \\
& + \frac{C}{8} \cos 4\theta \cos 4\varphi + \frac{C}{8} \sin 4\theta \sin 4\varphi
\end{aligned}$$

We notice that (2) is similar to the expression of azimuthal anisotropy for surface waves (Smith and Dahlen, 1973). Typically the 4φ terms are considered negligible (Montagner and Nataf, 1986) in many studies (e.g., Hearn, 1996; Huang et al., 2003; Yao et al., 2010). Moreover, a comparison between velocity and attenuation azimuthal anisotropy (Chapman, 2009) and our observations suggest that the effect from 4φ terms can be neglected for Q_{Lg} measured from the vertical component signal. Thus (21) will be

$$1/Q_{Lg} = \left(A + \frac{1}{2}B \right) + \left(-\frac{B}{2} \right) \cos 2\theta \cos 2\varphi + \left(-\frac{B}{2} \right) \sin 2\theta \sin 2\varphi, \quad (22)$$

where A is the isotropic coefficient (or isotropic $1/Q_{Lg}$) and B the anisotropic coefficient (or anisotropic magnitude).

We can assume that A , B , and θ are all frequency dependent. The lateral variations in A and B can be solved from 4-spectral-amplitude groups at different frequencies by dividing the study area into a two dimensional set of square cells. All Lg windows are manually picked and show a nearly constant v_{Lg} of 3.5 km/s, and the study of Chapman (2009) suggests that the lateral variation in velocity is probably negligible using this method. The geometrical spreading factor m of Lg is typically set at 0.5 (Hasegawa, 1985). We assume that A , B , and θ are constant inside each cell at each frequency. Referring to the method of Q tomography of Xie and Mitchell (1990), for each 4-spectral-amplitude group and each frequency f_n , (22) can be finally derived as

$$\sum d_k (X_{kn} f_n + Y_{kn} f_n \cos 2\varphi_k + Z_{kn} f_n \sin 2\varphi_k) = \frac{v_{Lg}}{\pi} \ln \left(\frac{A_{ai} A_{bj}}{A_{aj} A_{bi}} \left(\frac{d_{ai} d_{bj}}{d_{aj} d_{bi}} \right)^m \right), \quad (23)$$

$$X_{kn} = A_{kn} + \frac{1}{2} B_{kn}, \quad Y_{kn} = -\frac{B_{kn}}{2} \cos \theta_{kn}, \quad Z_{kn} = -\frac{B_{kn}}{2} \sin \theta_{kn},$$

where d_k and φ_k are the distance and azimuth travelled by path ij in cell k , respectively, and A_{kn} , B_{kn} , and θ_{kn} the isotropic coefficient, anisotropic coefficient, and high- Q direction of cell k and frequency f_n , respectively. A_{kn} , B_{kn} , and θ_{kn} are unknown variables and are assumed to be frequency dependent.

The linear system of (23) can be written in matrix form $\mathbf{D}=\mathbf{Gm}$. We denote the number of 4-spectra-amplitude groups by N_A and the number of discrete frequencies by N_F . The vector \mathbf{D} has its elements calculated from the terms on the right side of the equal sign in (4), and the length of it is $N_A N_F$. The vector \mathbf{m} consists of all unknown parameters including X_{kn} , Y_{kn} , and Z_{kn} in (23) of all cells and frequencies, and the length of it is $3MNN_F$ if the study area is divided into $M \times N$ cells. The matrix \mathbf{G} is a large and sparse matrix with the size of $N_A N_F \times 3MNN_F$. We use an LSQR algorithm (Paige and Saunders,

1982) to solve this inverse problem. Like the Pn velocity anisotropy (Hearn, 1996) and surface wave azimuthal anisotropy (e.g., Yao et al., 2010), the corresponding elements in the solution vector \mathbf{m} can be used to determine A_{kn} and B_{kn} , and the high- Q direction θ_{kv} by:

$$\begin{aligned} A_{kn} &= X_{kn} - \sqrt{Y_{kn}^2 + Z_{kn}^2} \\ B_{kn} &= 2\sqrt{Y_{kn}^2 + Z_{kn}^2} \\ \theta_{kn} &= \begin{cases} 90^\circ + \frac{1}{2} \arctan\left(\frac{Z_{kn}}{Y_{kn}}\right) & \text{if } Y_{kn} \geq 0 \\ 180^\circ + \frac{1}{2} \arctan\left(\frac{Z_{kn}}{Y_{kn}}\right) & \text{if } Y_{kn} < 0, Z_{kn} \geq 0 \\ \frac{1}{2} \arctan\left(\frac{Z_{kn}}{Y_{kn}}\right) & \text{if } Y_{kn} < 0, Z_{kn} < 0 \end{cases}, \end{aligned} \quad (24)$$

The result is regularized by using a nine-point spatial smoothing, which was used in Q_{Lg} tomography by Suetsugu and Nakanishi (1985) and Xie and Mitchell (1990). If $k(p, q)$ denotes the k th cell, where p and q are cell numbers in the latitude and longitude directions, respectively, a set of regularization equations are organized by counting all neighboring cells of the k th cell to build a matrix \mathbf{L} :

$$\begin{aligned} \frac{1}{(L_{k(p,q)})'} &= \frac{1}{2} \left[\frac{1}{L_{k(p-1,q-1)}} + \frac{1}{L_{k(p-1,q+1)}} + \frac{1}{L_{k(p+1,q-1)}} + \frac{1}{L_{k(p+1,q+1)}} \right] \\ &+ \frac{4}{2} \left[\frac{1}{L_{k(p,q-1)}} + \frac{1}{L_{k(p,q+1)}} + \frac{1}{L_{k(p-1,q)}} + \frac{1}{L_{k(p+1,q)}} \right] + \frac{9}{2 L_{k(p,q)}}. \end{aligned} \quad (25)$$

Two damping factors λ_1 and λ_2 are applied to balance the trade-off between isotropic and anisotropic terms, while λ_1 is for X_{kn} and λ_2 is for Y_{kn} and Z_{kn} . Two damping factors λ_1 and λ_2 are applied to balance the trade-off between isotropic and anisotropic terms, while λ_1 is for X_{kn} and λ_2 is for Y_{kn} and Z_{kn} .

We have also continued work on creating a reliable tomographic model for the Pn velocity structure in western China including station corrections or crustal delay times. Data from recent INDEPTH IV and other broadband deployments in Tibet are used to invert for crustal delays and Pn velocities beneath the eastern Tibetan Plateau and surrounding regions. The average Pn velocity for the region is 8.1km/s but varies from 7.8 to over 8.3km/s. Generally low Pn velocities are found in northeastern Tibet in the Qiangtang and Songpan-Ganzi terrains. This includes a zone of very low Pn velocity northwest of the Longmen Shan thrust, along the eastern Kunlun fault, and beneath the eastern Qilian Shan. A region of high Pn velocity underlies the eastern end of the Bangong-Nujiang Suture (bounded by 31°-33°N; 90°-98°E). It could represent part of the underthrust Indian shield. The region between the Qilian Shan and Kunlun Shan is also characterized by high Pn velocity with several zones of extremely high velocity. This includes two high velocity features beneath Qaidam basin and Gonghe basin. These features may correspond to cratonic fragments that accreted during the closure of the Tethys Ocean and have impeded, but not stopped, the northward growth of the plateau.

The station delays show the thickest crust is beneath Tanggula Shan in central Tibet and should be the result of the internal deformation within Qiangtang terrain due to the collision of Indian and Eurasia plates. There is a significant decrease of crustal thickness in the northeast plateau and lateral variation also exists within the region.

To investigate the lateral resolution of the inversion parameters, checkerboard tests are used to determine the most appropriate damping factors and the approximate size of anomalies which can be retrieved. Two reference values for A and B are both set at $1/300$, respectively, and the perturbation of A is 50%, which is selected to approximately simulate the observation of anisotropic attenuation from our data (Figure 10). Two sinusoidal functions designed for north-south (N-S) and west-east (E-W) synthetic high Q directions, respectively, are used to calculate the variations of A and B . Thus each checkerboard block has the maximum ($1/200$) or minimum ($1/600$) of A and maximum of B ($1/300$) at its center, and the average of A ($1/300$) and minimum of B (0) along all the edges of the synthetic Q anomalies. Staggered θ values of 0° and 90° are used in neighboring blocks. The checkerboard tests of $1^\circ \times 1^\circ$ anomalies are likely irretrievable, especially for the anisotropic terms, which is probably because of insufficient path density. We further test four checkerboard patterns where all designed anomalies have the same size of $2^\circ \times 2^\circ$ (Fig. 3). Among the four patterns, Pattern 1 and Pattern 2 have the same variations of A and B but opposite θ distribution; and Pattern 3 and Pattern 4 have the opposite variations of A and B to Pattern 1 and Pattern 2, and the same θ distribution as Pattern 1 and Pattern 2, respectively. A normally distributed random noise of 0%, 15%, and 25%, is added into all the tests. We simultaneously solve A , B , and θ by dividing the region into $0.5^\circ \times 0.5^\circ$ square cells in tomography. The ideal damping factors λ_1 and λ_2 should be selected to minimize the trade-off between lateral variations of A and B , which occurs when a variable R_{ia} , defined from the residuals of A and B as

$$R_{ia} = \frac{\sum (A - A_0)^2}{\sum (B - B_0)^2}, \quad (26)$$

is equal to 1, where A_0 and B_0 denote parameters in the given model and A and B denote parameters in the solution. The R_{ia} in (26) only includes residuals in the area defined by limiting the hit-count to more than 5 within each cell of the model.

An example of how the best λ_1 and λ_2 are determined for Pattern-1 in Figure 10 is shown in Figure 11, where a grid search is used for different λ_1 and λ_2 pairs varied from 0.02 to 0.3, and contours of R_{ia} value are illustrated and labeled. An important observation is that an increase in λ_1 leads to an increase in the residual of A and a corresponding decrease in the residual of B , and an increase λ_2 causes an increase in the residual of B and a decrease in the residual of A . A low residual of A probably deserves priority in our problem because A will be very important in a further discussion on its frequency dependency. Thus we determine the best λ_1 and λ_2 pairs by satisfying a sufficiently low residual of A and a point within a 15% perturbation of R_{ia} of 1 (between 0.85 and 1.15) among the contours in Fig. 4. Moreover, we observe that the level of random noise may slightly affect R_{ia} , where the contours change substantially by increasing the noise from 0% to

25%, but this is not as significant as the influence from the changes in damping parameters. We also observe that we are able to maintain a stable and relatively high resolution with a level of random noise of up to 15%, but a higher level of random noise rapidly decreases the resolvability (defined by *Zelt* [1998]) and makes the inversion unstable. We finally determine that λ_1 and λ_2 can be typically selected at 0.15 and 0.25, respectively, based on a number of such tests using a grid search. This actually means that the trade-off between A and B is conditionally minimized to less than 15%. The results of the four tests indicate good resolution for anomalies at $2^\circ \times 2^\circ$ scale with 15% random noise when we use a cell size of $0.5^\circ \times 0.5^\circ$ (Fig. 3).

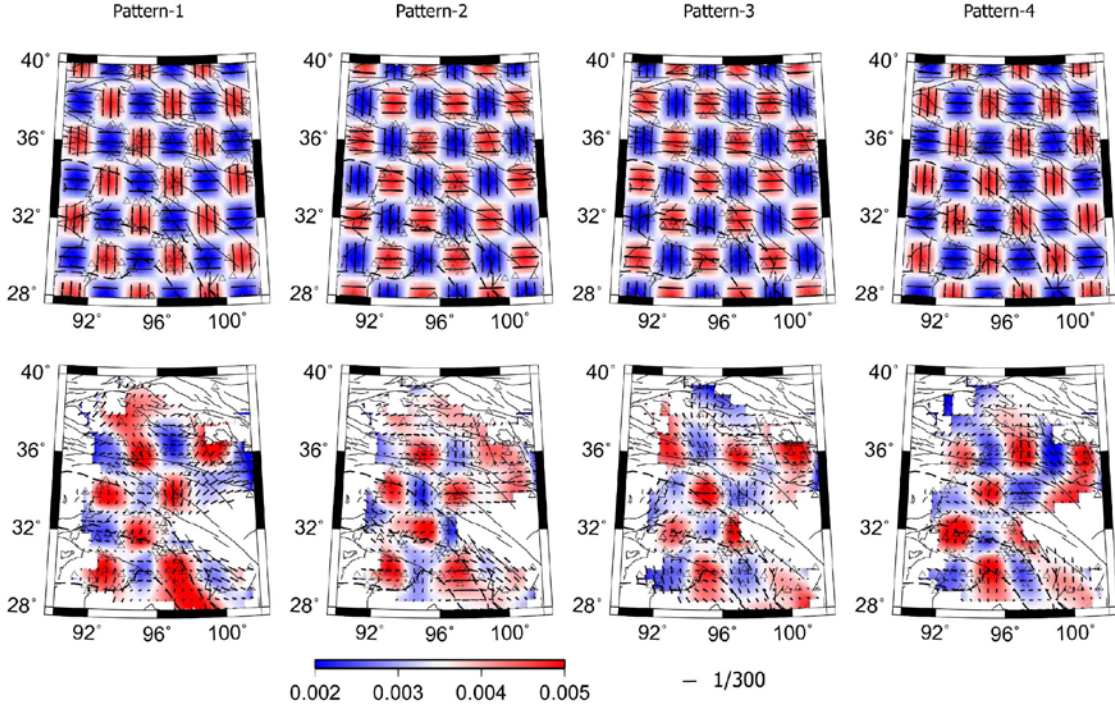


Figure 10. A resolution test to determine whether we are able to resolve azimuthal Q anisotropy given our reverse two station path coverage.

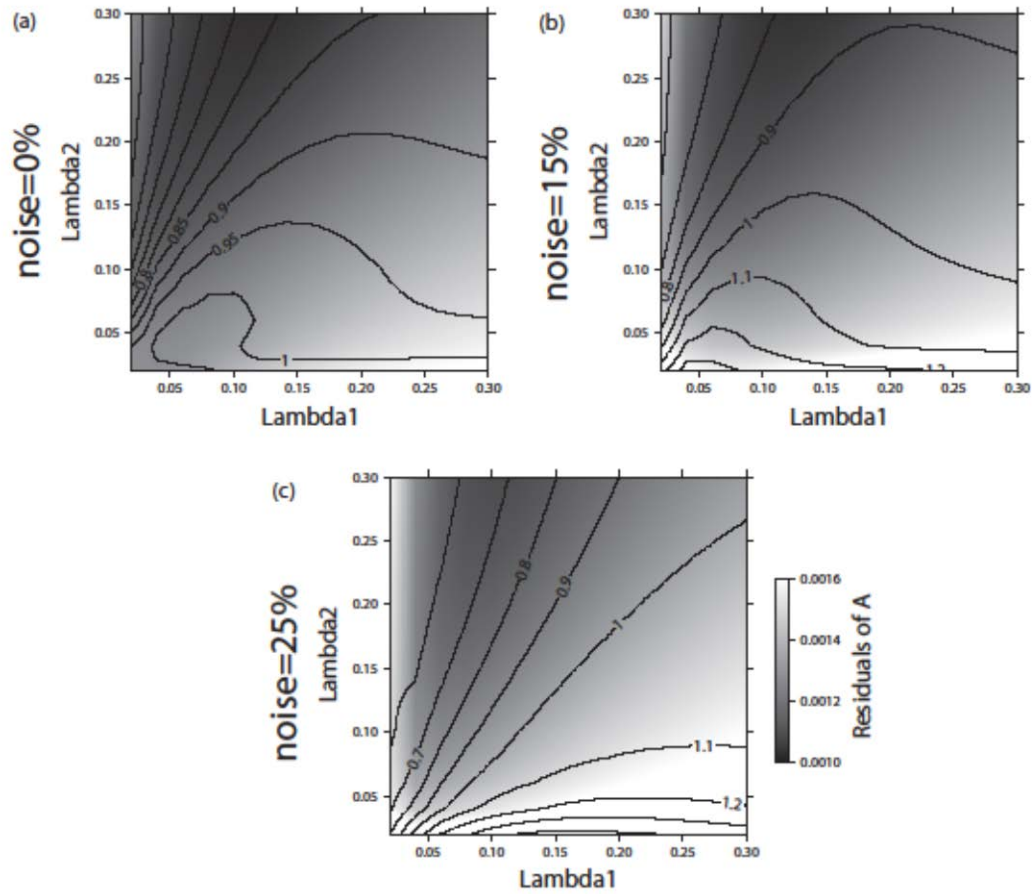


Figure 11. An example of the grid search result on the co-influence of damping factors λ_1 and λ_2 on the residual ratios of isotropic and anisotropic coefficients A and B when (a) no random noise, (b) 15% random noise, and (c) 25% random noise are added, respectively. The checkerboard pattern of this example is shown in Pattern 1 of Figure 10. The gray color backgrounds represent scales of the residuals of A . The labeled contours represent the distribution of R_{ia} defined in (26). The effect from added random noise level is dominant over that from damping factors. The best damping factor pair is selected when the residual of A is at a minimum value and the perturbation of R_{ia} is between ± 15 percent (0.85 to 1.15). This shows that the trade-off between isotropy and anisotropy is conditionally minimized at a secondary bias for the approach of a realistic isotropic coefficient. Typically, λ_1 and λ_2 can be selected at 0.15 and 0.25, respectively, based on many such grid search results.

3.5 Catalog Amplitude Tomography (ML tomography)

In general we have taken the approach of using multiple independent approaches to measure seismic velocities and attenuation. Thus in an effort to test or validate our crustal attenuation from temporary broadband stations in the region we have begun to mine amplitude data from the official Chinese Earthquake Bulletin. The data from the Chinese Bulletin was also used to estimate crustal attenuation. This was done in a manner similar to Hearn et al., 2004. That study used data from the Annual China Bulletin of Earthquakes but was limited to only about 100 stations. In 2008 China began incorporating their sub-network data into their bulletin and now has over 1000 stations distributed across China. Bulletin data lists event locations, arrival times for both regional and teleseismic phases, and amplitude and period data for the purpose of

estimating ML, MS, MB, and Mb magnitudes. In this study we have used the ML amplitudes and periods.

The China Bulletin is an amalgamation of national network data and 28 sub-networks. Data was downloaded from the online website of China Earthquake Data Center (<http://data.earthquake.cn/data>) and contains data for events as small as magnitude 1.0. The online information does not list station locations. We obtained these from other sources both official and non-official. We also mass relocated stations using the source-receiver distances and azimuths in the bulletin. Best locations were chosen on the basis of the residuals and verified, when possible, by the use of Google Earth. Elevations were found using an API (Application Programming Interface) for Google Earth. Because the bulletin is a combined bulletin, there were many inconsistencies and blunders in the data set that had to be rectified.

We found most of the raw data to be useful but listed source-receiver distances and azimuths often were off. This occurs because the sub-network data was referenced to the sub-net location rather than the national location of the bulletin. In one case, for the Tianshan sub-network, the azimuth data made no sense at all. In addition, since sub-networks share data, there are sometimes multiple readings for each station and it is not clear which was used for the final location. For amplitude phases both the peak-to-peak amplitude and period were used (the reported period is the pulse-width at maximum amplitude). Amplitudes were measured using both velocity and displacement seismographs and designated as such. However, amplitudes were often reported using different units of nanometers, micrometers, and deca-nanometers (10^{-7} meters) without specifying which unit it was. Sub-network seismogram data was reported using deca-nanometers for the velocity seismograph readings and nanometers for the displacement seismograph readings. National network data was reported using nanometers through 2010 and micrometers from July 21, 2012 to present. Between these dates the units alternated and these data were excluded. We adjusted all data to nanometers before data analysis; however, since the inversion contains station gains any mistake about units will be absorbed into those terms.

3.6 Joint Inversion of Receiver Functions and Surface Waves

We used receiver functions from seventy-eight stations from the ASCENT and NETS arrays in joint inversions for the velocity models. We used the method described by Julia et al., 2000 with some minor modifications. Both phase and group velocities across the eastern plateau were used to interpolate velocities at the station's coordinates using a least mean squares approach. The phase velocity model was taken from Ceylan et al., 2012 and the group velocity measurements were taken from Pasyanos, 2010.

Receiver functions for each station were cut from 5 seconds before the P-wave arrival to 65 seconds after the first arrival. We used the method of Liggoria and Ammon, 1999 to compute the time domain receiver functions. The receiver files were then grouped and stacked according to their ten degree distance bins. This allowed us to model the normal move-out of the PS Moho phases to help constrain the velocity inversion. The events from 65° to 85° were grouped as one due to a lower number of files at these distances.

The events from 35° to 55° were put into 5° groupings as these files were much more numerous at these distances and to allow for easier processing. We used a Gaussian filter alpha of 2.5 for all receiver functions.

We chose to allow for more receiver file influence or weighting than dispersion (receiver function = 0.6; dispersion data = 0.4). The optimal smoothing parameter was found to be 0.7, which gave the best balance between producing a smoother velocity model and allowing for a reasonable fit to the receiver functions. We compiled all receiver functions and interpolated between all 70 stations in order to produce a three dimensional velocity model. The velocity models were then used to construct a velocity surface at 50 km, 80 km and 100 km to spatially evaluate the models in accordance with accepted theory.

4. RESULTS AND DISCUSSION

4.1 Two Plane Wave Rayleigh Wave Tomography

We used fundamental mode Rayleigh waves and two-plane wave tomography (TPWT) for phase velocity inversions (Forsyth and Li, 2005). We chose earthquakes with epicentral distances between 20° and 120° , depth ≤ 100 km, and $MS \geq 5.7$. We only used the vertical component in order to avoid shear and Love wave interference, and long period noise that may exist on horizontal components. The events with low signal to noise (S/N) ratios were eliminated visually. Our data was recorded at the INDEPTH-IV array (74 broadband stations), which was deployed across Northern Tibet. We also included data from the Namche-Barwa seismic array (Sol et al., 2007) in southeastern Tibet. Prior to data processing, all instrument responses were converted to the first generation STS2. We measured phase velocities for 13 frequency bands ranging between 20 and 143 s, and utilized 10-mHz-wide Butterworth filters centered on each frequency. In order to avoid dependence on earthquake magnitude, we normalized the seismic wave amplitude for each event, then measured phases and amplitudes of visually windowed data using Fourier analysis. We used a total of 174 earthquakes. In order to increase the reliability of our inversions, we only included events that were recorded by at least 10 stations.

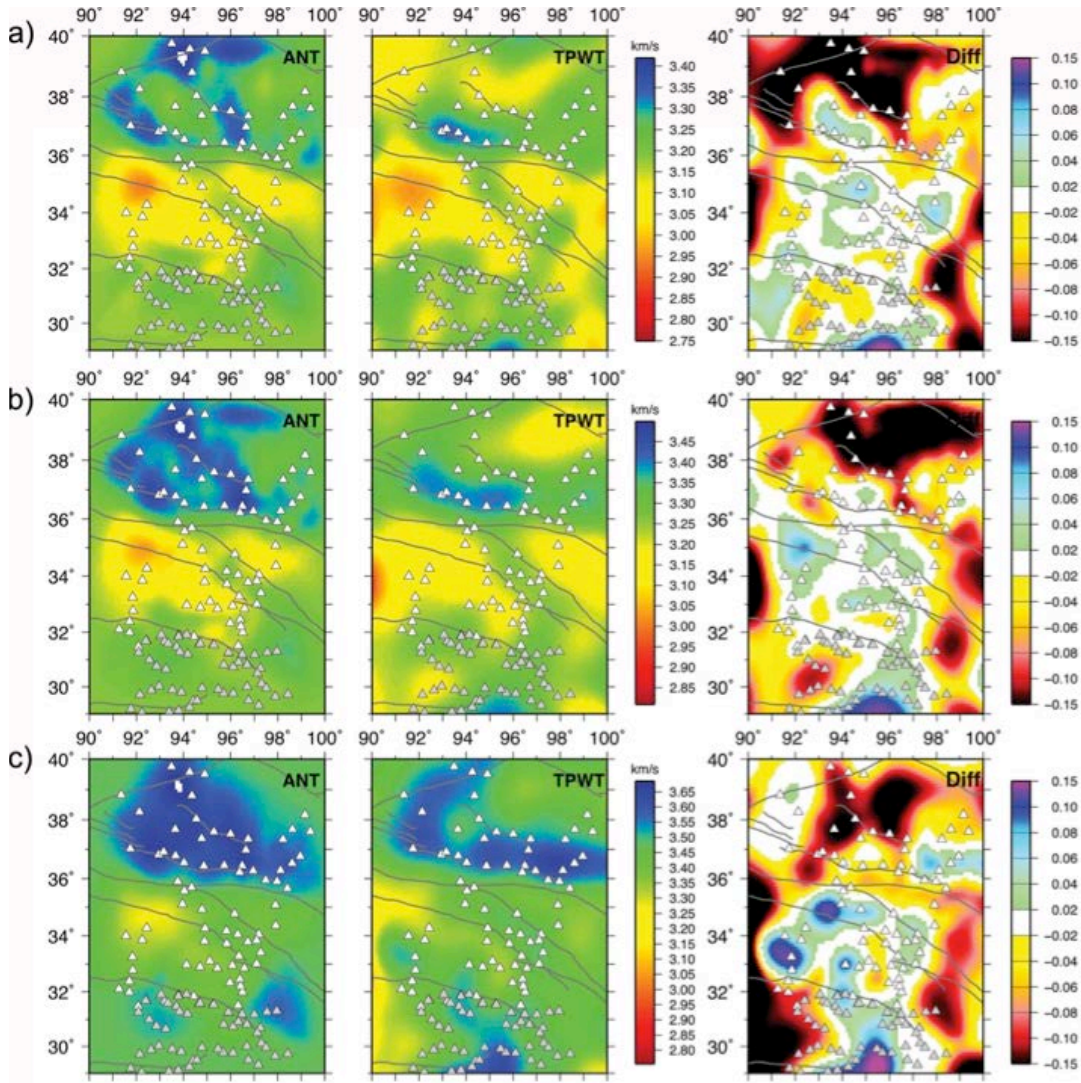


Figure 12. The difference between isotropic phase velocities obtained using ambient noise tomography (ANT) [Yang et al., 2010] and the two-plane wave approach (TPWT) for periods of a) 25, b) 30, and c) 40 s. *The third column shows the difference between the two methods in km/s. These results show that within the seismic array (with the exception of Qaidam Basin), phase velocities obtained by two methods are similar ($\sim \pm 0.06$ km/s).*

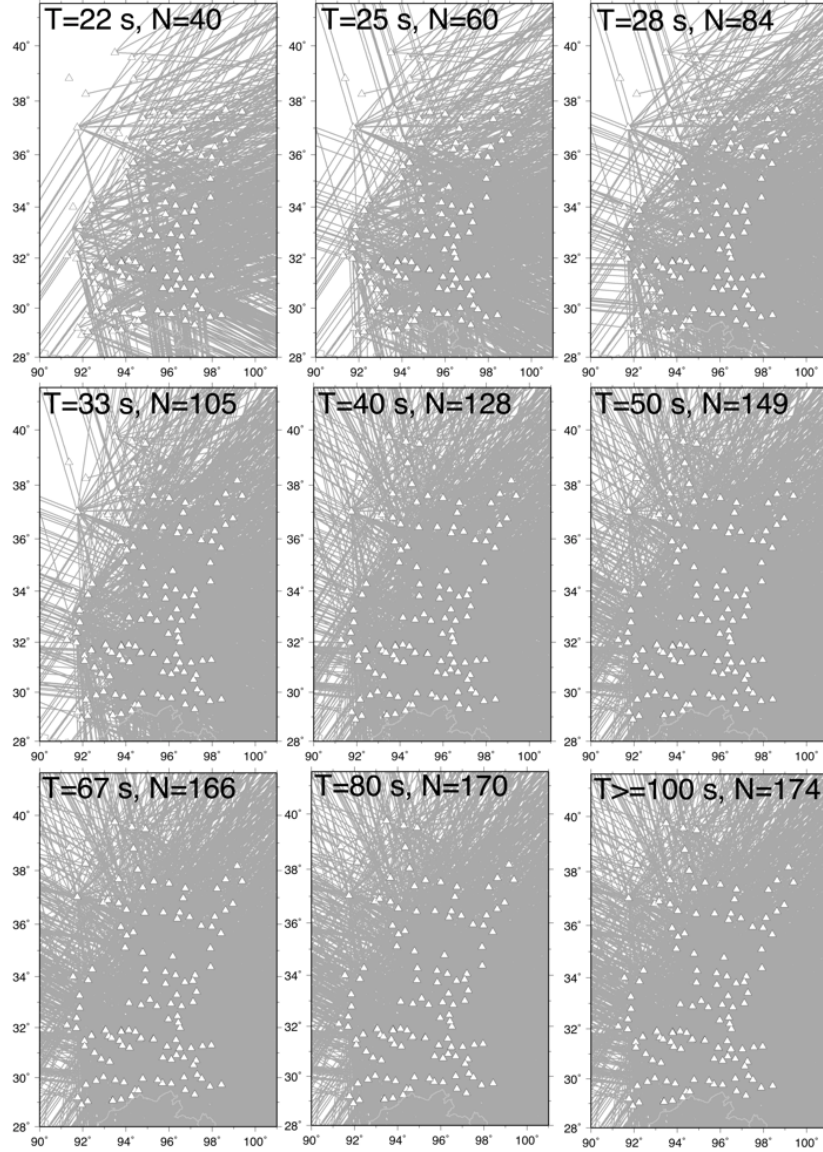


Figure 13. Ray path coverage for each period (T) with the number of events (N). Isotropic phase velocities are stable for $T \geq 25$ s (the periods with $N \geq 60$ earthquakes). *White triangles show the seismic station locations. For periods less than 40 seconds, there is not enough coverage on northwestern edge of our array.*

The first step in our inversions is calculating isotropic phase velocities for each frequency. Our experiments with TPWT show that ~ 60 events are enough to obtain stable results. In order to better constrain our inversion parameters (i.e. smoothing length and damping), we compared our results with those of Ambient Noise Tomography (ANT) (Yang et al., 2010). Although both methods measure surface wave dispersion, ANT and TPWT are fundamentally different and use independent data sets: TPWT implements surface waves created by earthquakes while ANT excludes earthquakes and uses ambient noise of the earth. Additionally, while ANT uses ray theory to obtain phase maps, TPWT assumes that distortion of wavefronts at each station can be expressed as the sum of two

plane waves (Forsyth and Li, 2005). Due to the short wavelengths of ambient surface waves, ANT can typically obtain more reliable results at crustal depths than TPWT. There is an overlapping frequency range between these two methods (in our case 20-50 s).

The comparison of isotropic phase velocities indicates that within the seismic array, these two methods reveal very similar results (differences less than ± 0.06 km/s with the exception of Qaidam Basin) for periods between 25 and 40 s (Figure 12). With the exception of 125 s (~ 170 km), the checkerboard tests (Figure 14) imply that resolution within the seismic array is ~ 150 km or better at all periods, sufficient to image all of the anomalies discussed in this study. Due to insufficient ray paths from the W-NW, the checkerboard tests exhibit evidence for some lateral smearing.

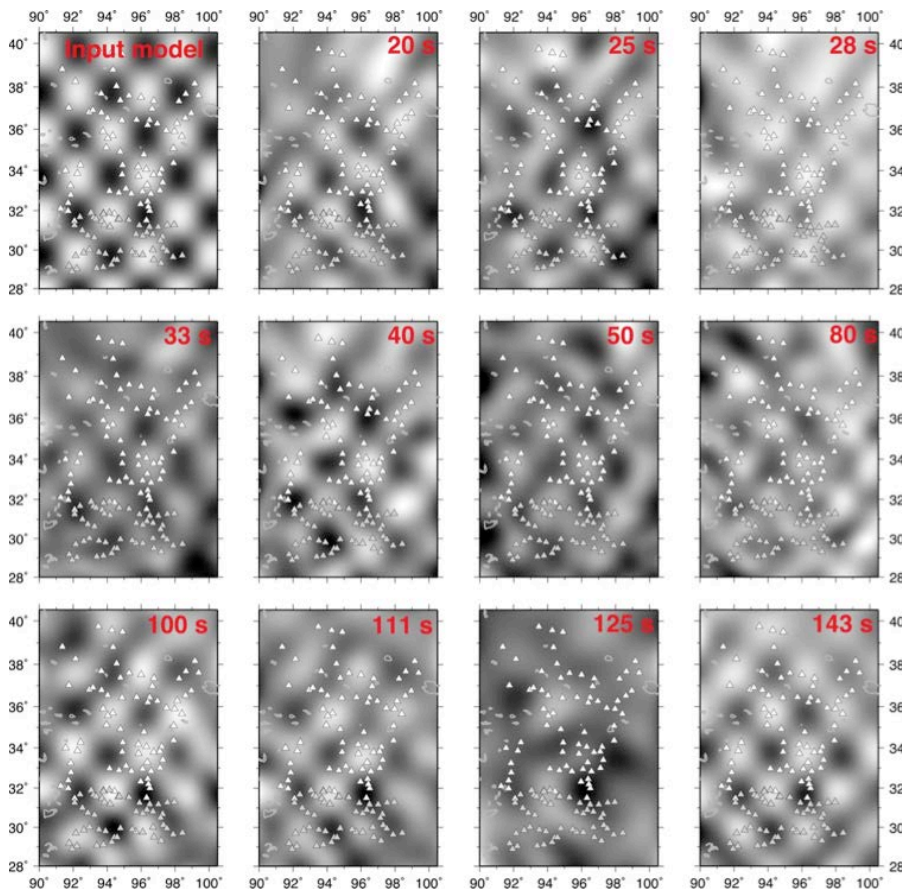


Figure 14. The resolution test results for different periods using checkerboard synthetic model. The anomalies in the input model are $1.5^\circ \times 1.5^\circ$. The periods are indicated in the upper-right corner of each panel.

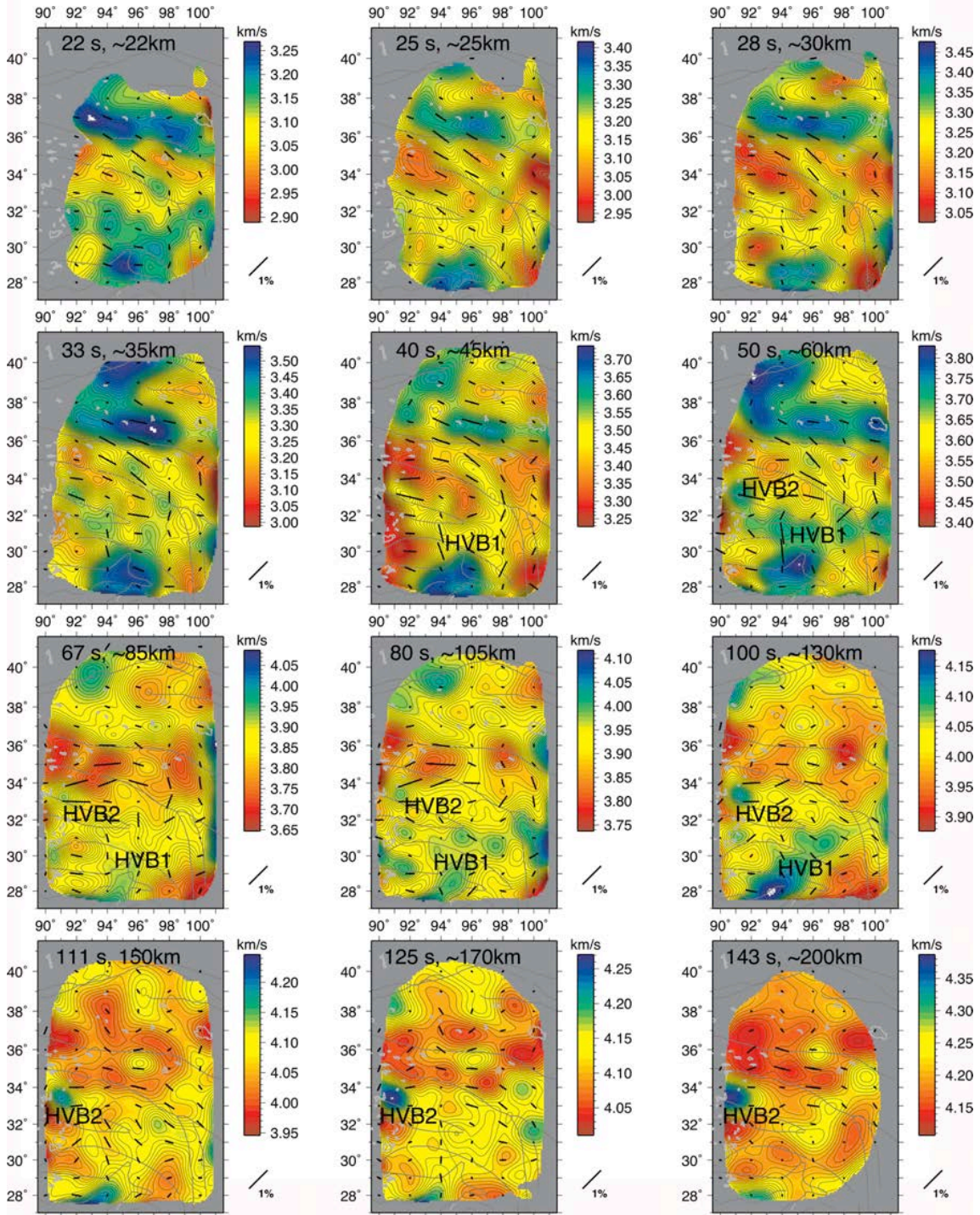


Figure 15. Anisotropic phase velocity maps for 12 periods (22-143 s). The solid black lines indicate azimuthal fast direction and amplitude of anisotropy. Note that color scales are different for each map. The regions with errors of $2\sigma \leq 0.06$ km/s (where σ is the standard deviation) are shaded. HVB1 and HVB2 show the high velocity bodies addressed in the text.

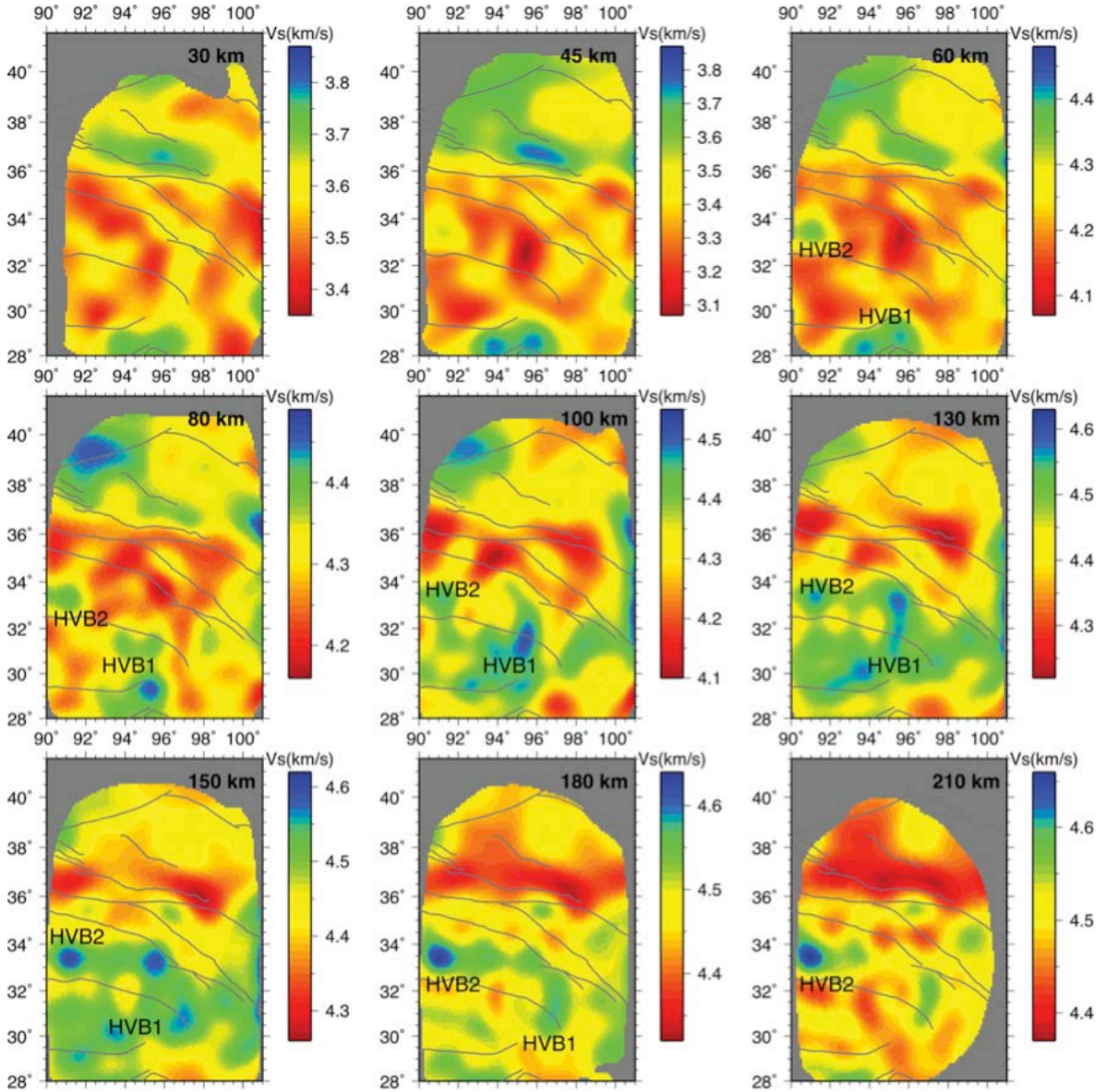


Figure 16. Shear wave velocities (km/s) for depths between 30 and 210 km. Depths are indicated on each panel. Note that each panel has a different color scale. The dark gray lines show major tectonic features. HVB1 and HVB2 show the high velocity bodies addressed in the text. The regions with errors of $2\sigma \leq 0.06$ km/s (where σ is the standard deviation) are shaded, based on peak depth sensitivity of corresponding frequencies.

The second step of phase velocity inversion includes determining anisotropic phase velocities and seismic fast directions (Figure 15). Unlike traditional ray theory, TPWT accounts for phase and amplitude changes. A disadvantage of this method is its sensitivity to finite frequency effects such as scattering and wave front healing (Hung et al., 2001; Nolet and Dahlen, 2000). To overcome these limitations, we employed 2D sensitivity kernels [Yang and Forsyth, 2006] for both amplitude and phase perturbation for each period. Azimuthal anisotropy was simultaneously solved with Rayleigh wave

phase velocities. Because the shortest wavelength for our data is ~65 km (for 20 s period and taking the average phase velocity as 3.18 km/s), we used a constant smoothing length of 80 km for all periods.

In order to reduce the effects of this trade-off, we used high damping both for anisotropy and phase velocities. We tested our inversion results by using a variety of damping values. However, the final choice of damping parameter was made considering model uncertainties (Figure 20) and consistency with ANT results. Moreover, the features we discuss here are consistently observed in all inversions regardless of damping. Additionally, to increase reliability, we only interpret phase velocities with errors of about 0.06 km/s , where σ is the standard deviation.

The third and last step of the inversion is obtaining shear wave velocities (Figure 16) using the anisotropic phase maps from the second step. For shear wave inversions, we used the partial derivatives from Saito [1988]. For the initial model, the AK135 model was adapted to our region by taking average Moho depths of 45 and 60 km for Qaidam Basin and the rest of the region (Zhu and Helmberger, 1998), respectively.

We defined 50 layers for shear wave inversion from the surface to 400 km depth. According to Li (2011), who used a similar frequency range with less data, the shear wave structure cannot be determined precisely at all layers, but the average velocity for each defined layer can be resolved for depths less than 250 km. Therefore, we do not interpret our results for depths $> 200 \text{ km}$.

Figures 15-16 show our tomographic models for Rayleigh wave phase and shear wave velocities. Starting from the south, we observe a high velocity body (HVB1) along the BNS and further south, between the depths of ~60 and 170 km. This feature is highly heterogeneous in the east-west direction with a shear wave anomaly of $\geq 2\%$. Furthermore, the phase velocity maps (Figure 15) show regions of relatively low velocities within the HVB1. The shear wave anomaly cross-sections show that the HVB1 has a sub-horizontal geometry dipping northwards slightly beneath the BNS, between ~94E and 97E. A further isolated high velocity body (HVB2) is observed at ~91E-33N which appears to be connected to the HVB1 beneath the BNS at ~130-150 km, becoming isolated again at greater depths. This vertically continuous feature starts at ~60 km depth (50 s) and gradually increases in diameter to depths greater than 200 km (Figures 15 and 16).

Further north, low velocities characterize the uppermost mantle beneath the N. Qiangtang and Songpan-Ganzi. The shear wave velocities are ~4% slower than those observed beneath the Lhasa block and southern Qiangtang terrane (Figure 14). Anisotropic fast directions across the northern and southern branches of the Kunlun Fault tend to conform to strikes of the active faults. We also observe the largest amplitude of azimuthal anisotropy across these shear zones. Seismic anisotropy appears to be consistent at depth with the exception of the southeast portion of our region. Similar to shear wave splitting measurements (Huang et al., 2000; León Soto et al., 2012), azimuthal fast directions exhibit a general clockwise rotation (Figure 15).

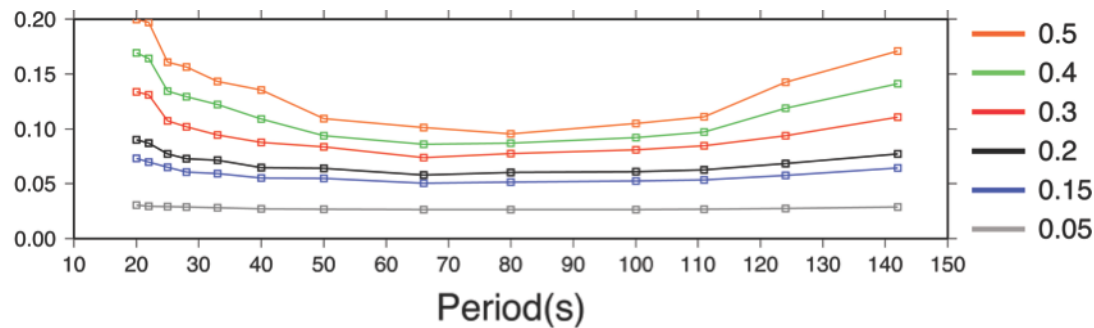


Figure 17. Standard Error (left vertical axis) vs. period for different damping parameter values. Color codes are shown in the figure legend. Note that the damping and damping parameter are inversely proportional (i.e. lower damping parameter values mean higher damping). As expected, model misfits decrease as damping increases (damping parameter decreases). Considering the consistency between ANT and TPWT results, and the model misfits, we determined that 0.2 is the most suitable damping parameter value. Moreover, all features discussed in the manuscript are consistently observed in all inversions.

Both phase maps and S wave anomalies (Figures 15 and 16) show ~1% higher velocities, indicating thicker (~130-140 km) and possibly rigid lithosphere beneath the Qaidam Basin. We also observe the eastern edge of the Tarim Basin. In approximate agreement with the lithosphere-asthenosphere boundary (LAB) phases of S-wave receiver functions [Zhao et al., 2011], the Tarim Basin has a lithospheric thickness of ~200 km, while the Qaidam Basin is substantially thinner. Beneath the Kunlun Shan, south of Qaidam Basin, we observe low velocity zones that are concentrated along the northern and southern branches of the Kunlun Fault, extending deeper than 200 km.

Comparisons with independent phase maps using ambient noise (Yang et al., 2010) suggest that we are able to measure the phase velocities with a high degree of precision (differences less than 0.06 km/s within the array, Figure 12). Furthermore, unlike previous surface and body wave measurements (Li et al., 2008), our shear wave observations are broadly consistent with those obtained using body wave tomography (Liang et al., 2012). Moreover, the comparison of the splitting data from León Soto et al. (2012) and our azimuthal fast directions for 143 s shows that average differences are ~1 degree and 10 degrees for Qiangtang and Songpan-Ganzi, respectively (Figure 15).

4.2 Pn and Sn Travel Time Tomography

We created a reliable tomographic model for the Pn velocity structure in western China including station corrections or crustal delay times (Figures 18 and 19). Data from recent INDEPTH IV and other broadband deployments in Tibet are used to invert for crustal delays and Pn velocities beneath the eastern Tibetan Plateau and surrounding regions. Several similar high velocity regions occur north of the eastern Himalayan syntaxis beneath the Lhasa, Qiangtang, and Songpan-Ganzi terranes. We interpret these as underthrust Indian continental lithosphere segments. The east-west variability of Pn velocity beneath the Himalayas and southern Tibet indicates that the underthrust Indian continental lithosphere is not a homogeneous body. Qaidam Basin along with the Gonghe and Xining Basins east of it show an east-west high velocity anomaly. The Indian lithosphere extends roughly half-way into the Tibetan plateau, with more penetration north of the eastern syntaxis.

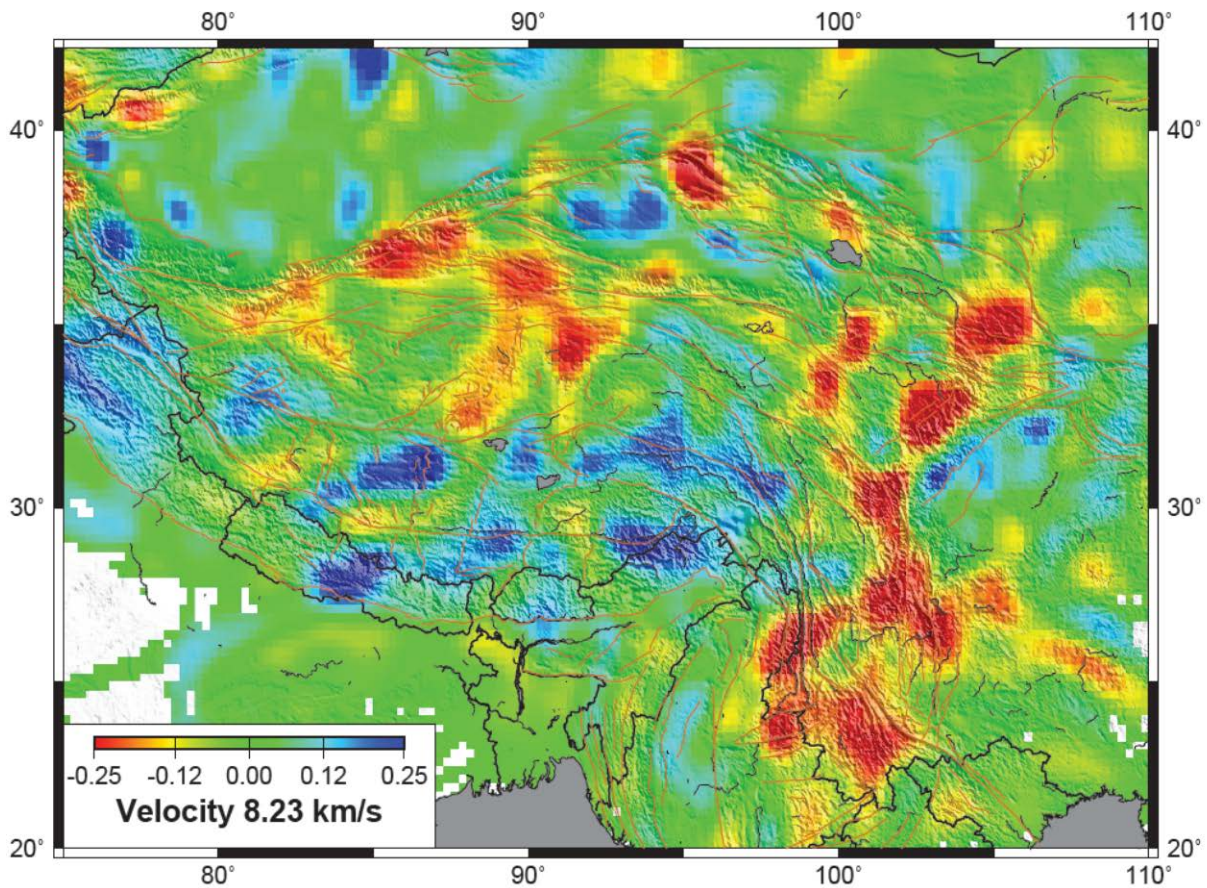


Figure 18. Our final tomographic Pn velocity model for ray paths between 3 and 15 degrees using data from the Chinese National catalog as well as picks from all temporary stations deployed throughout the Tibetan plateau.

Our previous Pn tomography studies showed a contrast between high velocities beneath southern Tibet and low velocities beneath northern Tibet, but we now find that this model is oversimplified. Longer ray paths show a vastly different velocity structure than do the shorter ray paths; thus there is significant vertical variation in the velocity structure of the mantle lid. Only longer ray paths show low velocity beneath northern Songpan-Ganzi

terrane, but are not coincident with the Bangong-Nujiang suture that separates northern and southern Tibet. There is also low velocity mantle beneath the northeast Songpan-Ganzi Terrane (in Gansu province). Shorter ray paths image the top of the mantle lid and show two distinct high velocity zones beneath the Himalayas.

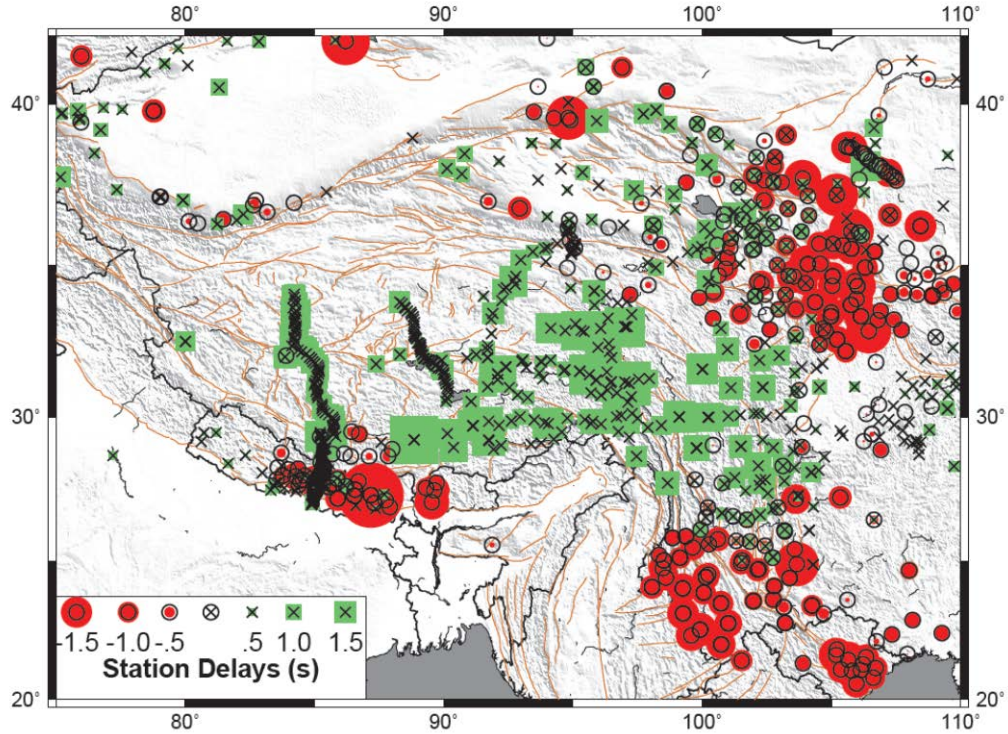


Figure 19. Our final list of average station delays for all stations used to construct the tomographic model shown in Figure 18.

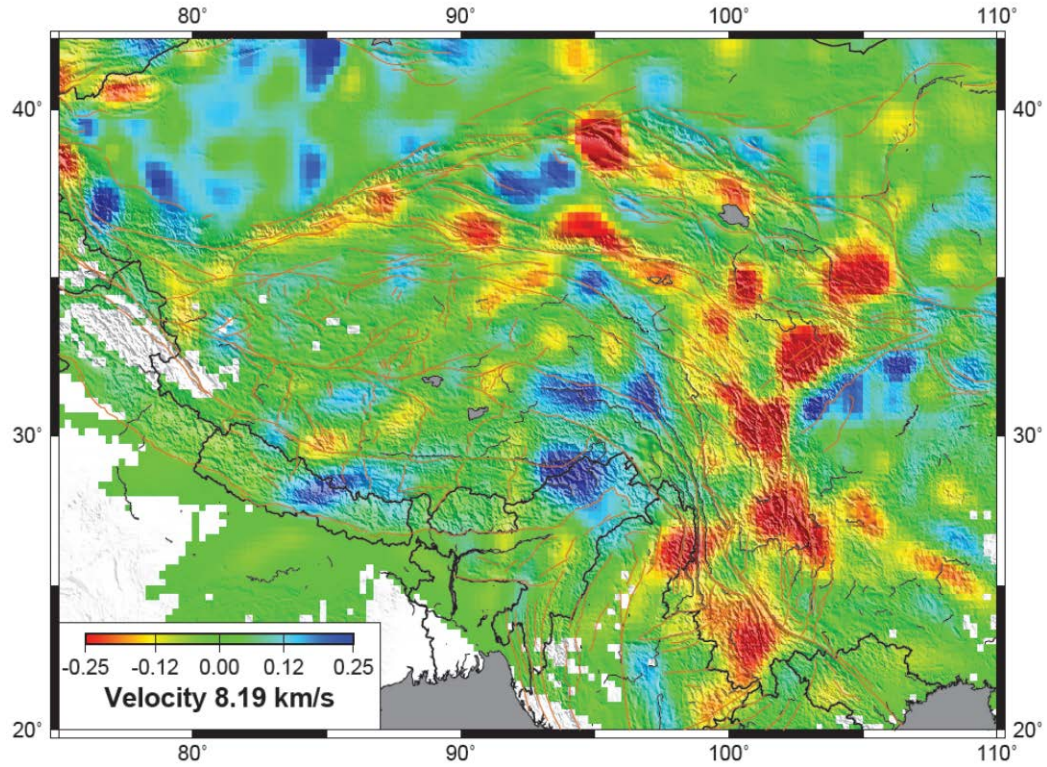


Figure 20. Our final tomographic Pn velocity model for ray paths between 3 and 9 degrees.

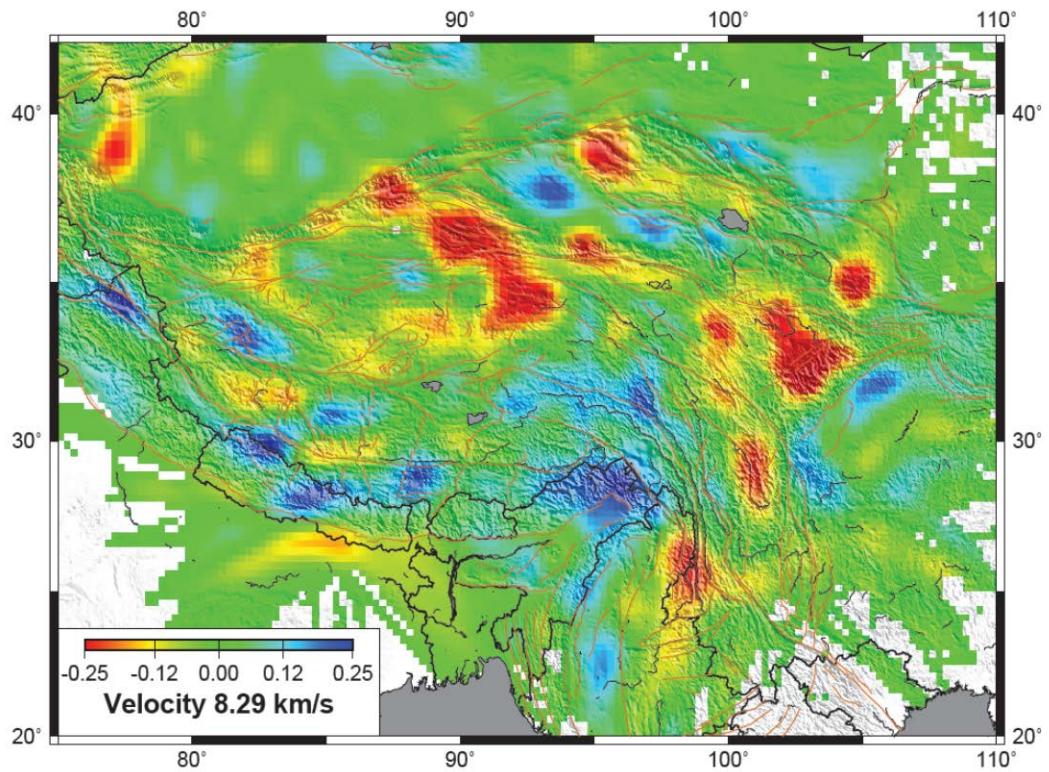


Figure 21. Our final tomographic Pn velocity model for ray paths between 6 and 12 degrees.

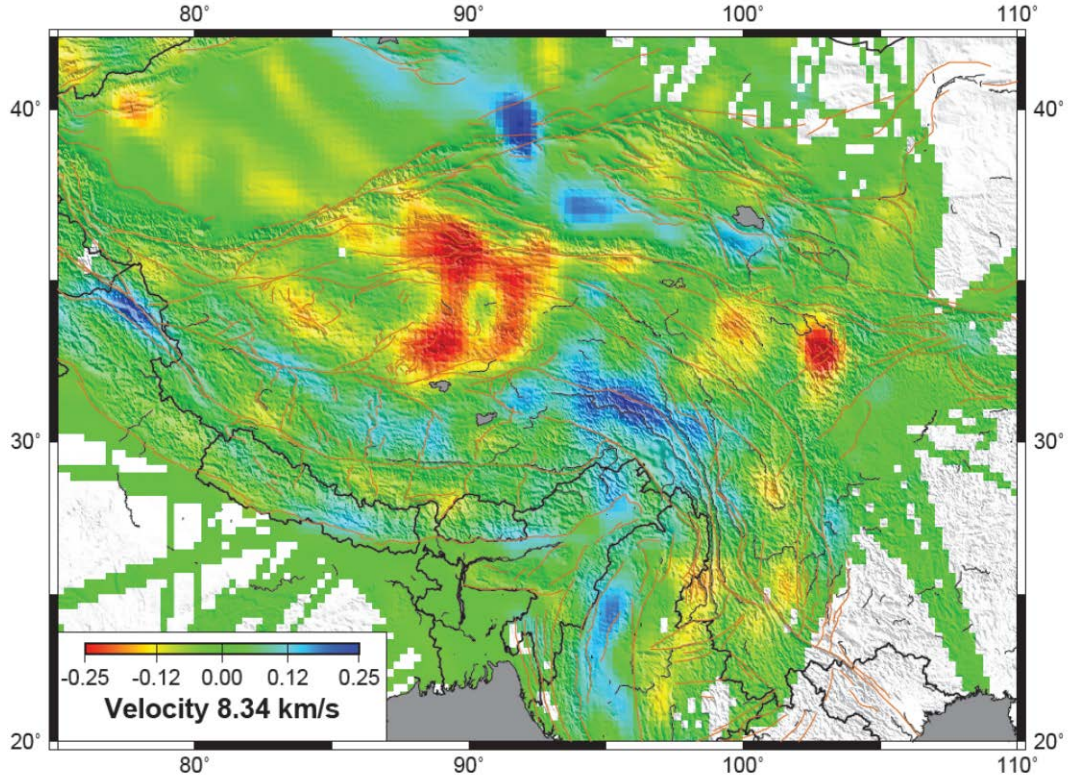


Figure 22. Our final tomographic Pn velocity model for ray paths between 9 and 15 degrees.

In addition to mapping variations in Pn velocity we have also created a model for Sn velocities across much of China and eastern Tibet. Furthermore, in order to be able to constrain V_p/V_s , a key parameter for earthquake location, for this region we have extracted only those earthquake-station pairs with both Pn and Sn travel time picks. This will allow us to directly compute V_p/V_s because the resolution of the two tomographic models should be very similar. In order to test this further, however, velocity resolution tests were performed to determine the size of features that can be reliably imaged, and therefore interpreted. Checkerboard tests were conducted to evaluate the effects of ray coverage on spatial resolution. A test checkerboard velocity model was created by assigning sinusoidal velocity anomalies to the cells of the model domain simultaneously. Synthetic arrival times were calculated for the test model under different checkerboard sizes with the same number of earthquakes, stations, and ray paths that are used for actual tomographic inversion. Gaussian noise was added to the synthetic travel times and Gaussian distributed errors with a standard deviation of 15 km were added to the event locations to simulate location errors.. We performed tests using different cell sizes for the sinusoidal velocity anomalies. The spatial resolution is considered to be good for the regions in which the checkerboard pattern is recovered. The tests indicate that, for most of the study region, velocity anomalies with a size of $2.7^\circ \times 2.7^\circ$ can be well resolved, and at the western part of the study area, the spatial resolution can reach $2.0^\circ \times 2.0^\circ$ or even better.

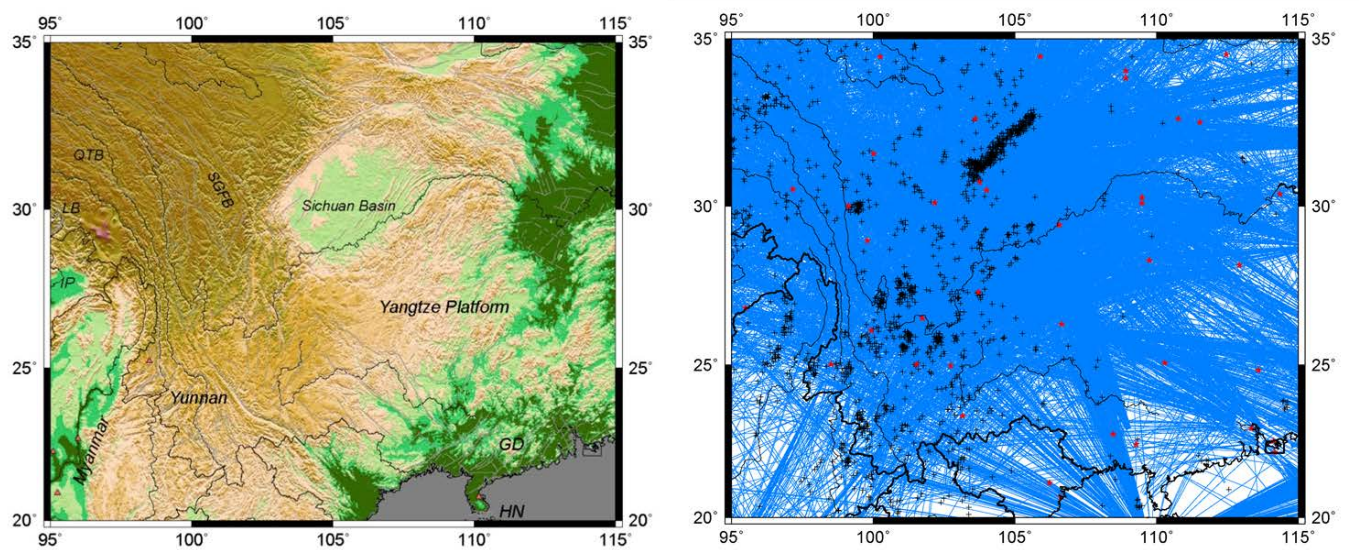


Figure 23. A map of eastern Tibet showing the major physiographic features (left) and a plot of the ray path coverage where we observe both Pn and Sn arrival times (Lü et al, 2012).

For the inversion for V_p/V_s for the uppermost mantle, we used the Pn and Sn phase data for epicentral distances between 3° and 16° . We show the ray path coverage in Figure 23. The initial models were obtained by a fit to the travel time–distance curve considering the effect of the global curve. The average Pn and Sn velocities of the upper layer are 8.10 km/s and 4.60 km/s and those of the deeper layer are 8.19 km/s and 4.65 km/s, respectively (Figures 24 and 25). The travel time residuals (difference between predicted and reported travel times) used in the study were limited to a range of ± 5 s.

In general, the Pn and Sn velocity variation patterns are similar to those obtained in the model of the upper layer discussed above. High velocity values are observed beneath the Sichuan Basin and the Indian plate; low velocities are found to be distributed under the Myanmar–Yunnan region, Hainan region, and the Songpan–Ganzi fold belt. Four independent datasets of the inversion of the Pn and Sn travel time data yielded similar results that are consistent with each other, and this confirm the credibility of the inversion results.. In our model, there is a clear velocity difference between the southern and the northern parts of 26° N in the Yunnan region. Low velocities are found south of 26° N.

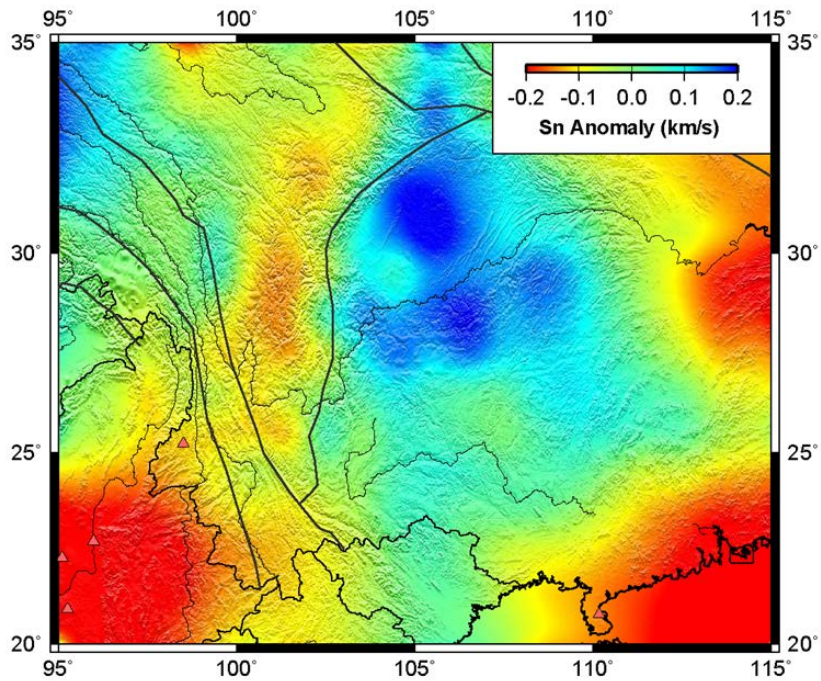


Figure 24. Sn lateral velocity variations for the uppermost mantle layer. The average Sn velocity is 4.60 km/s.

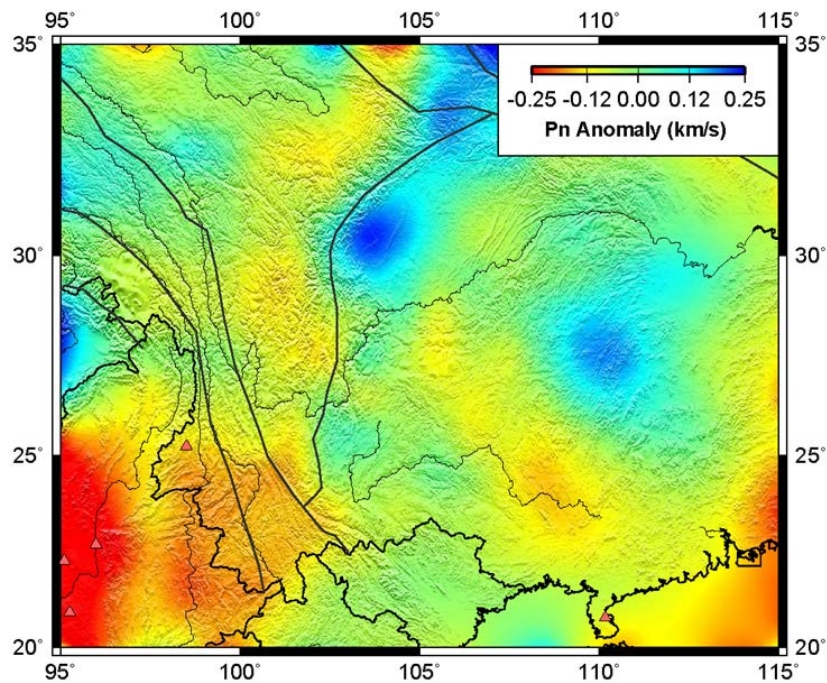


Figure 25. Pn lateral velocity variations for the uppermost mantle layer. Average Pn velocity is 8.10 km/s.

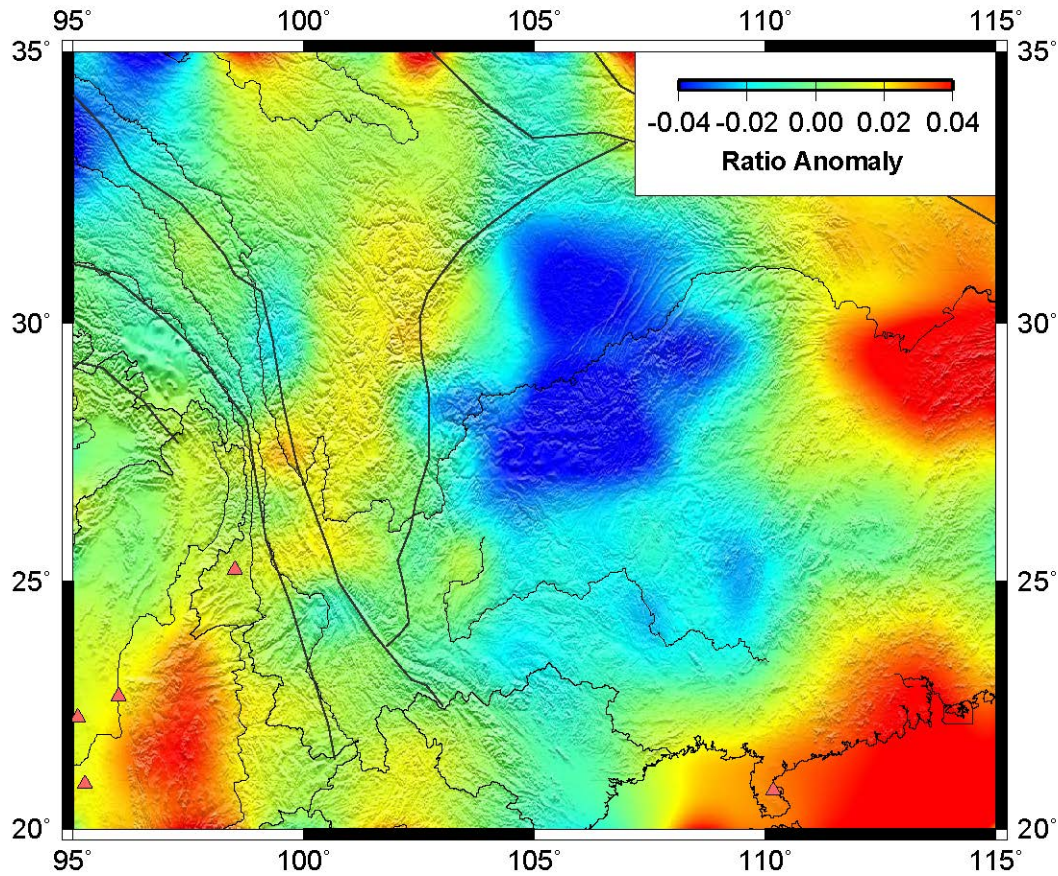


Figure 26. A tomographic model of the V_p/V_s ratio for the uppermost mantle beneath eastern Tibet and the surrounding regions. Average velocity ratio is 1.76. Red and blue areas correspond to ratios higher and lower than the average, respectively.

Figure 26 shows the V_p/V_s ratio distribution. The average ratio is approximately 1.76 beneath the study area. The velocity ratio distributions are generally similar for both the Pn and the Sn models. The velocity ratio is low in the Sichuan Basin. In the Myanmar–Yunnan and Hainan regions, the velocity ratio is considerably high, indicating that the uppermost mantle had a high temperature. In the Yunnan region, there are some differences in the velocity ratio distributions between the two layers. From the heat flow observation (Wang and Huang, 1990; Hu et al., 2001) and crust velocity structure studies (Gao et al., 2009; Wu and Zhang, 2012; Xu et al., 2012), we infer that the hot material upwelling is not vertical but is more complex beneath the Yunnan region. For the upper layer, Pn and Sn were determined using by rays with epicenter distances between 3° and 10°. The average Pn and Sn velocities of this layer are 8.10 km/s and 4.60 km/s, respectively. The average V_p/V_s ratio is approximately 1.76 beneath the study area. The RMS residuals of the Pn travel times decreased from 2.0 s to 1.1 s after inversion, and the residuals of Sn travel times decreased from 2.2 s to 1.3 s. In general, the variations of the Pn and Sn velocities are similar. High velocity values are observed beneath the Sichuan

Basin and the Indian plate. Clear low velocities are found under the Myanmar–Yunnan region, the Hainan region, and the Songpan–Ganzi fold belt.

At the Indian plate at the west of the eastern Himalayan syntaxis and the Sichuan Basin, the Pn velocity is clearly high for both layers. The model shows that the lithospheres of these regions are cold and stable. The stable lithospheres of the Sichuan Basin block the material flow from the Tibetan Plateau to the east and change the flow direction to the south. In the Myanmar–Yunnan region, low Pn velocities are distributed around some volcanoes (Lei et al., 2009a). These results serve as further evidence of the subduction of the Indian plate beneath the Myanmar–Yunnan region (Li et al., 2008), which caused the back-arc upwelling. In the Hainan region, mantle plumes were found using body-wave tomography (Lei et al., 2009b). Our inversion models also support this discovery. The Pn velocity under the Songpan–Ganzi fold belt is significantly low, which has also been observed in previous studies (Liang et al., 2004; Pei et al., 2007). This low velocity can be primarily attributed to high temperatures, and secondarily to compositional variations due to water (Hearn et al., 2004).

In general, the Pn and Sn velocity variation patterns are similar to those obtained in the model of the upper layer discussed above. High velocity values are observed beneath the Sichuan Basin and the Indian plate; low velocities are found to be distributed under the Myanmar–Yunnan region, Hainan region, and the Songpan–Ganzi fold belt. Four independent datasets of the inversion of the Pn and Sn travel time data yielded similar results that are consistent with each other, and this confirms the credibility of the inversion results. A previous study involving an SKS analysis revealed that the fast direction of the SKS north of 26° N is N–S and south of 26° N is W–E (Sol et al., 2007). In our model, there is a clear velocity difference south and north of 26° N in the Yunnan region, with low velocities south of 26° N. Considering the previous SKS and Pn anisotropy results (Cui and Pei, 2009), we infer that the regions south and north of 26° N in the Yunnan region are controlled by different dynamic processes. The southern part is affected by the eastward subduction of the Indian plate; the northern part is affected by material flow from the Tibetan Plateau (Zhang et al., 2010; Bai et al., 2010).

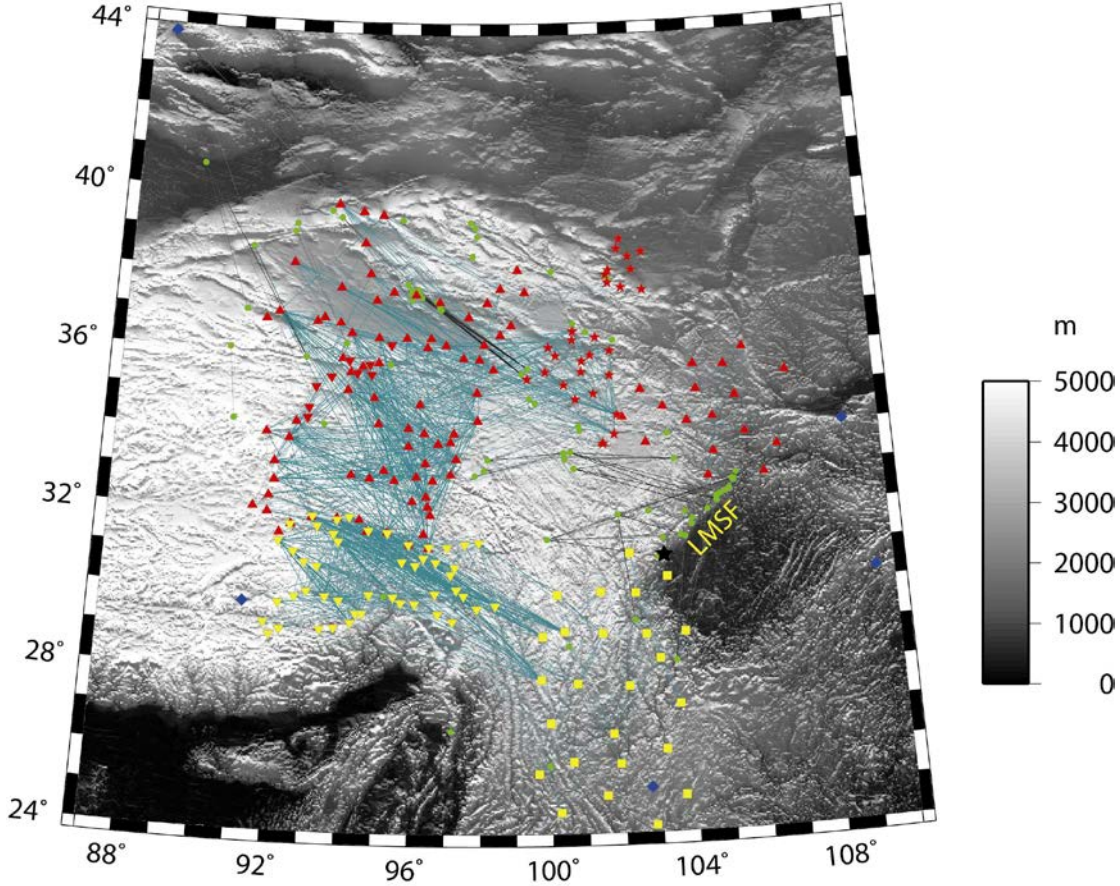


Figure 27. Map showing seismic stations, regional seismic events, and two-station or two-event paths in this study. Yellow inverse triangles represent the Namche Barwa experiment; yellow squares represent the MIT-China experiment; red triangles represent the INDEPTH-IV-ASCENT experiment; red inverse triangles represent the INDEPTH-IV-UK experiment; red stars represent the NETS experiment; blue diamonds represent the permanent network IC; green circles represent events. The cyan and black lines represent RTS and RTE paths at 1 Hz, respectively. The epicenter of the Wenchuan earthquake is marked by black star, and the Longmenshan fault (LMSF) area is noted. Elevation is shown with a gray scale.

4.3 Lg and Pg Q Tomography

We used more than 16,000 Lg spectra combined to form 12,000 Reverse Two Station (RTM) paths that cover most of the eastern Tibetan plateau. We analyzed Lg spectra between 0.5 Hz and 2 Hz, which typically represents the predominant frequency range for Lg phases travelling through tectonically active crust. We have selected 16 different frequency bands within this predominant frequency range using a perturbation of 0.1 Hz, a starting central frequency of 0.5 Hz, and an ending central frequency of 2.0 Hz. We used a bandwidth of 0.8 Hz for each of these frequency bands. A moving average is used to smooth each spectrum, and a cubic spline interpolation is used to replace unstable data points if at least 80% of the number of data points for a spectrum fall within an order of magnitude of the smoothed spectrum.

The study area is divided into square two dimensional cells with a size of $0.5^{\circ} \times 0.5^{\circ}$ for our tomographic model. A set of maps of path density (i.e. hit counts) have been built for all 16 frequency bands. The densest path coverage is found within an area where the Namche Barwa, western portion of ASCENT, INDEPTH-IV-UK, and NETS were deployed, which is also consistent with the retrievable area of $2^{\circ} \times 2^{\circ}$ anomalies in our resolution tests (Figure 10). In terms of the tectonics, this area mainly consists of the Qaidam Basin (QB), Songpan-Ganzi terrane (SGT, or Bayan Har block [e.g., Vergne et al., 2002]), Qiangtang terrane (QT), Lhasa terrane (LT), and Eastern Himalayan Syntaxis (EHS) (Figure 33).

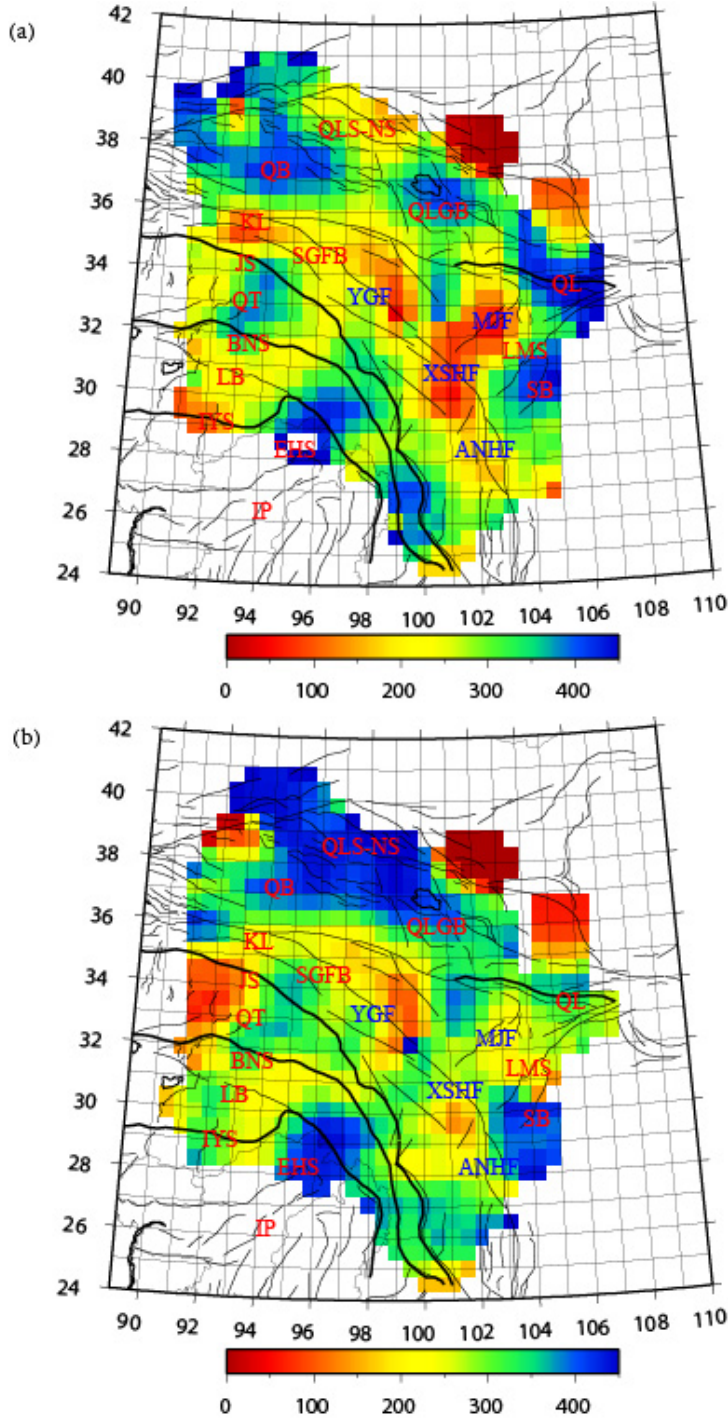


Figure 28. Q_{Lg} (a) and Q_{Pg} (b) tomographic images at 1 Hz. Thin solid lines represent faults, and thick lines represent tectonic sutures. ANHF: Anninghe Fault; BNS: Bangong-Nujiang Suture; EHS: Eastern Himalayan Syntaxis; IP: Indian Plate; IYS: Indus-Yalu Suture; JS: Jinsha Suture; KL: Kunlun mountain belt; LB: Lhasa Block; LMS: Longmenshan mountain belt; MJF: Minjiang Fault; QB: Qaidam Basin; QLGB: Qinghai Lake-Gonghe Basin; QL: Qinling mountain belt; QLS-NS: Qilian Shan-Nan Shan Mountain belt; QT: Qiangtang Terrane; SB: Sichuan Basin; SGFB: Songpan-Ganzi fold belt; XSHF: Xianshuihe Fault; YGF: Yushu-Ganzi Fault.

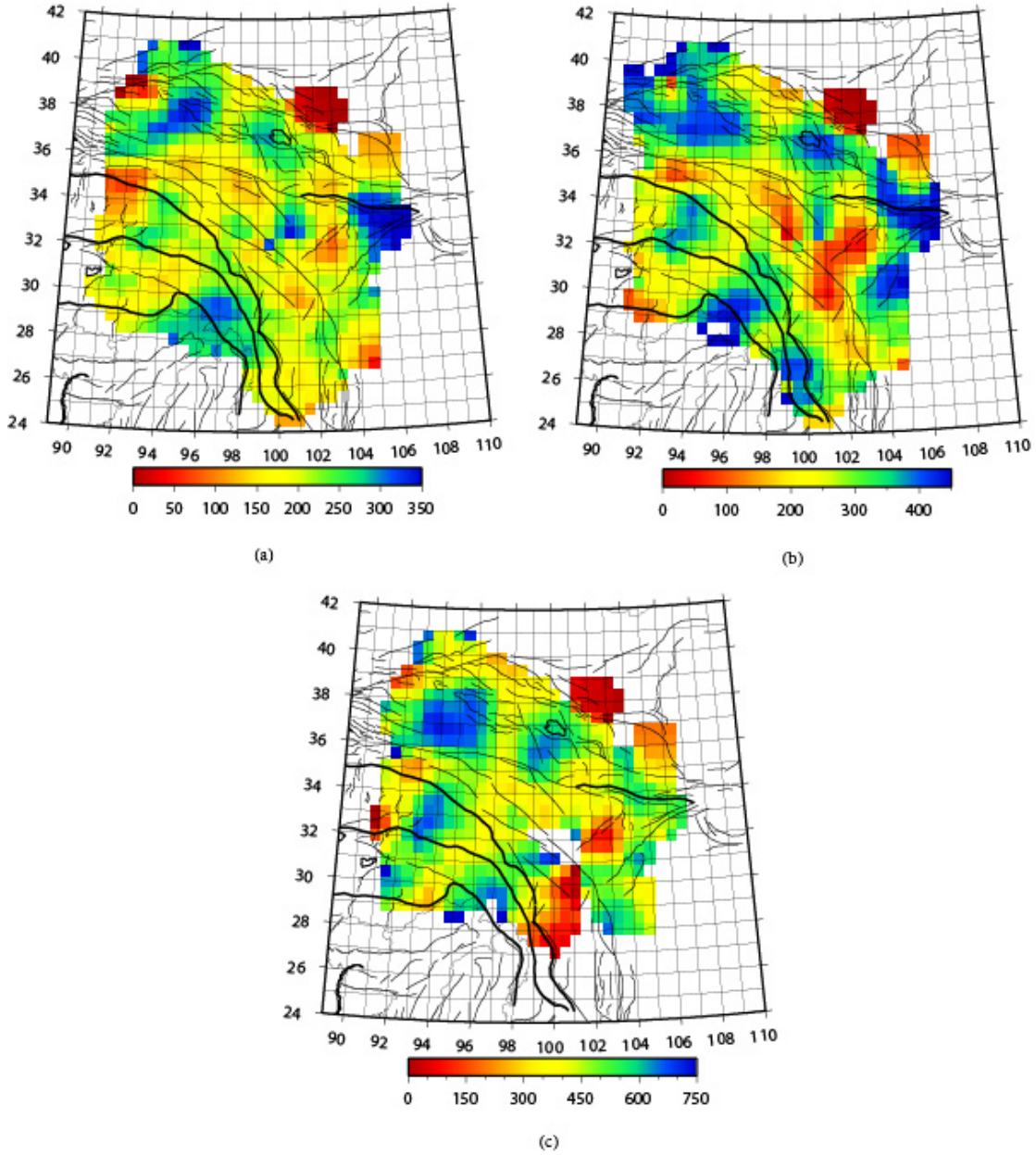


Figure 29. Models of Q_{Lg} at 0.5 Hz (a), 1 Hz (b), and 2 Hz (c).

A high Q_{Lg0} zone is located near the Eastern Himalayan Syntaxis (EHS) and probably extends eastward to the Bangong-Nujiang Suture (BNS) in the southeastern TP (Figure 28), which was also observed by Li et al., 2008. The Kunlun mountain range is at the northern margin of the TP, where we observe a nearly continuous E-W very low Q_{Lg0} “band” that divides the high Q_{Lg0} Qaidam Basin and low to middle Q_{Lg} central TP. Another low Q_{Lg} zone, nearly along the western Longmenshan thrust belt, laterally divides the high Q_{Lg} Sichuan Basin and the low to middle Q_{Lg} eastern TP.

Theoretical studies suggest that a complex velocity structure leads to scattering attenuation and regional phase mode conversion when Lg propagates in a strongly heterogeneous crust (e.g., Kennett, 1989). But practically, large numbers of studies of Lg propagation imply that the Q_{Lg} is a good approach for crustal shear wave Q_s , and that scattering plays only a minor role and is probably negligible at low frequencies (Herrmann and Kijko, 1983; Mitchell, 1995; Sarker and Abers, 1998; Jemberie and Nyblade, 2009). We only see Lg frequencies lower than 10 Hz in our study, which suggests that the conditions of measuring Q_{Lg} and its frequency dependence are similar to the studies referenced above. Meanwhile, focusing and defocusing, especially lateral refraction, probably affects the fundamental assumptions of the RTM and the accuracy of tomographic modeling (Mitchell, 1995). However, the mechanism of focusing and defocusing is mostly caused by small-scale velocity anomalies, probably less than 10 km (Sarker and Abers, 1998), which is secondary and probably negligible for measurements from relatively longer paths such as our minimum inter-station distance of 150 km. Thus the lateral variation of Q_{Lg0} probably represents the lateral variation of crustal Q_s , and furthermore contains information about geothermal structures and active tectonics in the crust (e.g. Mitchell, 1995).

Our observations of high Q_{Lg0} zones, such as the Qaidam Basin, probably represent tectonically relatively stable crust with low temperatures. The very low Q_{Lg0} band along the Kunlun mountain range dramatically corresponds with Cenozoic volcanic fields developed during Indo-Asia Collision (Yin, 2010) and regions with high horizontal shear strain rate modeled from Quaternary fault slip and GPS measurements (Holt et al., 2000); this correlation suggests a relationship among high shear strain rate, young volcanism, and Q in the crust. Unlike prior studies noting that the Qiangtang crust perhaps contains partial melting in northern Tibet, our model suggests that the high shear strain accumulated in the crust of the Songpan-Ganzi fold belt and Kunlun leads to high temperature, and possibly partially molten crust.

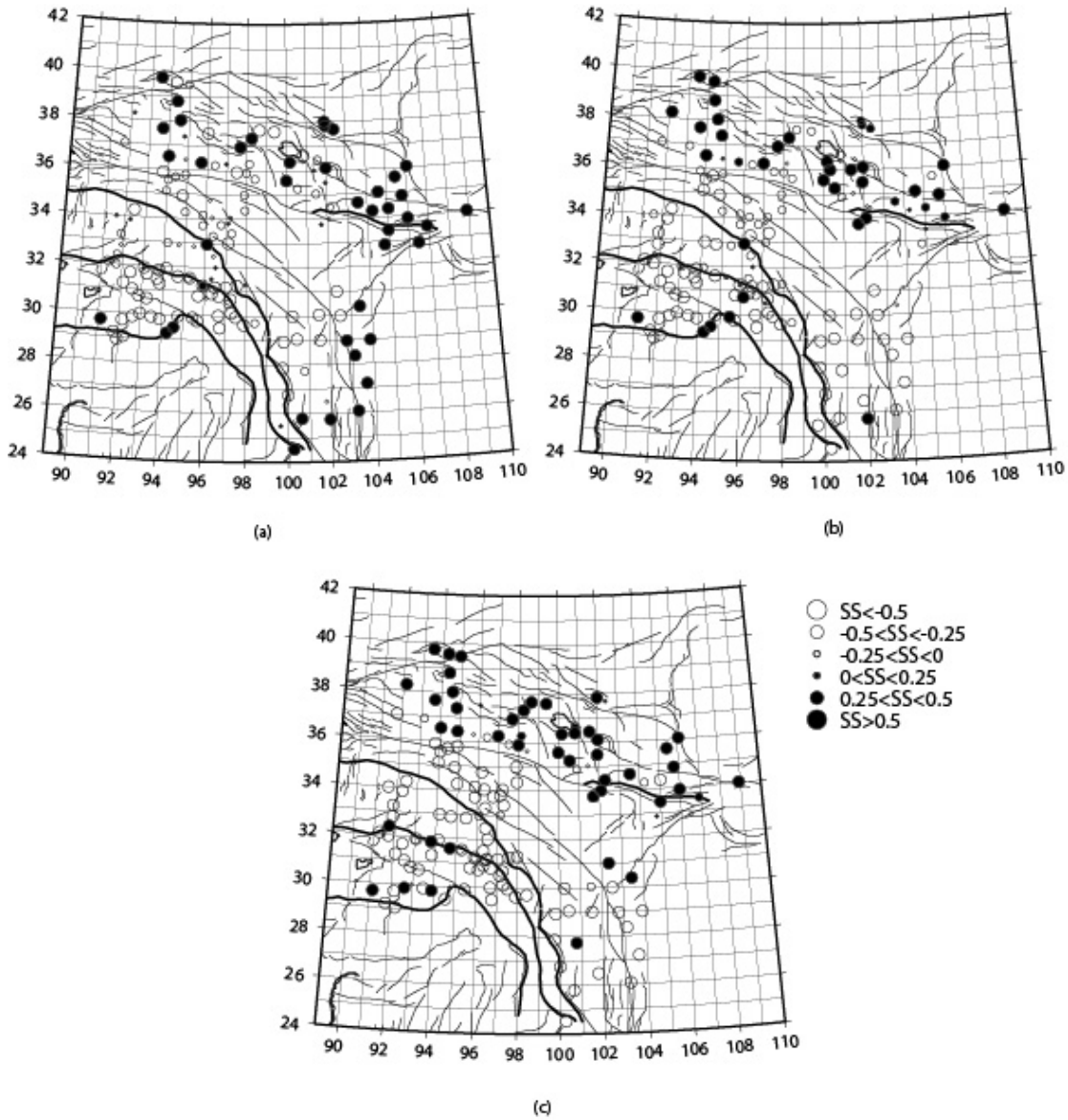


Figure 30. Lg site term maps at frequencies of 0.5 Hz (a), 1 Hz (b), and 2 Hz (c). We observe significant site term differences between the Tibetan Plateau and major basins, probably dependent on topography or sedimentary thickness.

We also observe that the site responses have a very strong spatial structure across the TP; we consistently observe high site amplification values within the Qaidam Basin and low amplification values within high TP (Figure 30). This does not correlate with any difference in instrument response or suggest a potential artificial effect from deployment style. There is no contradiction between the pattern of lateral variation of measured site response in this study and the assumption of the frequency dependency of site responses (e.g., Huang et al., 2005) because we calculate relative site terms. But such a regular pattern is unlikely consistent with the assumption that the site responses are strongly dominated by near-surface shear wave velocity and seismic structures (Rodgers et al., 2006), and its lateral variation does not correspond with the distribution of different

geological strata. In contrast, this pattern shows strong evidence that the site amplification is dependent on topography (Zhang and Lay, 1994) or sedimentary thickness (Mitchell and Hwang, 1987). This suggestion also helps to explain the different Q_{Lg0} model measured from TSM, in which the site amplification is neglected and the Q_{Lg0} measurements are biased. In these models, Q_{Lg0} within the Qaidam Basin is not as distinguishable from the Lg attenuation in the high TP.

In terms of our source terms, we observe a relatively linear relationship between estimated logarithmic RTM source terms and earthquake magnitude M_L (Figure 31) when $3 \leq M_L \leq 7$. This shows a possible application of RTM Lg amplitude in accurately detecting earthquake magnitude, because in theory it eliminates the contribution from geometrical spreading, site response, focusing/defocusing, scattering, and attenuation in propagation within inhomogeneous crust. We emphasize that its practical application is probably only limited by seismic station distribution.

Similar to Q_{Lg} as a proxy of crustal Q_S , the Q_{Pg} of another crustal regional phase Pg is assumed as a proxy of crustal Q_P . Although the propagation of Pg still contains uncertainties in theory (Kennett, 1989), many studies have suggested that it is reasonable and satisfactory to consider Pg phases as post-critical P waves trapped in a crustal wave guide (e.g. Hearn and Clayton, 1986; Steck et al., 2009). We apply a very similar data processing flow to the Pg data as we do with the Lg data; while some parameters, such as the group velocity window, the geometrical spreading coefficient, the threshold of maximum inter-station distance, etc, have been revised to appropriate values for Pg (Bao et al., 2011). The calculated RTM Q_{Pg} tomographic image is strongly correlated with the RTM Q_{Lg} model (Figure 28b): high attenuation regions throughout most of the northern TP and low attenuation regions surrounding TP. However, we observe differences in the relative attenuation structure between Pg and Lg in the Qilian Shan-Nan Shan ranges and central Qiangtang Terrane that probably indicate rheological anomalies in the crust.

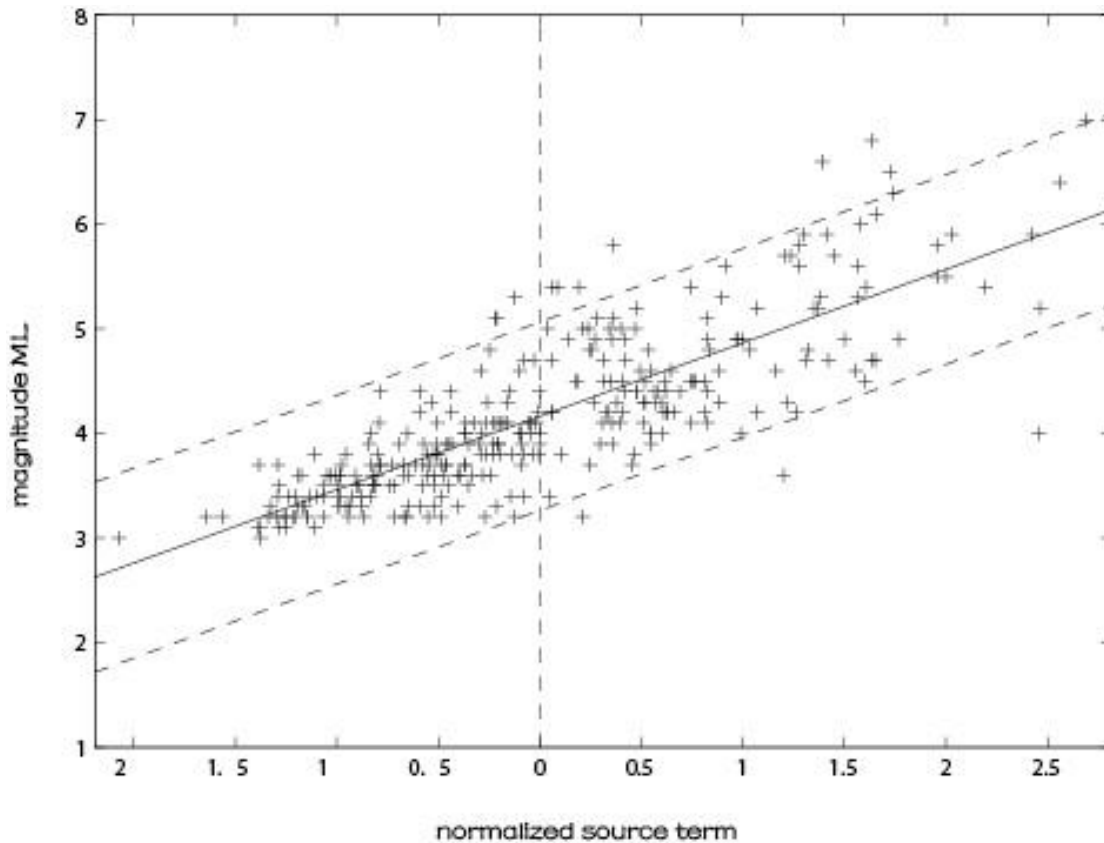


Figure 31. The linear relationship between normalized logarithmic source terms solved from Lg RTM and magnitude M_L . The solid line represents the least-square linear fit line and the two dashed lines parallel to it represent its 95% confidence interval. It indicates that the source term solved from Lg amplitude using RTM is well correlated with seismic magnitude M_L when $3 \leq M_L \leq 7$. This method eliminates the contribution of path, site, and source radiation pattern, and its practical application is only limited by seismic station alignment.

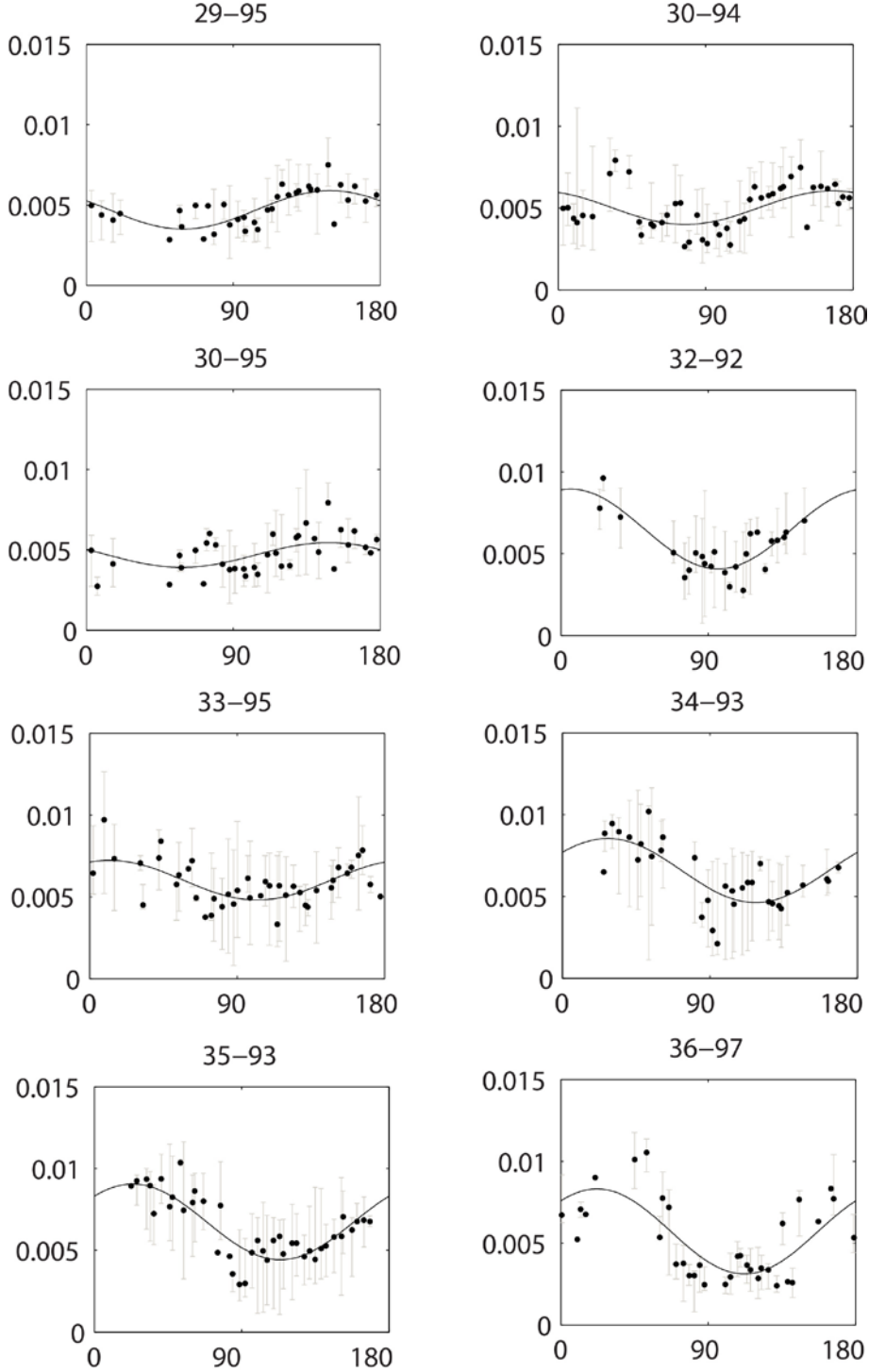


Figure 32 Examples of the RTM $1/Q_{Lg} \sim \phi$ correlation. The x -axis represents path azimuth ϕ and y -axis represents $1/Q_{Lg}$ value. The values of $1/Q_{Lg}$ are normalized using integration within an interval of 3.6° ($1/50$ of 180°). In each solvable interval, the normalized $1/Q_{Lg}$ is assumed as the median number (black dot), and error bar is also shown as gray. The black curves represent fitting curves using sinusoidal function of 2ϕ with a corresponding phase, whose period is 180° . The latitude and longitude of each block are specified in the title.

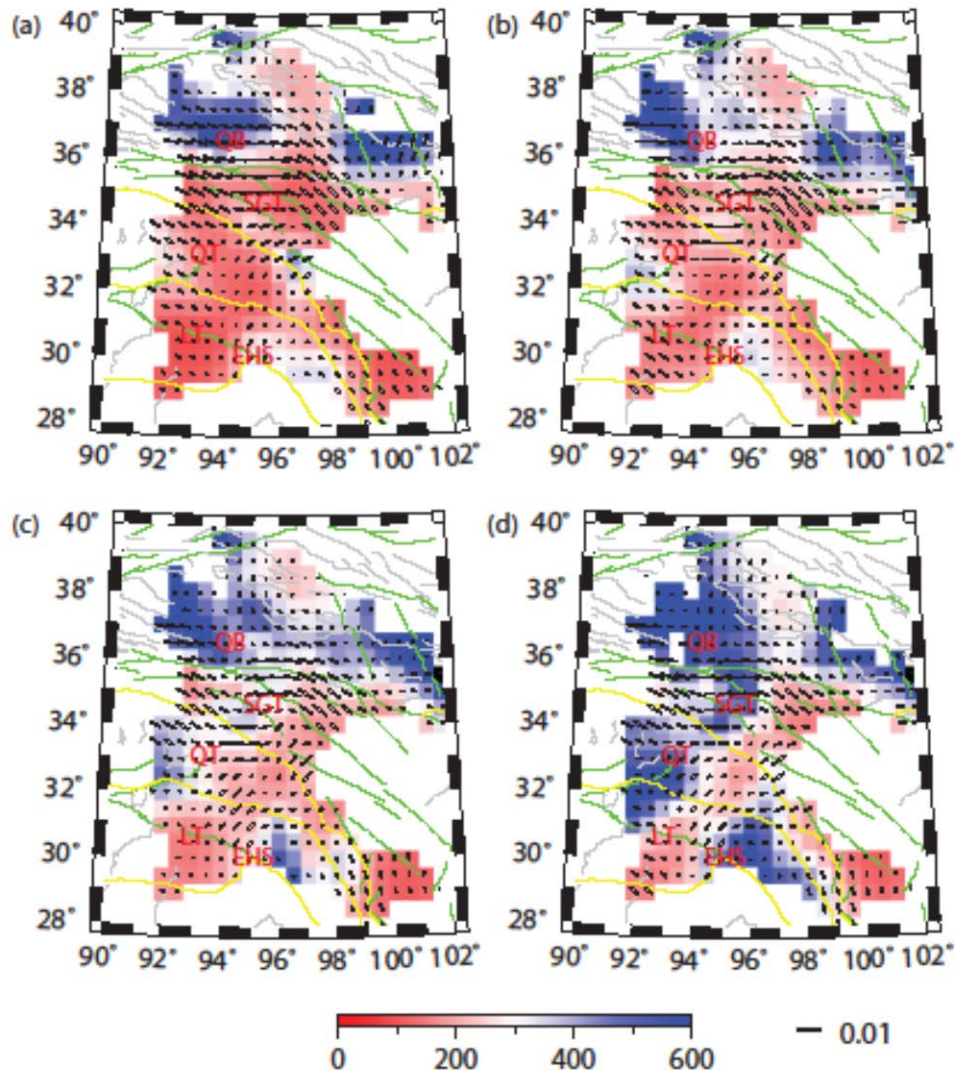


Figure 33. Imaged variations of isotropic Q ($1/A$), anisotropy magnitude (B), and high- Q direction (θ) in the crust of eastern Tibetan Plateau at different frequencies of (a) 0.6 Hz, (b) 0.8 Hz, (c) 1 Hz, and (d) 1.2 Hz. The color scale represents the variations of $1/A$, and the length and orientation of black vectors represent $1/B$ and θ , respectively. Major faults and sutures are also shown using the database HimaTibetMap-1.0 (Taylor and Yin, 2009), while strike-slip faults are green, other types of faults are gray, and sutures are yellow. QB: Qaidam basin; SGFB: Songpan-Ganzi fold belt; QT: Qiangtang terrane; LB: Lhasa block; EHS: Eastern Himalayan Syntaxis.

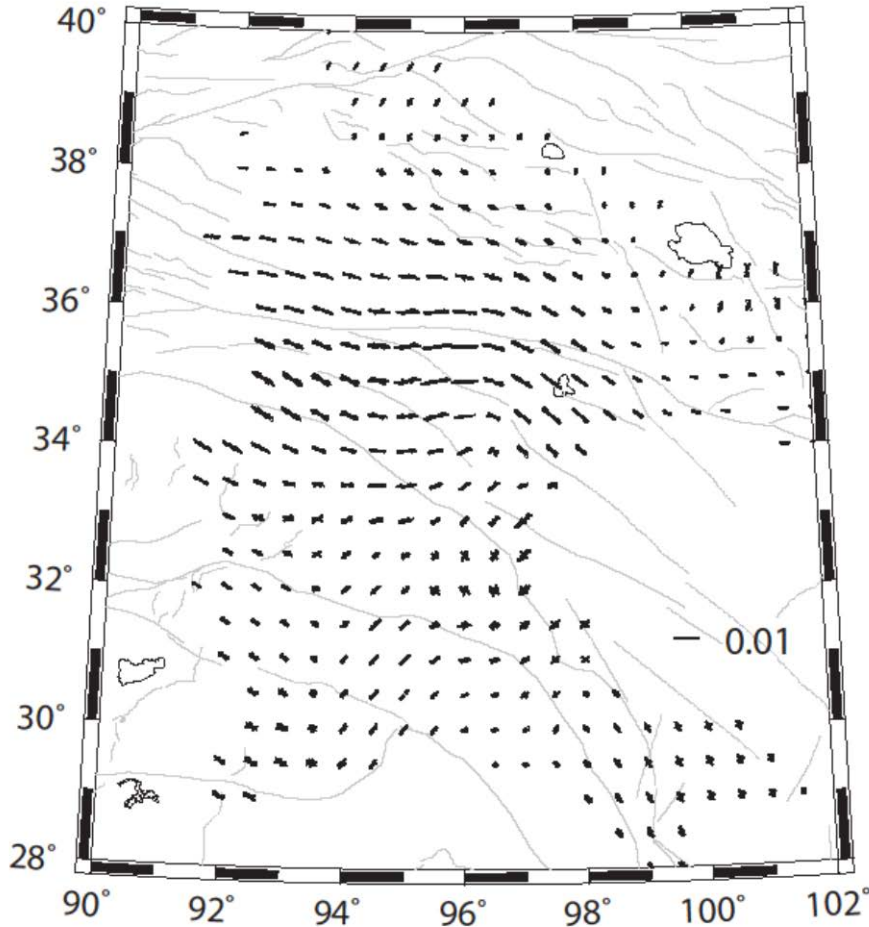


Figure 34. Comparison of azimuthal anisotropy of $1/Q_{Lg}$, for different frequencies, in the eastern Tibetan Plateau. The fast directions are overlain at each grid point, with vector length scaled by magnitude of the anisotropy, for 16 narrow frequency bands between 0.5 Hz and 2.0 Hz as described in the text. At most points all the vectors are essentially parallel, indicating very weak frequency dependency within most of this region.

Our images showing lateral variations in A , B , and θ at discrete frequencies from 0.5 to 2.0 Hz, in discrete steps of 0.1 Hz, are solved from the $1/Q_{Lg}$ azimuthal anisotropy tomography. Fig. 36 shows four examples of these tomographic images at different frequencies of 0.6 Hz, 0.8 Hz, 1 Hz, and 1.2 Hz. Only the cells with more than 5 hit-counts are included. To compare the results with tectonics, we employ the HimaTibetMap-1.0 database [Taylor and Yin, 2009] to show major faults and plate boundaries. Three aspects of the model, on the anisotropic part (containing two variables of B and θ) and isotropic part (A) of $1/Q_{Lg}$, are discussed and interpreted.

(i) The major pattern of anisotropic magnitude (B) is that there is a strong azimuthal anisotropy of $1/Q_{Lg}$ within the northern TP. The maximum B of the whole study region, typically higher than 0.01, is observed within the northwestern SGT, the Kunlun Shan (mountain range), and northern QT. Meanwhile, B is mostly less than 0.004 in the central QB, which shows a very significant discontinuity between the northern and southern side of the Kunlun Shan. B slowly decreases to below 0.005 in the central and southern TP, and appears to increase slightly around the EHS. In general we observe a very weak frequency-independent B (Fig. 8). (ii) A nearly uniformly W-E high- Q direction (θ) is observed in the northern TP. The highest B values are found in the northwestern SGT, with θ correlating strongly with the strike of the major transform fault planes, such as the North Kunlun Fault (NKF) and South Kunlun Fault (SKF). The central and southern TP are probably divided into three sections in terms of the distribution of θ . A clockwise rotation of θ is around the EHS, with a northwest-southeast (NW-SE) direction on the western side of EHS and a nearly N-S direction on the eastern side of EHS. We also observe that θ is largely frequency independent (Fig. 8). (iii) A strong frequency-dependent A in the eastern TP is solved by isolating the anisotropic part of $1/Q_{Lg}$, which leads to the major differences among Fig. 36 (a), (b), (c), and (d). At 0.6 Hz, the central QB has $1/A$ higher than 400 and the northwestern SGT, northern QT, and central LT have $1/A$ probably lower than 150. The $1/A$ values at 0.8 Hz are typically higher than those at 0.6 Hz with a shift of 50. For frequencies larger than 1 Hz, we find three relatively high $1/A$ zones (350 at 1 Hz and >400 at 1.2 Hz) in the southern QT, EHS, and the center of northwestern SGT.

There are likely two possible interpretations for the strong azimuthal dependence of $1/Q_{Lg}$ along the Kunlun Shan: the influence from non-uniform geometry of the crust, or from the crustal anisotropy. Surface topography [Wu and Wu, 2001] and Moho geometry, sediment thickness [e.g., Kennett, 1986], and inhomogeneous velocity structures of the crust can generate a complicated seismic wave field at high frequencies (> 0.5 Hz). Across the Kunlun Shan, steep topography (> 2 km), a thick sedimentary basin (> 5 km in the Qaidam), and rapid Moho depth changes (15-20 km) [e.g., Zhu and Helmberger, 1998; Karplus *et al.*, 2011] all could lead to substantial scattering of the Lg wave field. Previous studies have observed an energy loss of Lg when its path laterally crosses the Kunlun Shan [Zhao *et al.*, 2003], which is probably associated with large geometrical fluctuations along this mountain range. A relationship between ray path azimuth α and the energy loss of Lg has been suggested by focused and defocused synthetic ray paths [Bostock and Kennett, 1990]. But the role of the influence of geometry on seismic attenuation from a generalized focusing and defocusing is actually still undeterminable for Lg [Furumura and Kennett, 1997]. The size of attenuation anomalies in our tomographic model is approximately 200 km and the focusing and defocusing produced by substantial seismic velocity variations should probably create smaller scale Q anomalies [Sarker and Abers, 1998]. The site responses beneath all seismic stations solved by the RTM, not included in the attenuation term, has been suggested to represent the influences from topography or sediment thickness [Bao *et al.*, 2011]. Our model with high anisotropy in other parts of the TP does not clearly show any strong correlation with Moho geometry [e.g., Wittlinger *et al.*, 1996]. We suggest that generalized focusing and

defocusing does not provide a necessary and sufficient condition for the azimuthal anisotropy of $1/Q_{Lg}$.

The seismic attenuation measured for the upper crust has been also suggested to include the effect from faults and cracks associated with fluids [Mitchell, 1995]. Fault zones have been suggested to play an important role in attenuation of coda waves resulting from scattering [Jin *et al.*, 1994]. Although it is still unknown how Lg samples the crust at different depths, the Q_{Lg} value should be affected by a crustal-scale fault zone. An azimuthal anisotropy of $1/Q_{Lg}$ is expected to be observed if such a fault system contains well aligned fractures and interstitial fluids. There is no evidence of abundant fracture fluids beneath TP, where a very dry crust is probably widespread [Hacker *et al.*, 2000]; however, such an interpretation with fracture fluids is unnecessary. It has been presented that the azimuthal anisotropy of $1/Q_{Lg}$ can be described as transversely isotropic media (TIM) containing multiple layers or aligned fractures with horizontal symmetry axis [Zhu and Tsvanskin, 2006; Chichinina *et al.*, 2009], and therefore be caused by the layers and faults themselves, not the content of fluid within them. Its anisotropic magnitude is related to, but much stronger than, the magnitude of the velocity anisotropy [Liu *et al.*, 2005; Chichinina *et al.*, 2006; Chapman, 2009]. This type of attenuation from multiple layers and aligned fractures is actually a shape preferred orientation, and is one of the major mechanisms for the crustal anisotropy [Werner and Shapiro, 1998].

The NKF and SKF are the two eastward extended branches of the Kunlun Fault (KF) and both are major left-lateral strike-slip faults in the northeastern TP. After separating at approximately 94°E , the NKF nearly follows the E-W orientation of the KF while the SKF turns to southeast and nearly parallels the orientation of the Jinsha Suture (JS), the tectonic boundary of the QT and SGT. We observe an alignment of the High Q directions along both the southern and northern branches of the Kunlun fault zones: E-W along the northern branch and NW-SE along the southern branch. The tectonic evolution of the SGT crust has likely been very complicated since the Mesozoic after the closing of the Songpan Ocean, including major amounts of crustal shortening and thickening [Roger *et al.*, 2010]. The complicated distribution of fractures and faults within the folded crust of the SGT may play an important role in the generation of the observed anisotropic velocity and attenuation structures. Both the NKF and SKF likely extend into the heterogeneous upper crust probably with very low velocity and Q between them [Wang *et al.*, 2009; Karplus *et al.*, 2011]. If the crustal anisotropy is the major source of the azimuthal anisotropy of $1/Q_{Lg}$ estimated in our model, the upper crust of the northwestern corner of the SGT may be assumed nearly transversely isotropic with abundant parallel faults and fractures following the orientations of the NKF, SKF, and JS. Such a pattern is probably generated by high rates of deformation within the SGT that have been measured by observations of Quaternary fault slip rates and GPS observations [e.g., Holt *et al.*, 2000]. We consistently observe strong azimuthal anisotropy of $1/Q_{Lg}$ with consistently east-west directions in the northern portion of the QT. This orientation is consistent with the characteristics of upper crustal anisotropy within the SGT [Vergne *et al.*, 2003] and about 3° west of our model [Ozacar and Zandt, 2004], which suggests a common origin for both the velocity and attenuation.

The pattern of high- Q directions θ is dramatically similar with the fast wave direction in the upper to middle crustal models (about 20-30 km in our discussion) of azimuthal anisotropy of Rayleigh waves [Su *et al.*, 2008; Yi *et al.*, 2010; Yao *et al.*, 2010]. These models have different lateral resolutions ($5^\circ \times 5^\circ$ in Su *et al.*, 2008, $4^\circ \times 4^\circ$ in Yi *et al.*, 2010, and $2^\circ \times 2^\circ$ in Yao *et al.*, 2010) not higher than our model ($2^\circ \times 2^\circ$). They show corresponding magnitudes of velocity anisotropy of approximately 3%-5% and fast wave directions of nearly W-E in the western portion with a clockwise rotation in the eastern portion in our study area at an upper to middle crustal depth. A more complicated pattern of fast wave directions around the EHS, like the pattern of our high- Q directions, is observed from the model of Yao *et al.*, 2010 with the highest lateral resolution in the three models of Rayleigh waves. The similarity between the models of azimuthal anisotropy of $1/Q_{Lg}$ and shear wave velocity further suggests a probable pattern of crustal anisotropy and supports the assumed relationship between velocity anisotropy and attenuation anisotropy. If the estimated high- Q direction correlates with the orientation of crustal-scale fault systems, its lateral pattern, including W-E direction in the northern TP, the N-S direction to the north of the EHS, and the clockwise rotation around the EHS, it may represent the pattern of upper and likely middle crustal fabric caused by faults and fractures, which is probably related to shape-preferred orientation and different major deformation motions in the whole TP. The nearly W-E trend of high- Q direction θ in the northeastern TP is also close to the patterns of Global Position System velocity vector measurements [e.g. Wang *et al.*, 2001] and shear wave splitting fast directions [e.g., Huang *et al.*, 2000; Wang *et al.*, 2008; Li *et al.*, 2011]. This correlation supports the assumption of mechanical coupling between the crust and lithospheric mantle during their deformation in the northeastern TP. But the southern TP shows a complexity where the stability of such coupling is likely affected by the probably underthrusting Indian lithosphere. Meanwhile, since the propagation of Lg waves is also likely affected by the complicated lower crustal velocity structures within the southern TP [Nábělek *et al.*, 2009], a possible contribution from the lattice preferred orientation may lead to a more complicated situation in the representation of the azimuthal anisotropy of $1/Q_{Lg}$ for the estimated crustal anisotropy.

4.4 Sn Q Tomography (Tibet and Northeastern China)

We studied Sn propagation across the Tibetan Plateau and northeastern China in order to quantify upper mantle shear wave attenuation. Efficient and inefficient longer period Sn waves were identified using data from the INDEPTH-IV array. More than 12,000 waveforms were reviewed and the Sn propagation efficiencies determined from instruments used in the ASCENT and NETS arrays in the northeastern Tibetan plateau and a further 6,000 waveforms were reviewed for our study in northeastern China. We were able to identify more than 2000 efficient paths from data that were bandpass filtered through 0.2 and 0.05 Hz for long period Sn waveforms. We used both the two and reverse two station method to calculate Sn Q that eliminates any source contribution to the Sn waveform. All waveforms were also corrected for instrument response. This method allowed us to tomographically determine variations in Sn Q across the Tibetan plateau.

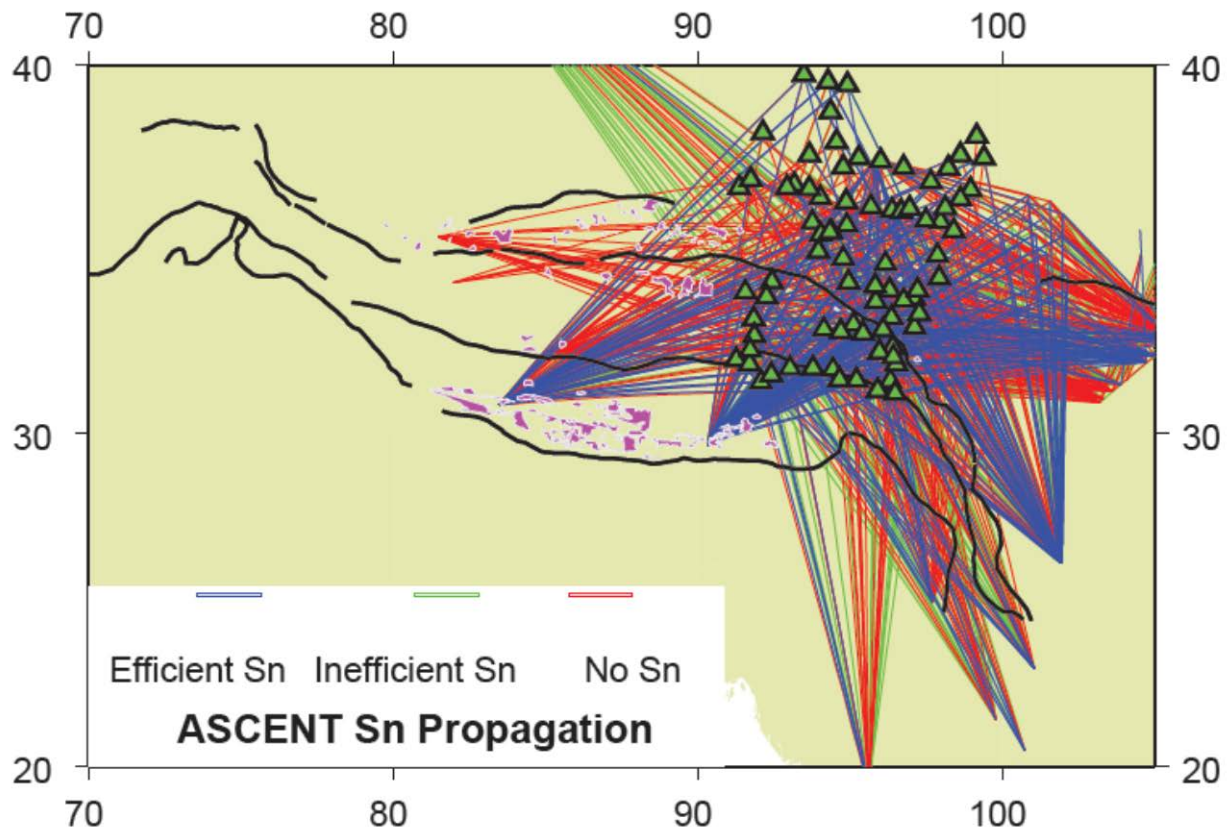


Figure 35. Sn efficiency map for Tibet with all efficient paths shown on top of the blocked and inefficient paths.

Our results suggest that Sn Q is low in and around the active fault systems like the Kunlun Fault. This observation is also consistent with shear-wave velocity models for the uppermost mantle. This observation points to a thin and hot lithosphere in northeastern Tibet up to the Qaidam basin. Both tomographic RTM and TSM models show portions of high Q (low attenuation) zones in central Tibet which are interpreted to be the leading edge of the underthrusting Indian lithosphere. Within the Qaidam basin we observe two regions of very high Sn Q that suggest that we are either smearing the effects from the Qilian Shan hot uppermost mantle or there are two distinct domains of the Qaidam mantle.

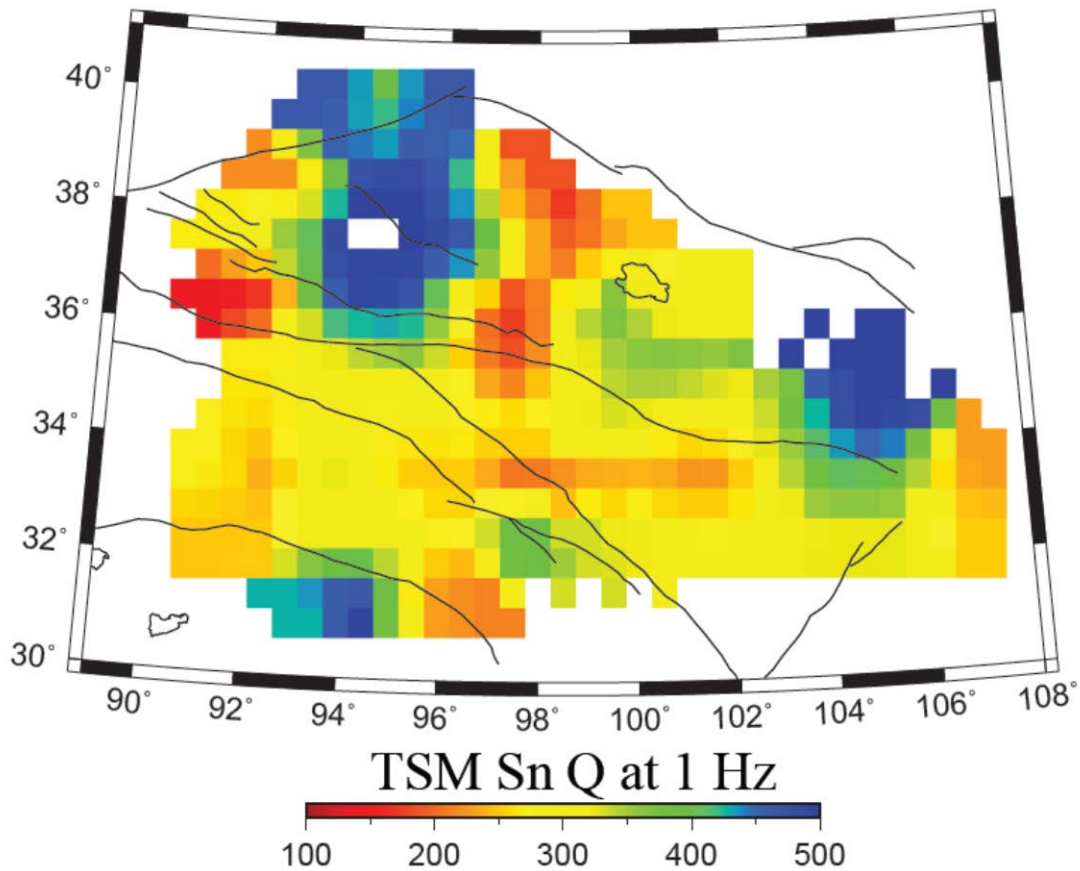


Figure 36. Sn Q tomography of northeastern Tibet at 1 Hz. *We once again observe the uppermost mantle beneath the Songpan Ganzi to be highly attenuation which is largely consistent with P-wave and S-wave velocity estimates of the same region.*

Comparisons of the RTM and TSM (Figures 36 and 37) models for Sn Q across eastern Tibet show significant differences. This observation would suggest that the crustal legs of Sn are having a significant impact on measured Sn amplitudes.

In addition to working on long period Sn Q studies in Tibet, we extended our work to include northern China with the eventual goal in future work of creating an Sn Q map for all of China and some of the surrounding regions. All of the seismograms in our study have been manually reviewed by applying two bandpass filters with corner frequencies of 0.5 to 2 Hz and 0.1 to 0.5 Hz to identify Sn. We classified each seismogram into one of three categories: no Sn (blocked), inefficient Sn and efficient Sn. If the Sn wavetrain can be seen for both high and frequencies seismograms, we categorize it as efficient. If no distinguishable high-frequency Sn wavetrain is observed but Sn could be observed in the low frequency band, or an ambiguous signal was found, we classified it as inefficient. Otherwise, we assigned the seismogram as “no or blocked Sn”. Figure 38 shows all Sn ray paths with color coded efficiencies used in our study. It shows that the inefficient Sn

ray paths are primarily restricted to those paths that cross the Sea of Japan, and the efficient Sn ray paths are mostly found for continental paths in our study region.

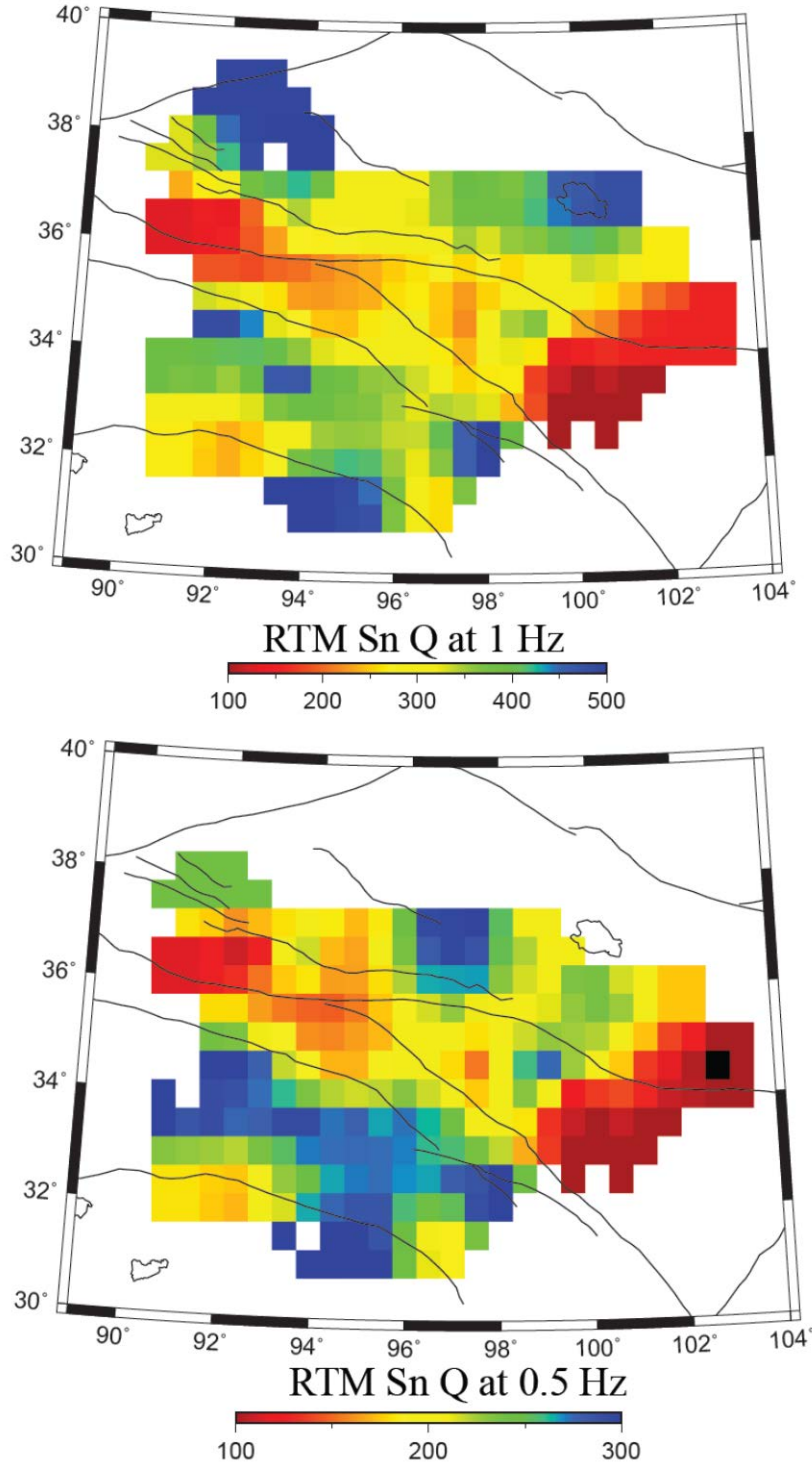


Figure 37. Top: RTM Sn Q tomography of northeastern Tibet at 1 Hz; Bottom: RTM Sn Q tomography of northeastern Tibet at 0.5 Hz. Note the differences between the Sn TSM and RTM methods, which suggest that the station and event site amplification have a significant impact on Sn amplitudes.

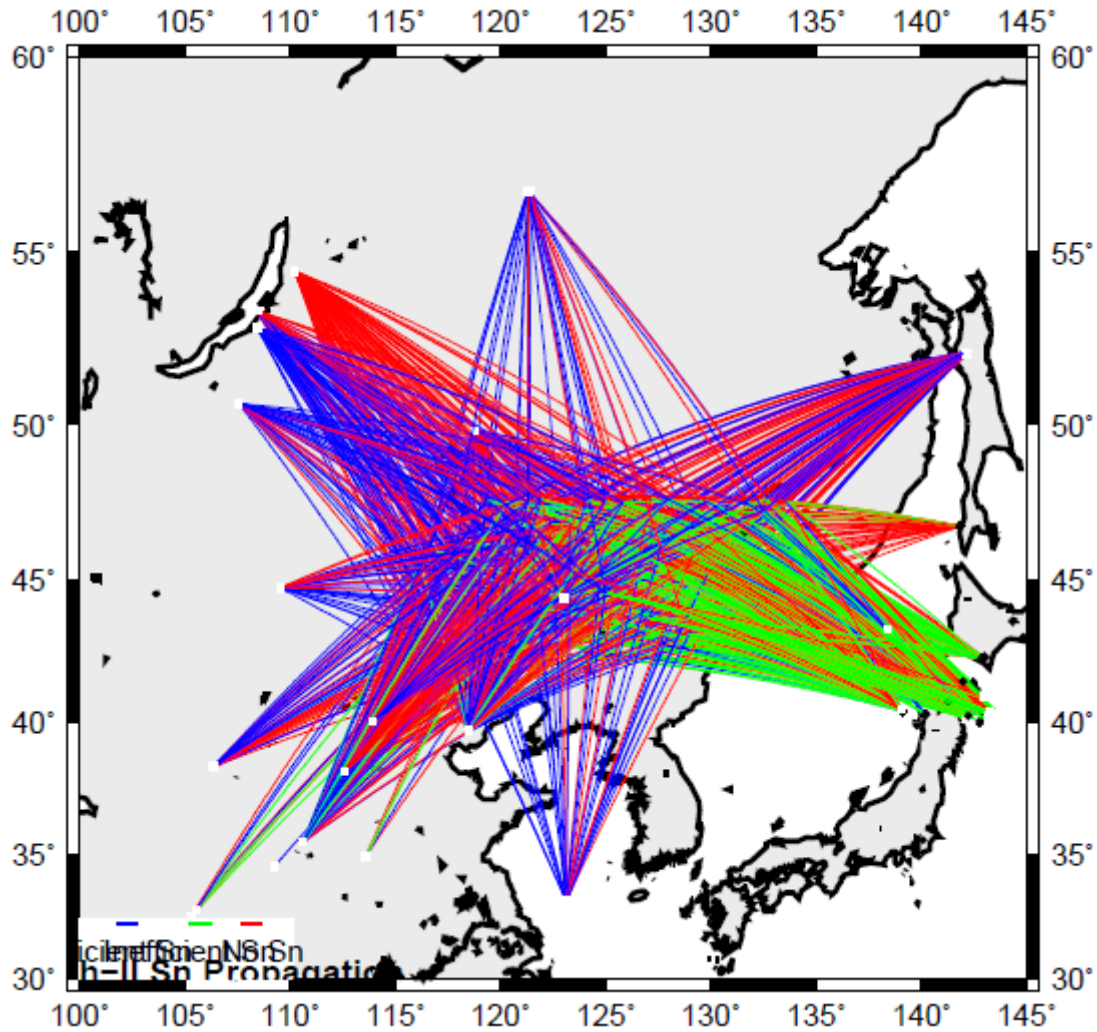


Figure 38: A map showing the Sn raypaths across northeastern China using broadband data from the NECESS array. *The propagation efficiencies are labeled by color: Blue, green and red lines present efficient, inefficient and “no or blocked Sn” raypaths, respectively.*

We inspected individual seismograms to remove the data that are too noisy or have incorrect timing. The Pn arrival time was automatically calculated and we also manually re-picked Pn for a more accurate arrival time. It was used to obtain a pre-Pn window and calculate the ambient noise level. Only those estimated Sn spectra with signal-to-noise ratio larger than 2 were kept. Furthermore, we cut a pre-Sn window between 4.8 and 5.0 km/s and an extensional Sn window between 4.1 and 4.8 km/s. If the root mean square of the extensional Sn signal to that of the pre-Sn was less than 1.05, the data were removed.

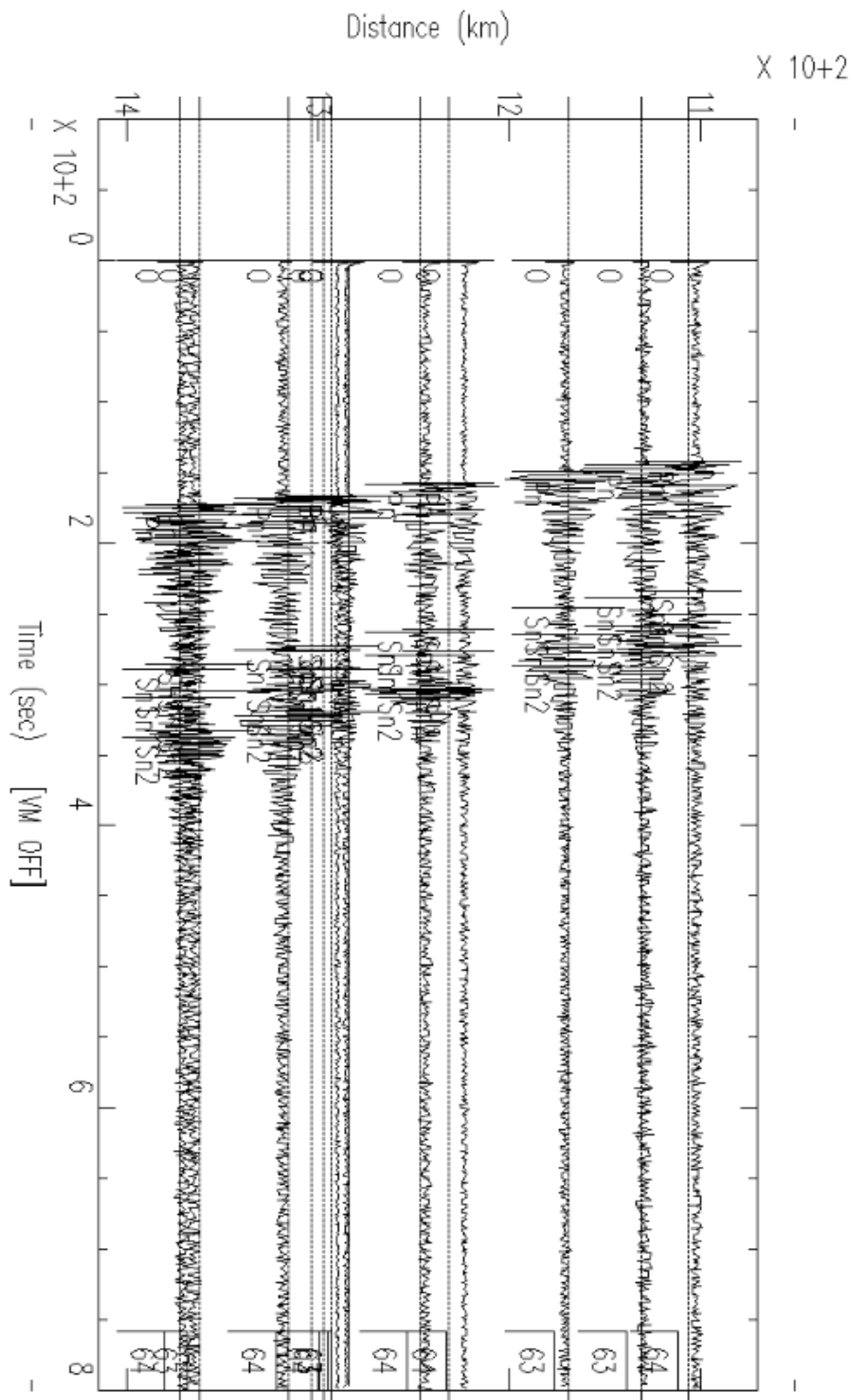


Figure 39. Sample record section for an earthquake occurring along the Pacific subduction zone.

The Sn velocity window was defined for 4.3 to 4.7 km/s uppermost mantle velocities. The Sn window was automatically estimated to start with a fast velocity of 4.8 km/s and end with a slow velocity of 4.1 km/s. To better isolate the Sn spectra, we adjusted the Sn windows manually. A window with a Pg velocity of 5.1 km/s and Lg group velocity of 3.5 km/s was used to avoid mistaking Pg coda or early Lg for Sn. Figure 7 shows some of the efficient Sn seismograms for one event. We can see that the Sn arrival time is around the center of the Sn window, which indicates the Sn velocity is approximately 4.45 km/s. In our study, we set an Sn velocity of 4.4 km/s based on the velocity model provided by Zheng et al. (2011).

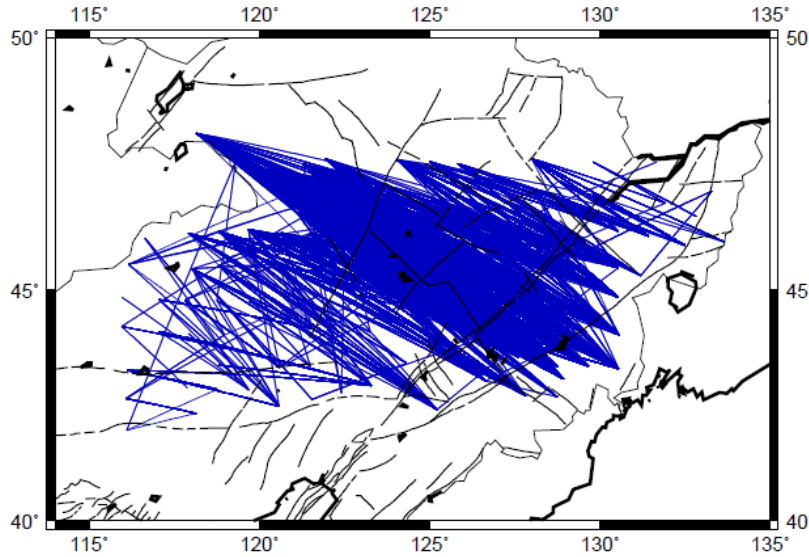


Figure 40. A map of the reverse two-station SN raypaths for the NECESS array.

The calculated Q_0 values were used to map the lateral variation of Q_0 by applying the LSQR algorithm (Figure 42). We can roughly divide the Q_0 values into four regions: low ($Q_0 < 400$), medium low ($400 < Q_0 < 800$), medium high ($800 < Q_0 < 1200$), and high ($Q_0 > 1400$). We observed low Q_0 in the Xilinhote block, the Songnen block, the eastern Zhangguangcailing block, and the Yanji block which are part of the Songnen unit, medium low Q_0 in the Erguna-Xing'an block, medium high Q_0 in the central and northern Songliao basin, and high Q_0 in the southern Songliao basin, Jiamusi block and part of Harlar-Tamsag basin and Erlian basin. In general we observe that the basins are characterized by high Sn Q_0 values. The borders between high Q_0 and low Q_0 are mostly along the active faults.

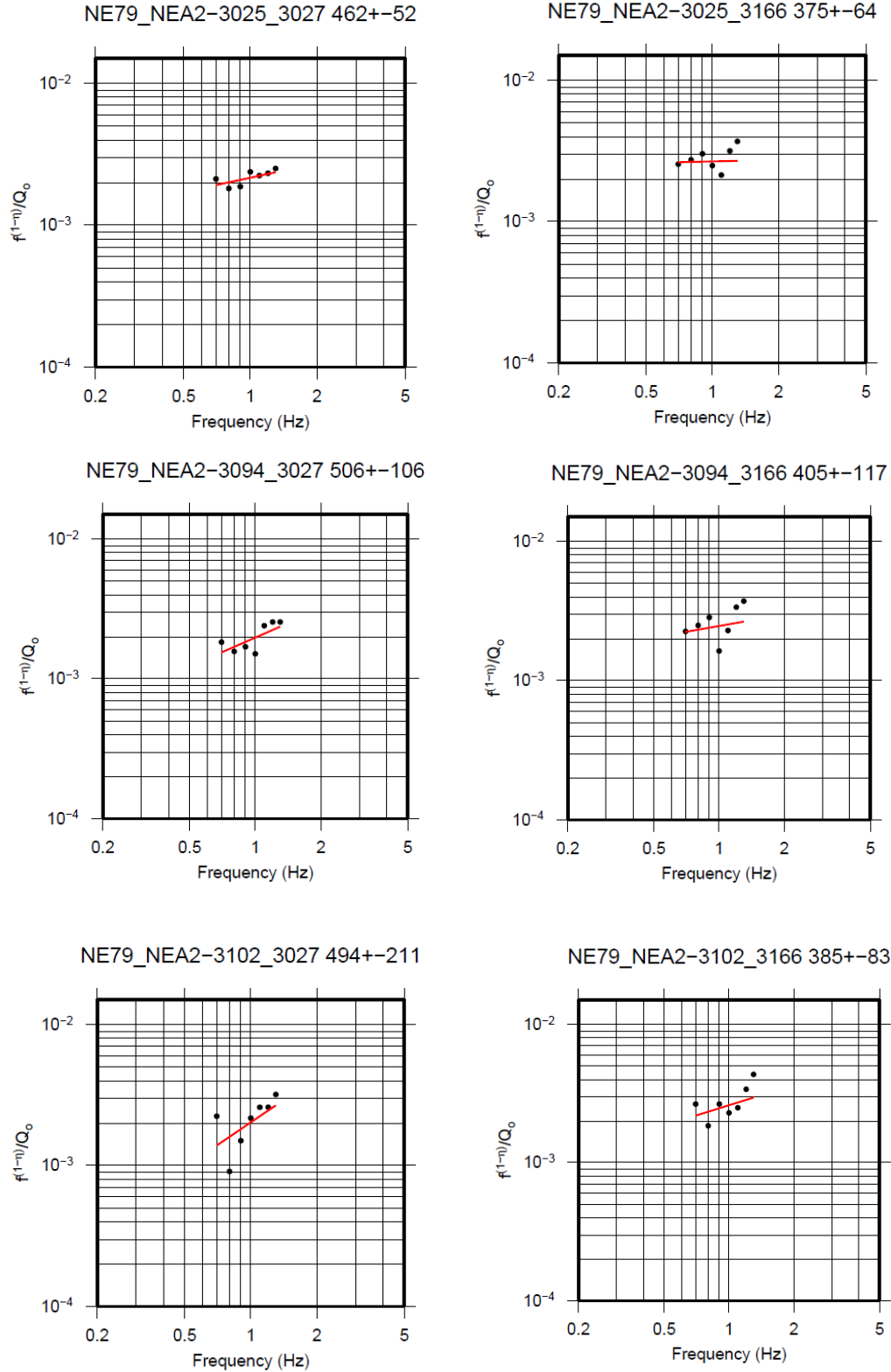


Figure 41 An example of linear regression fitting for interstation RTM Q_0 values for the same station pair NE79-NEA2. The title of each plot indicates the station pair, event pair, Q_0 values and errors. Note the large differences in the slopes indicating the relatively poor control we have on the frequency dependence for this particular two station pair. We can, however, use these types of repeated paths to estimate confidence limits on our Q models.

Approved for public release; distribution is unlimited.

We measured the RTM Sn Q values at discrete frequencies of 0.5 Hz, 1 Hz and 2 Hz. The data procedure is revised from Xie (2002a) and Xie et al. (2004).). Furthermore we did not obtain any effective RTEM paths due to the distribution of the stations and events. We set the minimum inter-station distance of 150 km in order to minimize Q estimation errors. Also, we set the maximum azimuthal angle at 15° to minimize modeling errors and the effects of multi-pathing. We set the minimum and maximum allowable interstation Sn Q values to 10 and 3000 respectively. Only Q values with error less than 50% and that met the interstation Q_0 quality control criteria were accepted. In the end we obtained 8003 reverse two-station paths (Figure 40) and Q_0 values. The Q_0 and η values and deviations were calculated from a linear regression. Examples of interstation spectral ratios and the Q_0 values are shown in figure 41. We found that the Q_0 values range from 277 to 576.

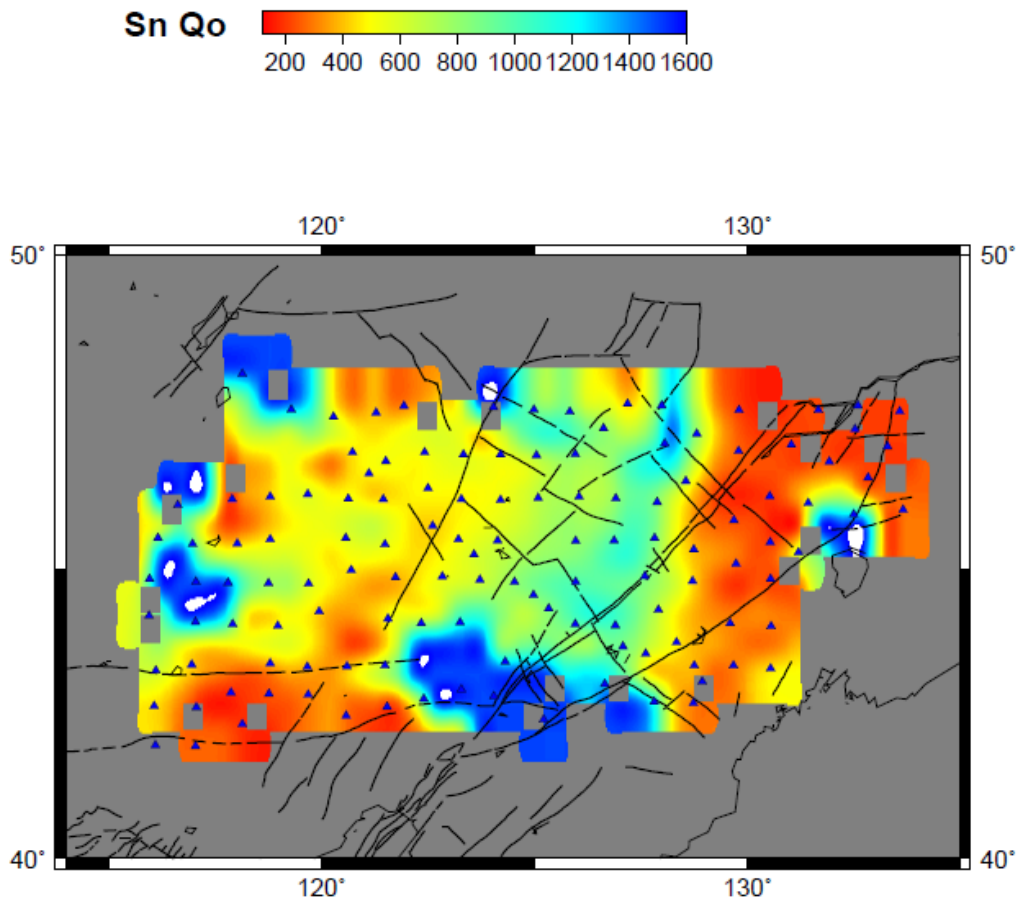


Figure 42. RTM Sn Q map at 1 Hz with a cell size of $0.5^\circ \times 0.5^\circ$. Blue triangles are stations.

The lateral variation of Sn Q_0 was helpful to infer the origin of seismic anomalies in the upper mantle. By correlating our Sn Q model with velocity measurements, we could determine which originated from temperature and which originated from compositional variations in the uppermost mantle. Liu et al. (2001) illustrated that the pattern of

magmatism since 4.5 Ma would suggest that the mantle upwelling strongly affected attenuation of Sn in regions within the Songliao basin.

We also measured TSM Q in this region in order to compare it to our RTM Q model. Any differences would likely originate from the site terms listed in equation (19). When preparing the two-station paths, we kept those paths with the more distant station having an Sn efficiency of “no Sn” and obtained 1685 two-station paths (Figure 40). We calculated TSM Sn Q_0 for 0.5~1.5 Hz (Figure 41). Compared with our RTM model, generally, it shows higher Q_0 values in high Q regions and lower Q_0 values in low Q regions. This may be due to the site effect that was not eliminated in the TSM Sn Q_0 . Typically, high site responses occur in basins, which may lead to higher TSM Q_0 values in the basin.

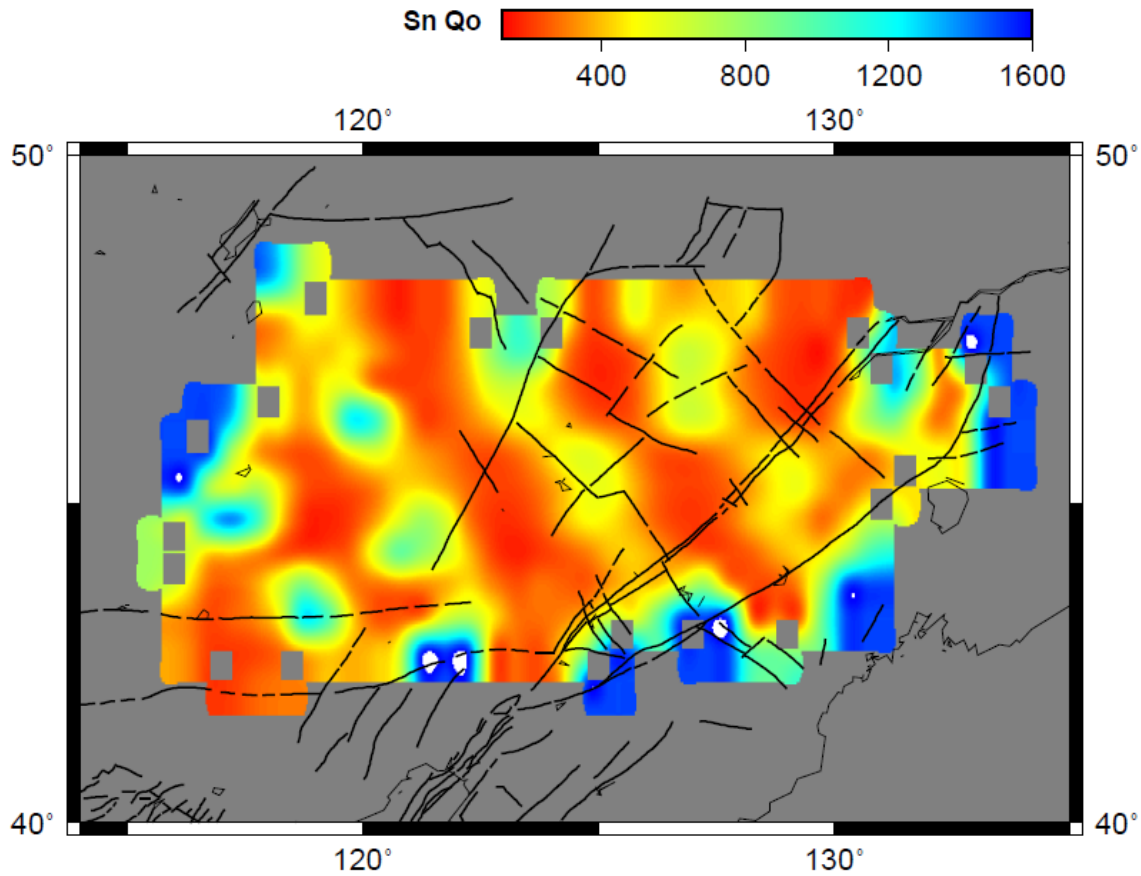


Figure 43. Checkerboard test with a $2^\circ \times 2^\circ$ cells using 3000 reverse two-station paths.

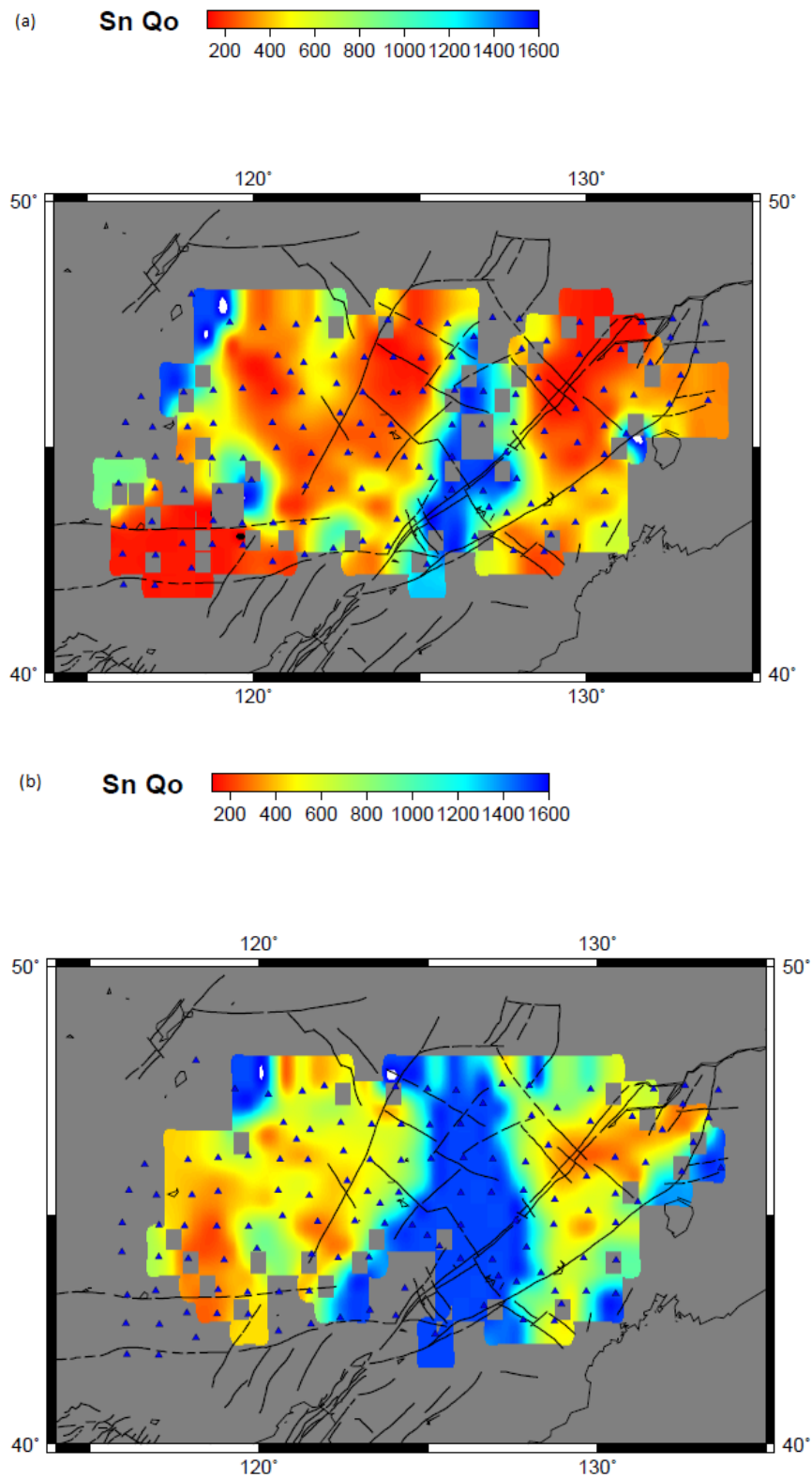


Figure 44. $Sn Q$ at (a) 0.5 Hz and (b) 2.0 Hz with $0.5^\circ \times 0.5^\circ$ cells. *Blue triangles denote stations.*

A 2D checkerboard test with 10% Gaussian distributed noise shows relatively good resolution for a $2^\circ \times 2^\circ$ anomaly size in most of the study area (Figure 43). In general we do observe some east west smearing because of the predominance of east-west reverse two station paths. Despite this, we are still able to resolve Q anomalies at a 2 degree cell size.

We have broadened the frequency band to 0.1~2.0 Hz for measuring η . We found low η values in the center of our study area where we suggest that anelastic attenuation dominates, whereas high η values around the edge suggest scattering attenuation or more likely worse resolution for the frequency dependence. At the edges of our model we have fewer crossing paths and which leads to larger errors and possibly larger values of η . Stronger frequency dependence would be more consistent with scattering attenuation rather than intrinsic attenuation. In general we observe only a weak frequency dependence which surprisingly suggests that intrinsic attenuation dominates throughout northeastern China.

The frequency dependence of $\text{Sn } Q$ appears to be quite complicated. In general we do observe a strong correlation between the frequency dependence and the Q value itself, which is commonly observed for high frequency regional phase Q . This observation suggests that at least part of the frequency dependence is a systematic problem with measuring larger Q values. We can see this effect in the Songliao Basin where we see the same spatial patterns in η as we do in Q

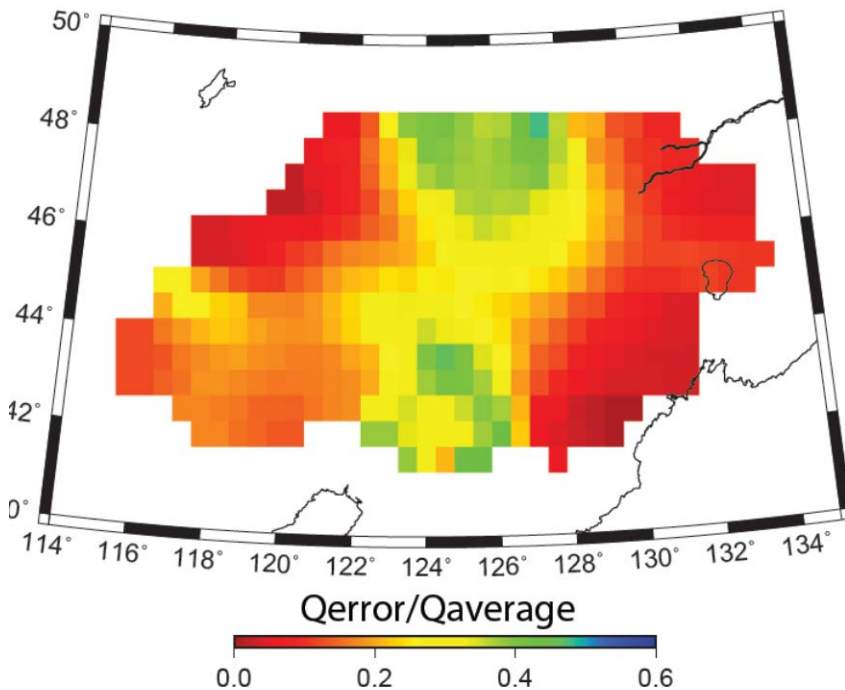


Figure 45. Our percentage error of $\text{Sn } Q$ at 1 Hz across our study region. *It is necessary to show the Q error as a percentage because larger Q values are significantly less well constrained than lower Q values.*

We have found a very large number of reverse two station paths (i.e. more than 3000), however, many of these paths are repeated paths. In fact we have approximately 800 unique reverse two station paths for the NECESS array (mostly east-west). This means we have a large number of repeat paths for each of our reverse-two station pairs. An example of these repeated paths is shown in Figure 41 for station pair NE79-NEA2. We can use these types of repeated paths to estimate confidence limits of our regional phase Q models by measuring the standard deviations of these repeated paths. We have compiled standard deviations for all two station pairs with at least 10 measurements and then computed a standard deviation for each pair. We then tomographically mapped the spatial variation in errors to produce error maps. Figures 45 and 46 show our model error estimates for the Q at 1 Hz (Q_0) and the frequency dependence (η) respectively. The errors for the frequency dependence show particularly large values in regions with high Q which again suggests that we have a difficult time constraining the frequency dependence for large Q values, as was seen in figure 41. In regions with lower Q values, on either side of the Songliao Basin, we do appear to be able to constrain the frequency dependence reasonably well.

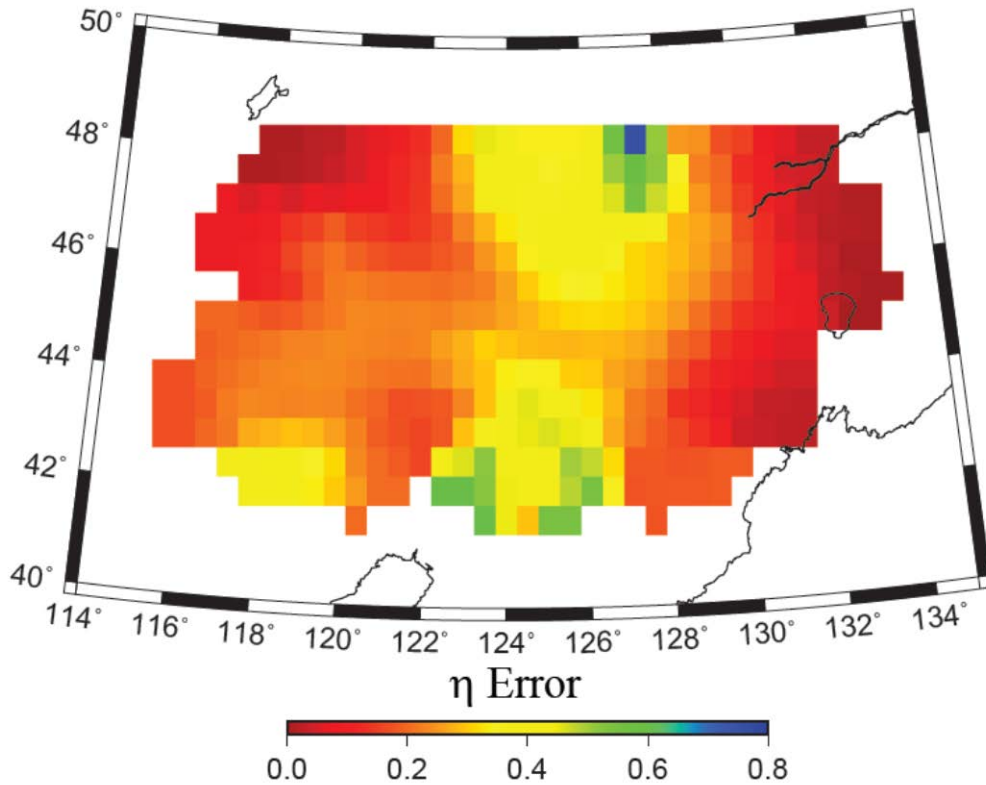


Figure 46. The error for the Q frequency dependence term η across our study region. *Note the very large error along the Songliao Basin which suggests that we have little to no control on Q 's frequency dependence at Q values larger than 1000 for S_n amplitudes.*

4.5 ML Amplitude Tomography

The inversion contained station gains, event gain corrections, geometric spreading, and regionally varying Q . While both the amplitude and measured period were included in the inversion, the period data often were reported with only one significant digit of precision. Since ML periods are small (0.1 to 2 seconds) and in the denominator, this means that errors in the period could cause large errors in the predicted amplitude. We attempted to use it in the inversion but results were unreliable. As a result, we fixed the periods to 0.5 seconds in the inversion. Nevertheless, it is important to note that assumptions about frequency dependence greatly affect both the geometric spreading and attenuation values.

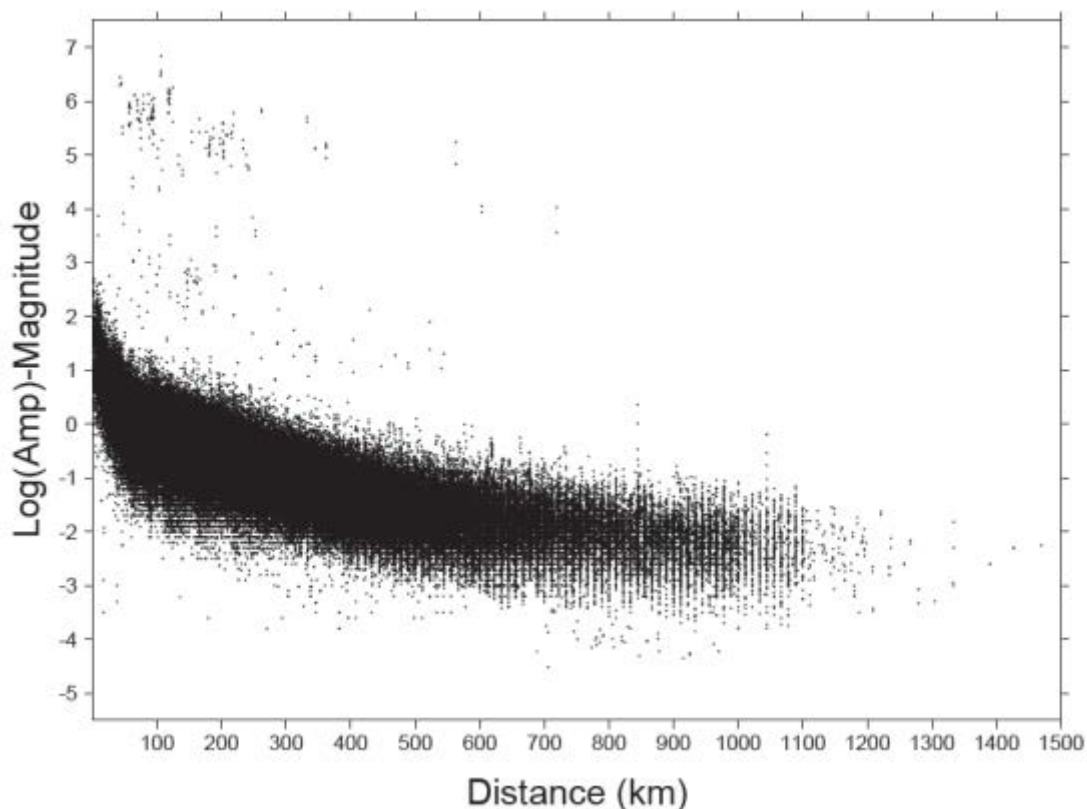


Figure 47. Log amplitude versus offset for the raw data set before selection. *Amplitudes were first converted to units of nanometers and then normalized for event size by subtracting the magnitude. Our fit to these data found a spreading coefficient of 0.75 and an average Q of 490. This absolute Q value could be biased by the assumed velocity and period; however, the pattern of attenuation found in the tomography is stable.*

The inversion restricted data to events with depths less than 33 km and source-receiver distances between 0.5 and 9 degrees. Data had an average period of 0.5 seconds so we restricted the data to those between 0.1 and 1.0 seconds. In addition, we iteratively eliminated stations with less than 10 arrivals and events with less than 25 recording

stations and also iteratively eliminated arrivals with residuals greater than one order of magnitude. We have assumed an average wave speed of 3 km/s and the average period of 0.5 seconds.

The results gave a geometrical spreading factor of 0.8 and an average Q value of 484 (Figure 47). The estimated Q value depends inversely on the assumed wave velocity and period. We attempted to use the measured period in the inversion, but the results were unreasonable with high spreading and Q values. This occurs because the period data often were reported with only one significant digit of precision and are subject to errors. Furthermore, since ML periods are small (0.1 to 21 seconds) and in the denominator, small errors in the period can result in large errors in the estimated amplitudes. Attempts at including a frequency dependent Q were also made; however these resulted in the untenable frequency dependences. Again, we believe this is because of the poor precision and accuracy of the period measurement. We did find, however, that including frequency dependent Q could significantly alter the spreading and attenuation estimates.

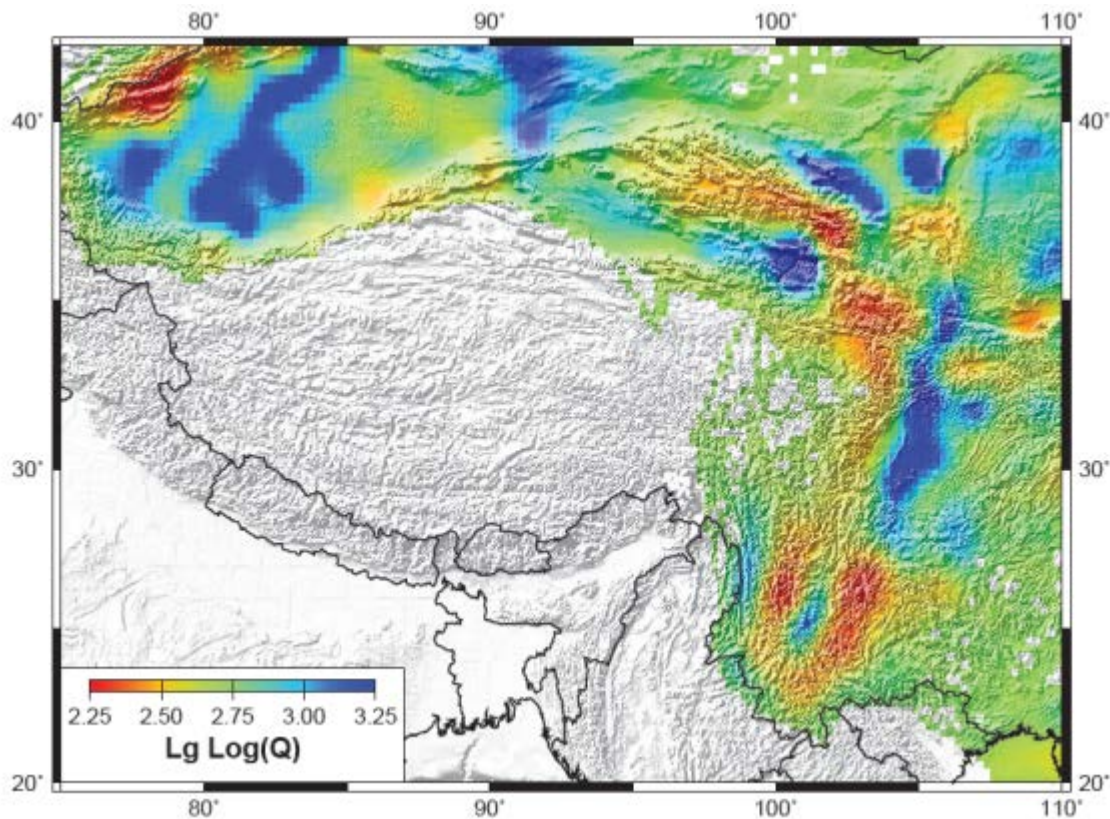


Figure 48. Tomographic image of Q across Tibet using amplitudes from the Chinese Earthquake Bulletin.

A comparison with our work using Lg and Pg data is somewhat limited because of the somewhat limited overlap between the two models, however, we do observe consistency across the Qaidam basin (high Q) and Qilian Shan mountain belt (low Q). Furthermore, we have found similar patterns to the relative station terms between the ML tomography and RTM approaches. We consistently observe a de-amplification of crustal phases in

the Tibetan plateau while we observe amplification in the Qaidam basin and surrounding regions (Figure 49). The absolute amplitude of the Q anomalies are somewhat different however. The MI amplitude tomography (shown in Figure 48) had larger Q values ($Q \sim 1000$) than we found using the RTM and TSM approaches ($Q \sim 500$).

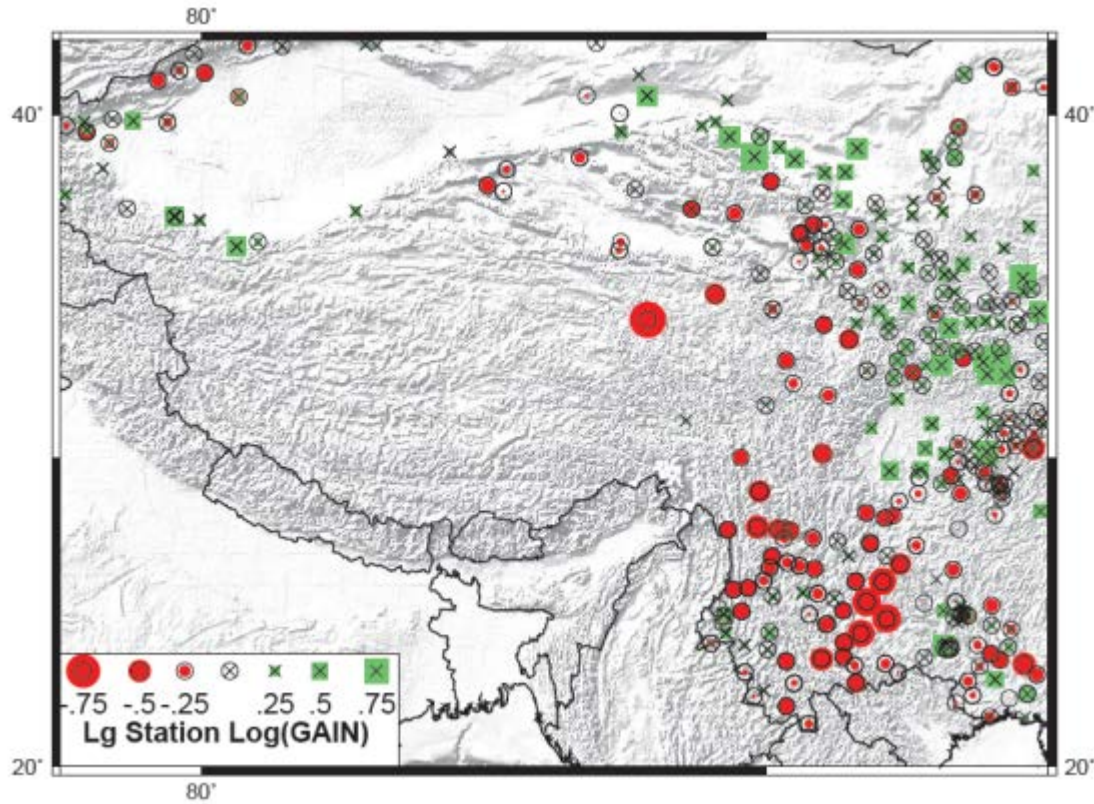


Figure 49. Relative station terms for the tomography. *Station terms are the logarithm of the station gains and are expressed in magnitude units.*

4.6 Joint Inversion of Receiver Functions and Surface Wave Dispersion Curves

We conducted a feasibility study of using our 3-D shear wave velocity model for Tibet by doing a joint inversion of dispersion curve data using both phase and group velocity data combined with published receiver functions across the ASCENT seismic network. We compared different velocity models using independent techniques to see which portions of the models are common to all of our models. We used the receiver function work of Han et al. (2012) and surface wave phase velocities of Ceylan et al. (2013) combined with the global group velocities from Pasyanos (2010) by applying the joint inversion method of Julia, et al. (2000). We used Rayleigh wave phase velocities obtained from the two plane wave method and receiver functions calculated using the method of Liggoria and Ammon, 1999. We took advantage of the constraints provided by PS move-out in receiver functions by creating a large number of receiver function stacks over a relatively narrow distance range (~ 5 degrees) and then simultaneously modeled all of the stacks. By utilizing the PS move-out this way we could better constrain the V_p/V_s ratio for the crust. We were generally able to fit both data reasonably well with the exception of some of the PS converted phase amplitudes. An example of the data fits is shown in Figure 50

for a station located directly on the Kunlun fault zone just south of Golmud China. This result is typical of what we have found for these stations in this region.

We have obtained 72 one dimensional velocity models for all of the ASCENT array stations; interpolating between these 72 models we were able to construct a three dimensional velocity model. Furthermore, we estimated a crustal thickness value for all 72 stations by choosing the center of the large positive velocity gradient at the base of the crust. We found that by choosing the center of the velocity gradient we obtained results roughly consistent with Han et al., 2012. If we chose the base or beginning we obtained generally unrealistic crustal thickness values. Figure 51 is our optimal Moho map using the center depth of the 1-D velocity gradients; this model shows crustal thickness patterns consistent in a relative sense with the migrated receiver functions: a thinning of the crust toward the Qaidam basin and the thickest crust south of the Jinsha suture. We also found further evidence of an upper crustal low velocity zone and a crustal thickness of approximately 70 km within the Kunlun Fault zone. We observed a reasonable agreement between mantle P-to-S converted waves and the LVZ imaged by the surface wave data.

Station C001

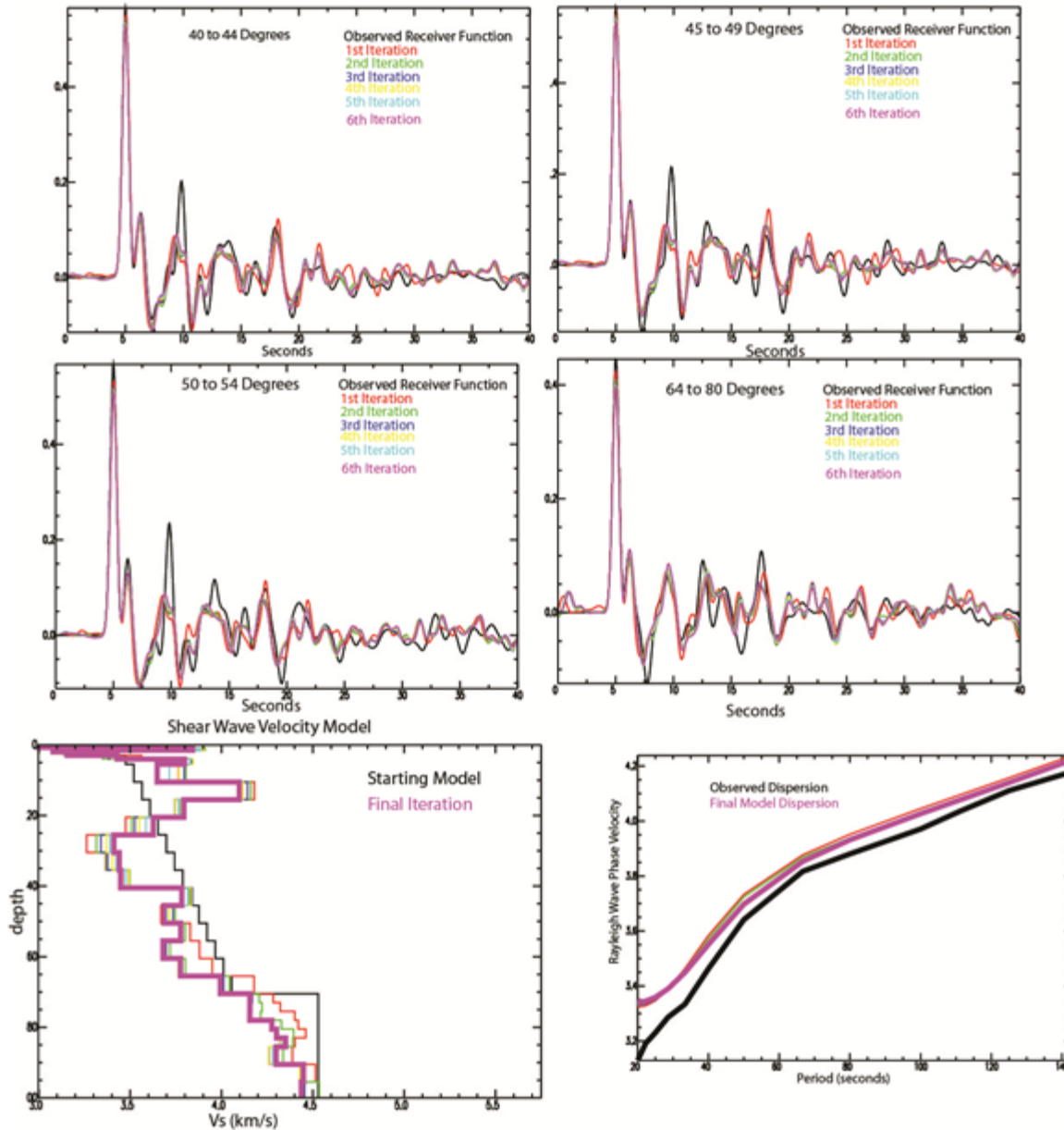


Figure 50. The results of one of our Joint Inversions for station C001. *This station was located near the northern edge of the Tibetan plateau with the Qiadam basin located just to the north. We found evidence of a low velocity layer in the uppermost mantle that is consistent with the surface tomography of Ceylan et al., 2012 and our Pn tomographic models using shorter ray paths.*

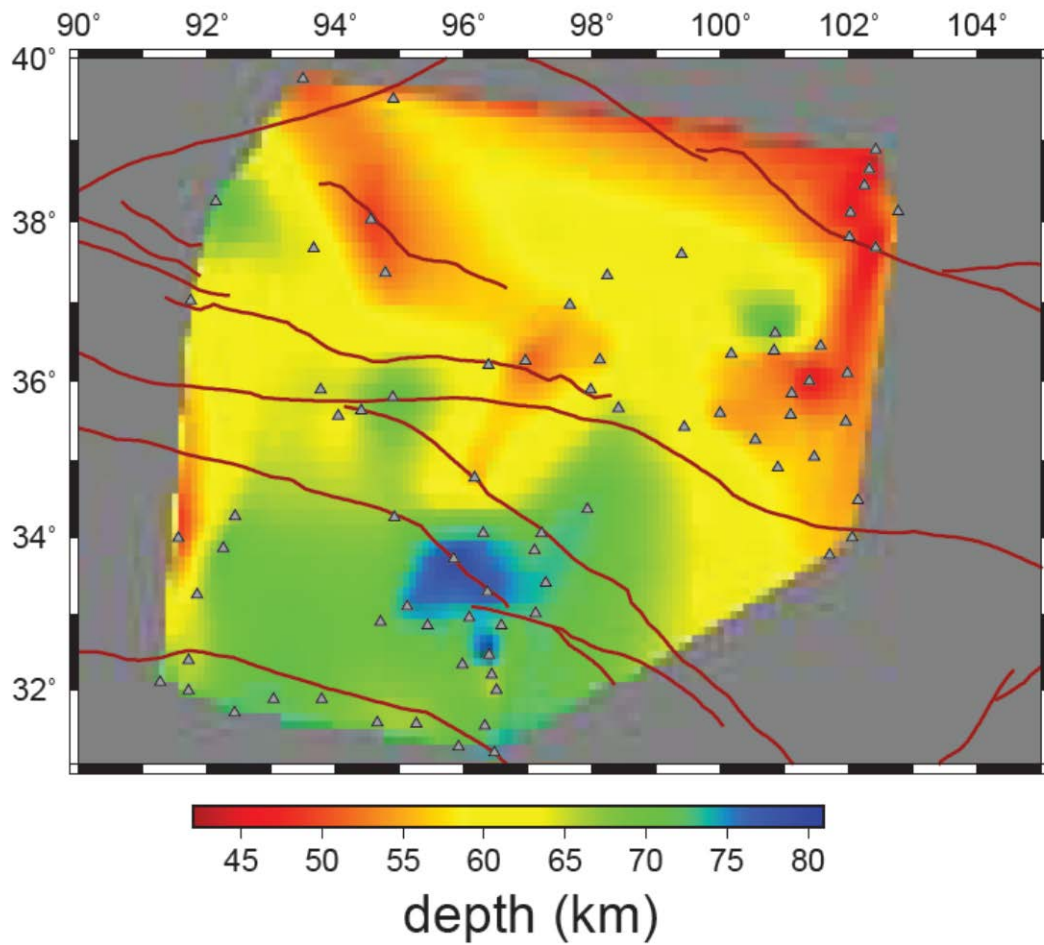


Figure 51. Our Moho map generated from the optimal 1-D velocity models from 70 stations across northeastern Tibet. *The triangles show the location of all stations were obtained optima 1-D models for. This map was constructed by taking the middle of the steepest velocity gradient from the lower crust to the uppermost mantle.*

5. CONCLUSIONS

5.1 Seismic Velocity Studies

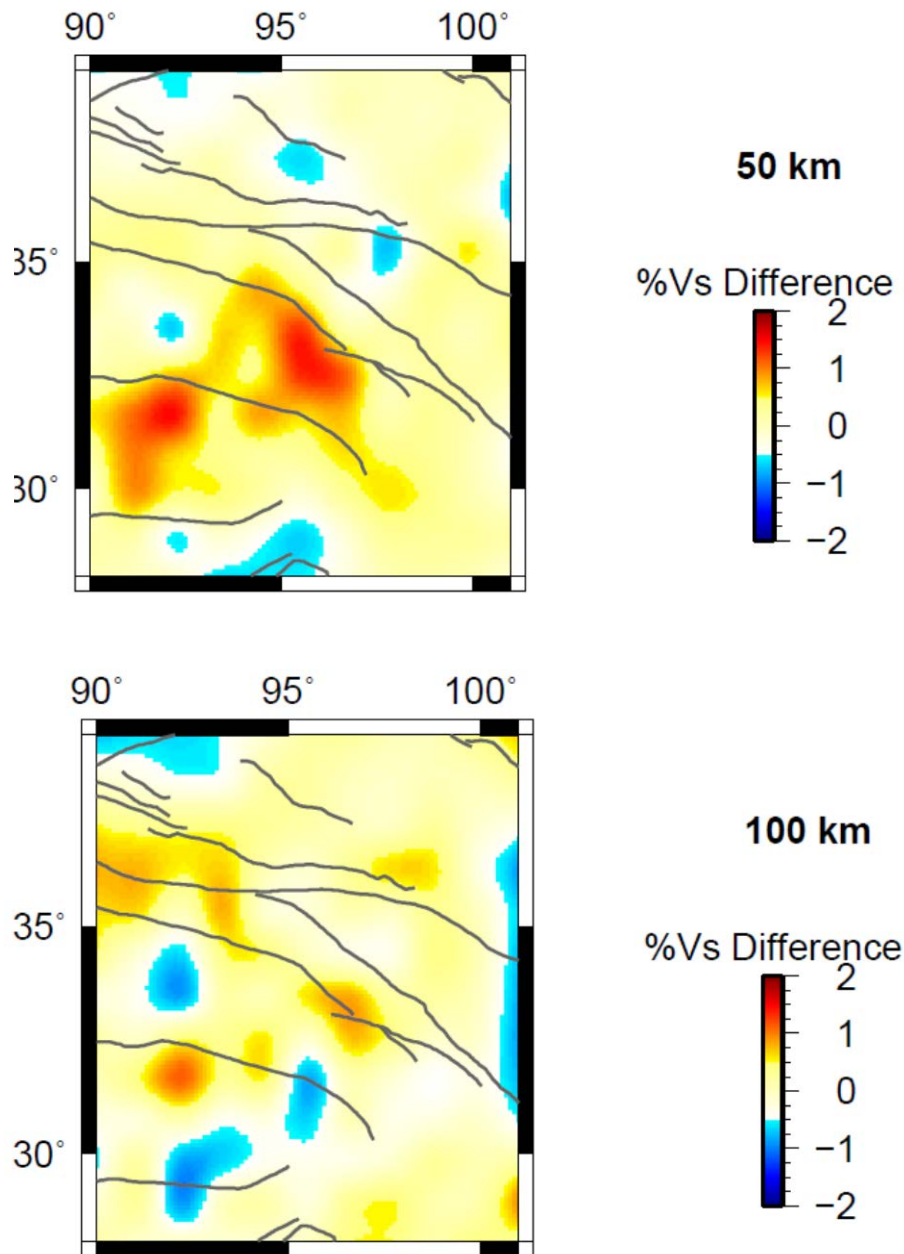


Figure 52. A rough quantitative comparison of the overlapping regions of the body and surface wave models of the shear wave velocity. *We normalized the velocity perturbations by the maximum percent change (negative or positive) and then subtracted the two normalized models to produce the contour maps.*

We compared different velocity models using different techniques to see which portions of the models are robust. We created three dimensional P and S wave velocity structure models for eastern Tibet using both finite frequency body wave tomography (not on this contract) and surface wave tomography (funded by this contract). In general the upper mantle, from the Main Frontal Thrust to central Tibet around 33°-34°N, exhibits laterally variable P- and S-wave velocity anomalies extending to at least 250 km in depth. Significant alternating low and high velocity anomalies are observed beneath southern Tibet, elongated in a north-south direction and extending to at least 150 km depth, possibly deeper. These studies confirm that low-velocity Tibetan crust ends abruptly at approximately 105 degrees longitude. These low velocity structures are consistent with measurements of low Lg and Pg Q values, indicating that these anomalies are a result of high temperatures and not just composition. The low velocities show a strong correlation with the strain rates computed from GPS and Quaternary fault data suggesting that strain heating plays some role in the generation of the lowest velocities. It is also important to note that neither the attenuation nor the velocity structure is symmetric with respect to the major sutures within Tibet, and overall we observe a much more complex velocity structure than previously thought.

Overall we observe a fairly strong correlation between the different features in our various seismic models for the eastern half of the Tibetan plateau. In order to test which parts of our models differ significantly we have attempted to do a direct comparison between the finite frequency S-wave travel time models and our surface wave velocity models. Direct comparison of these models is impossible because the finite frequency models only offer relative velocities while the surface wave models give us absolute velocity. Therefore we converted our surface wave models to a relative model and then normalized both of the models to either +1.0 or -1.0% depending upon which is larger. We then subtracted the two normalized relative S-wave velocity models and the results are shown in Figure 52. The largest differences between the two models occur at the Bangong Nujiang suture (BNS). It is important to note that we observe a steeply dipping high velocity anomaly in both body and surface wave model but the location of the anomalies is different.

Large two dimensional arrays in eastern Tibet have yielded a number of important results and the proliferation of seismic instrument pools in China offer a tremendous opportunity to further improve the resolution of three dimensional models within China. In particular large aperture, close spaced arrays of broadband stations across the margins of the Tibetan plateau should help to address fundamental questions about the different modes of deformation within the plateau.

5.2 Interpretation of the Pn and Sn Tomography

In general, the Pn and Sn velocity variation patterns are similar to those obtained in the model of the upper layer discussed above. High velocity values are observed beneath the Sichuan Basin and the Indian plate; low velocities are distributed under the Myanmar–Yunnan region, Hainan region, and the Songpan–Ganzi fold belt. Four independent data sets of the inversion of the Pn and Sn travel time data yielded similar results that are consistent with each other, and this confirms the credibility of the inversion results. A

previous study involving an SKS analysis revealed that the fast direction of the SKS north of 26° N is N–S and south of 26° N is W–E (Sol et al., 2007). In our model, there is a clear velocity difference between the southern and the northern parts of 26° N in the Yunnan region. Low velocities are found south of 26° N. Considering the previous SKS and Pn anisotropy results (Cui and Pei, 2009), we infer that the regions north and south of 26° N in the Yunnan region are controlled by different dynamic processes. The southern part is affected by the eastward subduction of the Indian plate and the northern part is affected by the material flow from the Tibetan Plateau (Zhang et al., 2011; Bai et al., 2010).

In eastern Tibet and throughout eastern China the average V_p/V_s ratio is approximately 1.76 beneath the study area (lower than the global average). The velocity ratio distributions are generally similar for the Pn and the Sn models. The velocity ratio is low in the Sichuan Basin. In the Myanmar–Yunnan and Hainan regions, the velocity ratio is quite high, indicating that the uppermost mantle has a high temperature. In the Yunnan region, there are some differences in the velocity ratio distributions between the two layers. From the heat flow observations (Wang and Huang, 1990; Hu et al., 2001) and crustal velocity structure studies (Gao et al., 2009; Wu and Zhang, 2012; Xu et al., 2012), we infer that the hot material upwelling is not vertical but is more complex beneath the Yunnan region, and the deeper layer is significantly affected by the hot material upwelling.

In the back-arc region around Myanmar, significant low Pn and Sn velocities were found to be distributed around volcanoes. This is strong evidence that the lithosphere of the Indian plate subducted into the mantle beneath Myanmar and caused the hot material upwelling at the back arc. The high temperature or even partial melting in the uppermost mantle caused the low velocity and the high V_p/V_s ratio. Surprisingly this is less than the global average for the uppermost mantle which is approximately 1.79. This number is similar to V_p/V_s ratios that are found in many subduction zones, suggesting that perhaps the mineralogy of the eastern Tibetan upper mantle is a result of the subduction of the Tethyan ocean in the Mesozoic.

The uppermost mantle velocities of the Sichuan Basin and the Songpan–Ganzi fold belt are quite different. The high Pn and Sn velocities of the Sichuan Basin imply that the lithosphere in this region is stable and cold, and thus the weaker and likely more ductile material beneath the Songpan Ganzi terranes flow moving to the south along the edge of the strong Sichuan basin lithospheric mantle. The low velocity in the Songpan–Ganzi region is consistent with that obtained in the previous studies. The very low V_p/V_s ratios beneath the Sichuan block is typical for many cratonic regions and can be attributed in part to a depleted lithospheric mantle.

There are significant velocity differences north and south of 26° N in the Yunnan region. From the SKS anisotropy result, we inferred that these parts were controlled by different dynamic processes. The southern part was affected by the eastward subduction of the Indian plate, and the northern part was affected by the material flow from the Tibetan

Plateau. The P_n and S_n velocities are low and the V_p/V_s ratio is high in the Hainan region, which offers further evidence of mantle plumes beneath the Hainan region. The differences in the velocity ratio distributions between the models of the two layers in the Yunnan region indicates that the hot material upwelling was not vertical but is more complex and the deeper layer was significantly affected by the hot material upwelling.

5.3 Q Tomography

Among various methods used to measure crustal Q, RTM appears to be the most reliable. Its RTS case does have the shortcoming that it is geometrically limited by the distribution of seismic stations, but this is improved by the RTE case, which makes RTM more practical to effectively map variations crustal Q using regional phases. The estimation of site terms using RTM in this study indicates that the site response is probably strongly dependent on topography and/or sedimentary thickness. The linear relationship between estimated logarithmic source terms and earthquake magnitudes M_L when $3 \leq M_L \leq 7$, shows that RTM Lg amplitude is applicable in accurately estimating earthquake magnitude. We create high-resolution (for $1^\circ \times 1^\circ$ to $2^\circ \times 2^\circ$ anomalies) Q_{Lg} and Q_{Pg} models of the eastern TP and adjacent areas using RTM in Q measurements and the LSQR algorithm in tomography. The Q_{Lg} and Q_{Pg} tomographic models show strong lateral variation in the eastern TP and adjacent areas. And low Q zones correlate with Cenozoic volcanic fields and active tectonics, which is circumstantial evidence that we are effectively isolating the path based attenuation of high frequency Lg and Pg waves.

Furthermore we measure significant azimuthal anisotropy of $1/Q_{Lg}$ within the eastern Tibetan Plateau using a reverse two-station/event method. Attenuation anisotropy appears to have similar orientations to the azimuthal velocity anisotropy measured using surface waves. A series of path-based $1/Q_{Lg}$ values are used to frame an inverse problem in order to solve for the frequency-dependent isotropic and anisotropic portions of $1/Q_{Lg}$. Resolution tests show that this model may retrieve anomalies as small as $2^\circ \times 2^\circ$. Anisotropic $1/Q_{Lg}$ is strong in the northwestern SGFB with the high-Q direction paralleling major strike-slip fault planes. This suggests that the crustal velocity and attenuation anisotropy have common origins. The very large azimuthally dependent fluctuations in $1/Q_{Lg}$ (Figure 35) suggest that for Lg propagation in Tibet, it is probably important to include an anisotropic component in all Q models in order to better predict high frequency amplitudes. These fluctuations are large enough to block Lg for some azimuths and propagate inefficiently for different path directions across the same part of Tibet. We have also assumed that the isotropic $1/Q_{Lg}$ is a result of intrinsic attenuation and scattering caused by randomly distributed scatterers and applied a model of Dainty (1981) to estimate the intrinsic attenuation of Q_{Lg} which is highly dependent on the temperature of the crust. The crustal temperature estimated for the Qiangtang terrane in this study corresponds with the results of previous studies. The northwestern corner of SGFB may have a high crustal temperature possibly resulting from strain heating of this strongly deforming flysch complex.

We also demonstrated that it is feasible to measure high frequency S_n Q using the RTM method. We showed that at least for Q the measurements are repeatable, especially for lower values of S_n Q (see Figure 48). However, for measuring the frequency dependence

our results are not as robust, suggesting we cannot constrain the frequency dependence for Q values larger than 1000. Based on the broadband seismograms from regional S_n waves, we determined an optimal tomographic S_n Q model of the uppermost mantle beneath NE China. When determining the Q values from regional phases, it is essential to eliminate the source response, site effects, radiation pattern, and instrument response. Although the TSM does not effectively remove relative site responses in Q values, it is widely utilized as the two stations give it a decided advantage over the single station methods and comparing with the RTM, it has fewer assumptions that may be violated. The RTM computes the most accurate Q values since it removes the site effect; however, the rigorous requirements for applying the RTM limits the scope of its application except when we have seismic networks such as the NECESS array.

The frequency dependence of Q is complicated and the power-law may be over simplified. Within a narrow frequency band, it may be an acceptable approximation. For our study, the S_n Q appears consistent with the η tomography. Negative η are shown near the high η ; this may be a result of the change of the waveguide shape and thus S_n attenuation is dominated by scattering. Our S_n Q tomography results show significant lateral variation in NE China, which may reflect the rheology in the uppermost mantle. The S_n Q values are relatively high in the Songliao basin, which suggests lower temperature and lower viscosity than in the surrounding area. The lower S_n Q values correspond with Quaternary volcanism. Our S_n Q model is consistent with previous shear wave velocity models at the Moho. The high Q regions correspond to the high velocity area and the low Q region corresponds to the low velocity area.

REFERENCES

- Bai, D., M. Unsworth, and M. Meju, (2010), Crustal deformation of the eastern Tibetan plateau revealed by magnetotelluric imaging, *Nature Geoscience*, 3, pp. 358-362, doi:10.1038/ngeo830.
- Bao, X., E. Sandvol, J. Ni, T. Hearn, Y. Chen, and Y. Shen (2011), High resolution regional seismic attenuation tomography in eastern Tibetan Plateau and adjacent regions, *Geophys. Res. Lett.*, doi: 10.1029/2011GL048012, in press.
- Bendick, R. and L. Flesch, (2007), Reconciling lithospheric deformation and lower crustal flow beneath central Tibet, *Geology*, **35**, pp. 895-898, doi:10.1130/G23714A.1.
- Bostock, M. G. and B. L. N. Kennett (1990), The effect of 3-D structure on Lg propagation patterns, *Geophys. J. Int.*, 101, pp. 355-365.
- Burchfiel, B. C., Q. Deng, P. Molnar, L. Royden, Y. Wang, P. Zhang, and W. Zhang (1989), Intracrustal detachment within zones of continental deformation *Geology*, **17**, pp. 748-752.
- Chapman, M. (2009), Modelling the effect of multiple sets of mesoscale fractures in porous rock on frequency-dependent anisotropy, *Geophysics*, 74, pp. D97-D103, doi: 10.1190/1.3204779.
- Chichinina, T., V. Sabinin, and G. Ronquillo-Jarillo (2006), QVOA analysis: *P*-wave attenuation anisotropy for fracture characterization, *Geophysics*, 71, pp. C37-C48, doi: 10.1190/1.2194531.
- Chichinina, T., I. Obolentseva, L. Gik, B. Bobrov, and G. Ronquillo-Jarillo (2009), Attenuation anisotropy in the linear-slip model: Interpretation of physical modeling data, *Geophysics*, 74, pp. WB165-WB176, doi: 10.1190/1.3173806.
- Chun, K.-Y., G. F. West, R. J. Kokoski, and C. Samson (1987), A novel technique for measuring *Lg* attenuation; results from Eastern Canada between 1 to 10 Hz, *Bull. Seismo. Soc. Amer.*, **77**, pp. 398-419.
- Cowgill, E., A. Yin, T. M. Harrison, and X. F. Wang (2003), Reconstruction of the Altyn Tagh fault based on U–Pb geochronology: role of back thrusts, mantle sutures, and heterogeneous crustal strength in forming the Tibetan Plateau, *J. Geophys. Res.* **108**(B7), p. 2346.
- Cotte, N., H. Pedersen, M. Campillo, J. Mars, J. F. Ni, R. Kind, E. Sandvol, and W. Zhao (1999), Determination of the crustal structure in southern Tibet by dispersion and amplitude analysis of Raleigh waves, *Geophys. J. Int.*, **138**, pp. 809-819.
- Cui, Z. and S. Pei (2009), Study on Pn velocity and anisotropy in the uppermost mantle of the Eastern Himalayan Syntaxis and surrounding regions. *Chinese J. Geophys.*, 52(9), pp. 2245-2254.
- Dainty, A. M. (1981), A scattering model to explain seismic Q observations in the lithosphere between 1 and 30 Hz, *Geophys. Res. Lett.*, 8, pp. 1126-1128.
- Der, Z. A., W. D. Rivers, T. W. McElfresh, A. O'Donnell, P. J. Klouda, and M. E. Marshall (1982), Worldwide variations in the attenuative properties of the upper mantle as determined from spectral studies of short-period body waves, *Physics of the Earth and Planetary Interiors*, 30 (1), pp. 12-25.

- Fan, G. W. and T. Lay (2003), Strong Lg wave attenuation in the Northern and Eastern Tibetan Plateau measured by a two-station/two-event stacking method, *Geophys. Res. Lett.*, **30**, doi:10.1029/2002GL016211.
- Fisk, M. D. (2006), Source spectral modeling of regional P/S discriminants at nuclear test sites in China and the Former Soviet Union, *Bull. Seism. Soc. Am.* **96**, pp. 2348-2367.
- Fisk, M. D. (2007), Corner frequency scaling of regional seismic phases for underground nuclear explosions at the Nevada Test Site, *Bull. Seism. Soc. Am.* **97**, pp. 977-988.
- Fisk, M. D., S. R. Taylor, H. J. Patton, and W. R. Walter (2008), Applications of a next-generation MDAC discrimination procedure using two-dimensional grids of regional P/S spectral ratios, proceedings of the 2008 Monitoring Research Review.
- Forsyth, D. W. and A. Li (2005), Array Analysis of Two-Dimensional Variations in Surface Wave Phase Velocity and Azimuthal Anisotropy in the Presence of Multipathing Interference, in *Seismic Earth: Array Analysis of Broadband Seismograms*, edited by A. Lavander and G. Nolet, AGU, Washington DC.
- Forsyth, D. W., S. C. Webb, L. M. Dorman, and Y. Shen (1998), Phase velocities of Rayleigh waves in the MELT experiment on the East Pacific Rise. *Science*, **280**, pp. 1235-1238.
- Furumura, T. and B. L. N. Kennett (1997), On the nature of regional seismic phases-II. On the influence of structural barriers, *Geophys. J. Int.*, 129, pp. 221-234.
- Galve, A., M. Sapin, A. Hirn, J. Diaz, J.-C. Lépine, M. Laigle, J. Gallart, and M. Jiang (2002), Complex images of Moho and variation of Vp/Vs across the Himalaya and South Tibet, from a joint receiver-function and wide-angle-reflection approach, *Geophysical Research Letters* 29 (24).
- Gao, X., Y. Su, W. Wang, S. Pei, and Z. Guo (2009), Lower-crust S-wave velocity beneath western Yunnan Province from waveform inversion of dense seismic observations, *Terra Nova*, 21, pp. 105-110.
- Hasegawa, H. S. (1985), Attenuation of Lg waves in the Canadian shield, *Bull. Seismol. Soc. Am.*, 75, pp. 1569-1582.
- Han, Y., et al. (2012), Lithospheric and upper mantle structure of the northeastern Tibetan Plateau, *J. Geophys. Res.*, 117(B5), B05307, doi:10.1029/2011jb008545.
- Hacker, B. R., E. Gnos, L. Ratschbacher, M. Grove, M. McWilliams, S. W. Sobolev, J. Wan, and Z. Wu, (2000), Hot and dry deep crustal xenoliths from Tibet, *Science*, **287**, pp. 2463-2466.
- Hearn, T. M. and R. W. Clayton (1986), Lateral velocity variations in southern California, *Bull. Seismol. Soc. Am.*, 76, pp. 495-509.
- Hearn, T. and J. Ni, (1994), Pn velocities beneath continental collision zones, the Turkish-Iranian plateau, *Geophys. J. Int.*, 117, pp. 273-283.
- Hearn, T. M. (1996), Anisotropic Pn tomography in the western United States, *J. Geophys. Res.*, 101, pp. 8403-8414.
- Hearn, T., S. Wang, J. Ni, Z. Xu, Y. Yu, and X. Zhang (2004), Uppermost mantle velocities beneath China and surrounding regions, *J. Geophys. Res.*, 109, B11301, doi:10.1029/2003JB002874.

- Hearn, T. M., S. Wang, S. Pei, Z. Xu, J. Ni, and Y. Yu (2008), Seismic amplitude tomography for crustal attenuation beneath China, *Geophys. J. Int.*, **174**, pp. 223-234, doi: 10.1111/j.1365-246X.2008.03776.x.
- Hearn, T. M. (2008), Surface-wave attenuation from ISC Bulletin data, presented at 2008 SSA meeting, *Seismological Research Letters*, **79**, p. 339, Meeting Abstract.
- Herrmann, R. B. and A. Kijko (1983), Modeling some empirical vertical component Lg relations, *Bull. Seismol. Soc. Am.*, **73**, pp. 157-171.
- Holt, W. E., N. Chamot-Rooke, X. Le Pichon, A. J. Haines, B. Shen-Tu, and J. Ren (2000), Velocity field in Asia inferred from Quaternary fault slip rates and Global Positioning System observations, *J. Geophys. Res.*, **105**, pp. 19,185-19,209.
- Hu, S., L. He, and J. Wang (2001), Compilation of heat flow data in the China continental area (3rd edition), *Chinese J. Geophys.*, **44**(5), pp. 611-626.
- Hung, S.-H., F. A. Dahlen, and G. Nolet (2001), Wavefront healing: a banana-doughnut perspective, *Geophys. J. Int.*, **146**, pp. 289-312.
- Huang, W.-C., et al. (2000), Seismic polarization anisotropy beneath the central Tibetan Plateau, *Journal of Geophysical Research*, **105**(B12), pp. 27,979-27,989.
- Huang, J. and Zhao D. (2006), High-resolution mantle tomography of China and surrounding regions, *J. Geophys. Res.*, **111**, B09305, doi:10.1029/2005JB004066.
- Huang, Z., W. Su, Y. Peng, Y. Zheng, and H. Li (2003), Rayleigh wave tomography of China and adjacent regions, *J. Geophys. Res.*, **108** (2), pp. ESE 4-1-4-14.
- Huang, M.-W., J.-H. Wang, H.-H. Hsieh, K.-L. Wen, and K.-F. Ma (2005), Frequency-dependent sites amplifications evaluated from well-logging data in central Taiwan, *Geophys. Res. Lett.*, **32**, L21302, doi:10.1029/2005GL023527.
- Jemberie, A. L. and A. A. Nyblade (2009), Intrinsic and scattering Q near 1 Hz across the East African Plateau, *Bull. Seismol. Soc. Am.*, **99**, pp. 3516-3524, doi:10.1785/0120090062.
- Jin, A., K. Mayeda, D. Adams, and K. Aki (1994), Separation of intrinsic and scattering attenuation in southern California using TERRAScope data, *J. Geophys. Res.*, **99**, pp. 17,835-17,848.
- Julia, J., C. Ammon, R. Herrman, and A. Correig (2000), Joint inversion of receiver function and surface wave dispersion observations, *Geophys. Jour. Int.*, **143**, pp. 99-112.
- Karplus, M. S., W. Zhao, S. L. Klemperer, Z. Wu, J. Mechie, D. Shi, L. D. Brown, and C. Chen (2011), Injection of Tibetan crust beneath the south Qaidam Basin: Evidence from INDEPTH IV wide-angle seismic data, *J. Geophys. Res.*, **116**, B07301, doi: 10.1029/2010JB007911.
- Kennett, B. L. N. (1986), Lg waves and structural boundaries, *Bull. Seismol. Soc. Am.*, **76**, pp. 1133-1141.
- Kennett, B. L. N. (1989), On the nature of regional seismic phases-I. Phase representations for Pn, Pg, Sn, Lg, *Geophys. J. Int.*, **98**, pp. 447-456.
- Kind, R., X. Yuan, J. Saul, D. Nelson, S. V. Sobolev, J. Mechie, W. Zhao, G. Kosarev, J. Ni, U. Achauer, and, M. Jiang (2002), Seismic images of crust and upper mantle beneath Tibet: Evidence for Eurasian plate subduction, *Science*, **298**, pp. 1219-1221.
- Knopoff, L., F. Schwab, and E. Kauselt (1973), Interpretation of Lg, *Geophys. J. R. Astron. Soc.*, **33**, pp. 389-404.

- Kumar, P., X. Yuan, R. Kind, and J. Ni (2006), Imaging the colliding Indian and Asian lithospheric plates beneath Tibet, *Jour. Geophys. Res.*, **111**, B06308, DOI:10.1029/2005JB003930.
- Langin, W. R., L. D. Brown, E. A. Sandvol, and Project INDEPTH Team (2003), Seismicity of central Tibet from INDEPTH III seismic recordings, *Bull. Seismol. Soc. Amer.*, **93**, pp. 2146-2159.
- León Soto, G., E. Sandvol, J. F. Ni, L. Flesch, T. M. Hearn, F. Tilmann, J. Chen, and L. D. Brown (2012), Significant and vertically coherent seismic anisotropy beneath eastern Tibet, *J. Geophys. Res.*, **117**(B5), B05308, doi:10.1029/2011jb008919.
- Lei, J., D. Zhao, and Y. Su (2009a), Insight into the origin of the Tengchong intraplate volcano and seismotectonics in southwest China from local and teleseismic data, *J. Geophys. Res.*, **114**, B05302, doi:10.1029/2008JB005881.
- Lei, J., D. Zhao, B. Steinberger, B. Wu, F. Shen, and Z. Li (2009b), New seismic constraints on the upper mantle structure of the Hainan plume, *Physics of the Earth and Planetary Interiors*, **173**, pp. 33-50.
- Li, A. (2011), Shear wave model of southern Africa from regional Rayleigh wave tomography with 2-D sensitivity kernels, *Geophysical Journal International*, **185**(2), pp. 832-844, doi:10.1111/j.1365-246X.2011.04971.x.
- Li, C., R. D. Van der Hilst, A. S. Meltzer, R. Sun, and E. R. Engdahl (2008), Subduction of the Indian lithosphere beneath the Tibetan Plateau and Burma, *Earth and Planetary Science Letters*, **274**, pp. 157-168.
- Li, Y., Q. Wu, F. Zhang, Q. Feng, and R. Zhang (2011), Seismic anisotropy of the Northeastern Tibetan Plateau from shear wave splitting analysis, *Earth Planet. Sci. Lett.*, **304**, pp. 147-157, doi: 10.1016/j.epsl.2011.01.026.
- Liang, C., X. Song, and J. Huang (2004), Tomographic inversion of Pn travel times in China, *J. Geophys. Res.*, **109**, B11304, doi:10.1029/2003JB002789.
- Liang, X., E. Sandvol, Y. J. Chen, T. Hearn, J. Ni, S. Klemperer, Y. Shen, and F. Tilmann (2012), A complex Tibetan upper mantle: A fragmented Indian slab and no south-verging subduction of Eurasian lithosphere, *Earth and Planetary Science Letters*, **333-334**, pp. 101-111, doi:10.1016/j.epsl.2012.03.036.
- Ligorria, J. and C. Ammon (1999), Iterative deconvolution and receiver-function estimation, *B Seismol Soc Am*, **89**(5), p. 1395.
- Liu, J., J. Han, and W. S. Fyfe (2001), Cenozoic episodic volcanism and continental rifting in northeast China and possible link to Japan Sea development as revealed from K-Ar geochronology, *Tectonophysics*, **339**, pp. 385-401.
- Liu, Y., T.-L. Teng, Y. Ben-Zion (2005), Near-surface seismic anisotropy, attenuation and dispersion in the aftershock region of the 1999 Chi-Chi earthquake, *Geophys. J. Int.*, **160**, pp. 695-706, doi: 10.1111/j.1365-246X.2005.02512.x.
- Lü, Y., B. Liu, S. Pei, Y. Sun, M. Toksöz, and X. Zeng (2012), Pn tomographic velocity and anisotropy beneath the Iran region, *Bull. Seis. Soc. Am.*, **102**(1), pp. 426-435, doi: 10.1785/0120100141.
- Makovsky, Y. and S. Klemperer (1999), Measuring the Seismic Properties of Tibetan Bright Spots: Evidence for Free Aqueous Fluids in the Tibetan Middle Crust, *J. Geophys. Res.*, **104**, pp. 10795-10825.
- McNamara, D. E., T. J. Owens, and W. R. Walter (1996), Propagation characteristics of Lg across the Tibetan Plateau, *Bull. Seismol. Soc. Am.*, **86**, pp. 457-469.

- McNamara, D. E., W. R. Walter, T. J. Owens, and C. J. Ammon (1997), Upper mantle velocity structure beneath the Tibetan Plateau from Pn travel time tomography, *Journal of Geophysical Research*, 102(B1), pp. 493-505, doi:10.1029/96JB02112.
- Mitchell, B. J. and H. J. Hwang (1987), Effect of low Q sediments and crustal Q on Lg attenuation in the United States, *Bull. Seismol. Soc. Am.*, 77, pp. 1197-1210.
- Mitchell, B. J. (1995), Anelastic structure and evolution of the continental crust and upper mantle from seismic surface wave attenuation, *Rev. Geophys.*, 33, pp. 441-462.
- Mitchell, B. (1997), Lg coda Q variation across Eurasia and its relation to crustal evolution, *J. Geophys. Res* 102, pp. 22,767-22,779.
- Montagner, J.-P. and H.-C. Nataf (1986), A simple method for inverting the azimuthal anisotropy of surface waves, *J. Geophys. Res.*, 91, pp. 511-520.
- Nábělek, J., G. Hetényi, J. Vergne, S. Sapkota, B. Kafle, M. Jiang, H. Su, J. Chen, B.-S. Huang, and the Hi-CLIMB Team (2009), Underplating in the Himalaya-Tibet collision zone revealed by the Hi-CLIMB experiment, *Science*, 325, pp. 1371-1374, doi: 10.1126/science.1167719.
- Nelson K. D. and 28 others (1996), Partially molten middle crust beneath southern Tibet; synthesis of Project INDEPTH results, *Science* 274, pp. 1684-1688.
- Ni, J. and M. Barazangi (1983), High-frequency seismic wave propagation beneath the Indian Shield, Himalayan Arc, Tibetan Plateau and surrounding regions: High uppermost mantle velocities and efficient SN propagation beneath Tibet, *Geophys. J. Royal Astron. Soc.*, 72, pp. 665-689.
- Nolet, G. and F. A. Dahlen (2000), Wave front healing and evolution seismic delay times, *Journal of Geophysical Research*, 105(B8), pp. 19,043-19,054.
- Nuttli, O. W. (1986), Yield estimates of Nevada test site explosions obtained from seismic Lg waves, *J. Geophys. Res.*, 91, pp. 2137-2151.
- Ozacar, A. A. and G. Zandt (2004), Crustal seismic anisotropy in central Tibet: Implications for deformational style and flow in the crust, *Geophys. Res. Lett.*, 31, L23601, doi: 10.1029/2004GL021096.
- Paige, C. C. and M. A. Saunders (1982), LSQR: An algorithm for sparse linear equations and sparse least squares, *ACM Trans Math. Softw.*, 8, pp. 43-71.
- Pasyanos, M. E., E. M. Matzel, W. R. Walter, and A. J. Rodgers (2009), Broad-band Lg attenuation modeling in the Middle East, *Geophys. J. Int.*, 177, pp. 1166-1176, doi:10.1111/j.1365-246X.2009.04128.x.
- Pasyanos, M. E. (2010), Lithospheric thickness modeled from long-period surface wave dispersion, *Tectonophysics*, 481 (1-4), pp. 38-50.
- Pei, S., et al., (2007). Upper mantle seismic velocities and anisotropy in China determined through Pn and Sn tomography, *J. Geophys. Res.*, 112, B05312, doi:10.1029/2006JB004409.
- Phillips, W. S., H. E. Hartse, S. R. Taylor, and G. E. Randall (2000), 1 Hz Lg Q Tomography in central Asia, *Geophys. Res. Lett.*, 27, pp. 3425-3428.
- Phillips, W. S., H. E. Hartse, S. R. Taylor, A. A. Velasco, and G. E. Randall (2001), Application of regional phase amplitude tomography to seismic verification, *PAGEOPH*, 158, pp. 1189-1206.
- Phillips, W.S., H. E. Hartse, and J. T. Rutledge (2005), Amplitude ratio tomography for regional phase Q, *Geophys. Res. Lett.*, 32, doi:10.1029/2005GL023870.

- Rapine, R. and J. F. Ni (2003a), Propagation characteristics of Sn and Lg in Northern China and Mongolia, *Bull. Seism. Soc. Am.*, 93, pp. 939-945.
- Rapine, R., F. Tilmann, M. West, J. Ni, and A. Rodgers (2003b), Crustal structure of northern and southern Tibet from a surface wave dispersion analysis, *J. Geophys. Res.*, 108, pp. 2120, doi:10.1029/2001JB000445.
- Reese C., R. Papine, and J. Ni (1999), Lateral variation of Pn and Lg attenuation at the CDSN station LSA, *Bull. Seism. Soc. Am.*, 89, pp. 325-330.
- Rodgers, A. R., J. F. Ni, and T. M. Hearn (1997), Propagation Characteristics of Short-Period Sn and Lg in the Middle East, *Bull. Seism. Soc. Am.* **87**, pp. 396-413.
- Rodgers, A., H. Tkalcic, D. McCallen, S. Larsen, and C. Snelson (2006), Site response in Las Vegas Valley, Nevada from NTS explosions and earthquake data, *Pure and Applied Geophysics*, 163 (1), pp. 55-80.
- Roger, F., M. Jolivet, and J. Malavieille (2010), The tectonic evolution of the Songpan-Garzê (North Tibet) and adjacent areas from Proterozoic to Present: A synthesis, *J. Asian Earth Sci.*, 39, pp. 254-269, doi: 10.1016/j.jseaes.2010.03.008.
- Sandvol, E., K. Al-Damegh, A. Calvert, D. Seber, M. Barazangi, R. Mohamad, R. Gok, N. Turkelli, and C. Gurbuz (2001), Tomographic imaging of Lg and Sn propagation in the Middle East, *Pure and Applied Geophysics*, 158, pp. 1121-1163.
- Saito, M. (1988), *DISPER80: A subroutine package for the calculation of seismic normal-mode solutions*, Elsevier, New York.
- Sarker, G. and G. A. Abers (1998), Comparison of seismic body wave and coda wave measures of Q, *Pure Appl. Geophys.*, 153, pp. 665-683.
- Smith, M. L. and F. A. Dahlen (1973), The azimuthal dependence of Love and Rayleigh wave propagation in a slightly anisotropic medium, *J. Geophys. Res.*, 78, pp. 3321-3333.
- Snieder, R. (1986), 3D Linearized scattering of surface waves and a formalism for surface wave holography, *Geophys. J. R. Astron. Soc.*, 84, pp. 581-605.
- Sol, S., A. Meltzer, and R. Burgmann (2007), Geodynamics of the southeastern Tibetan Plateau from seismic anisotropy and geodesy, *Geology*, 35(6), pp. 563-566.
- Steck, L. K., W. S. Phillips, K. Mackey, M. L. Begnaud, R. J. Stead, and C. A. Rowe (2009), Seismic tomography of crustal P and S across Eurasia, *Geophys. J. Int.*, 177, pp. 81-92, doi:10.1111/j.1365-246X.2009.04109.x.
- Su, W., C. Wang, and Z. Huang (2008), Azimuthal anisotropy of Rayleigh waves beneath the Tibetan Plateau and adjacent areas, *Sci. China D*, 51, pp. 1717-1725, doi: 10.1007/s11430-008-0137-x.
- Suetsugu, D., and I. Nakanishi (1985), Tomographic inversion and resolution for Rayleigh wave phase velocities in the Pacific Ocean, *J. Phys. Earth*, 33, 345-368.
- Tapponnier, P., Z. Xu, F. Roger, B. Meyer, N. Arnaud, G. Wittlinger, and J. Yang (2001), Oblique stepwise rise and growth of the Tibet plateau, *Science* 294, pp. 1671-1677.
- Taylor, M. and A. Yin (2009), Active structures of the Himalayan-Tibetan orogen and their relationships to earthquake distribution, contemporary strain field, and Cenozoic volcanism, *Geosphere*, 5, pp. 199-214, doi: 10.1130/GES00217.1.
- Tilmann, F., J. Ni, and INDEPTH III Seismic Team (2003), Seismic imaging of the downwelling Indian lithosphere beneath central Tibet, *Science*, 300, pp. 1424-1427.

- Vergne, J., G. Wittlinger, Q. Hui, P. Tapponnier, G. Poupinet, M. Jiang, G. Herquel, and A. Paul (2002), Seismic evidence for stepwise thickening of the crust across the NE Tibetan plateau, *Earth Planet. Sci. Lett.*, 203, pp. 25-33, doi: 10.1016/S0012-821X(02)00853-1.
- Vergne, J., G. Wittlinger, V. Farra, and H. Su (2003), Evidence for upper crustal anisotropy in the Songpan-Ganze (northeastern Tibet) terrane, *Geophys. Res. Lett.*, 30, p. 1552, doi: 10.1029/2002GL016847.
- Wald, D. J. and T. I. Allen (2007), Topographic slope as a proxy for seismic site conditions and amplification, *Bull. Seismol. Soc. Am.*, 97, pp. 1379-1395, doi:10.1785/0120060267.
- Walter, W. and S. Taylor (2002), A revised Magnitude Distance Amplitude Correction (MDAC2) procedure for regional seismic discriminants, Lawrence Livermore National Laboratory UCRL-ID-146882.
- Wang, J. and S. Huang (1990), Compilation of heat flow data in the China continental area (2nd edition), *Seismology and Geology*, 12(4), pp. 351-366.
- Wang, Q. and M. P. Coward (1990), The Chaidam basin (northwest China): Formation and hydrocarbon potential: *Journal of Petroleum Geology*, v. 13, p. 93-112.
- Wang, C.-Y., L. M. Flesch, P. G. Silver, L.-J. Chang, and W. W. Chan (2008), Evidence for mechanically coupled lithosphere in central Asia and resulting implications, *Geology*, 36, pp. 363-366, doi: 10.1130/G24450A.1.
- Wang, C.-Y., W. D. Mooney, Z. Ding, J. Yang, Z. Yao, and H. Lou (2009), Shallow seismic structure of Kunlun fault zone in northern Tibetan Plateau, China: implications for the 2001 Ms8.1 Kunlun earthquake, *Geophys. J. Int.*, 2009, 177, pp. 978-1000, doi: 10.1111/j.1365-246X.2009.04049.x.
- Wang, Q., P.-Z. Zhang, J. T. Freymueller, R. Bilham, K. M. Larson, X. Lai, X. You, Z. Niu, J. Wu, Y. Li, J. Liu, Z. Yang, and Q. Chen (2001), Present-day crustal deformation in China constrained by Global Positioning System measurements, *Science*, 294, pp. 574-577, doi: 10.1126/science.1063647.
- Wei, W., M. Unsworth, A. Jones, J. Booker, H. Tan, K. D. Nelson, L. Chen, S. Li, K. Solon, P. Bedrosian, S. Jin, M. Deng, J. Ledo, D. Kay, and B. Roberts (2001), Detection of widespread fluids in the Tibetan crust by magnetotelluric studies, *Science* 292, pp. 716-718.
- Werner, U. and S. A. Shapiro (1998), Intrinsic anisotropy and thin multilayering-two anisotropy effects combined, *Geophys. J. Int.*, 132, pp. 363-373.
- Wittlinger, G., F. Masson, G. Poupinet, P. Tapponnier, J. Mei, G. Herquel, J. Guilbert, U. Achauer, X. Guanqi, D. Shi, and Lithoscope Kunlun Team (1996), Seismic tomography of northern Tibet and Kunlun: Evidence for crustal blocks and mantle velocity contrasts, *Earth. Planet. Sci. Letters*, **139**, pp. 263-279.
- Wu, X.-Y. and R.-S. Wu (2001), Lg-wave simulation in heterogeneous crusts with surface topography using screen propagators, *Geophys. J. Int.*, 146, pp. 670-678.
- Wu, J. and Z. Zhang (2012), Spatial distribution of seismic layer, crustal thickness, and Vp/Vs ratio in the Permian Emeishan Mantle Plume region, *Gondwana Research*, 22: pp. 127-139.
- Xie, J. and B. J. Mitchell (1990), A back-projection method for imaging large-scale lateral variations of Lg coda Q with application to continental Africa, *Geophys. J. Int.*, 100, pp. 161-181.

- Xie, J. (2002a), Lg Q in the Eastern Tibetan Plateau, *Bull. Seism. Soc. Am.*, **92**, pp. 871-876.
- Xie, J. (2002b), Source scaling of Pn, Lg spectra and their ratios from explosions in central Asia: Implications on identification of small seismic events at regional distances, *J. Geophys. Res.*, **107**(B7), 10.1029/2001JB000509.
- Xie, J., R. Gök, J. Ni, and Y. Aoki (2004), Lateral variations of crustal seismic attenuation along the INDEPTH profiles in Tibet from Lg Q inversion, *J. Geophys. Res.*, **109**, B10308, doi:10.1029/2004JB002988.
- Xie, J., Z. Wu, R. Liu, D. Schaff, Y. Liu, and J. Liang (2006), Tomographic regionalization of crustal Lg Q in eastern Eurasia, *Geophys. Res. Lett.*, **33**, L03315, doi:10.1029/2005GL024410.
- Xu, Y., X. Yang, Z. Li, and J. Liu (2012), Seismic structure of the Tengchong volcanic area southwest China from local earthquake tomography, *Journal of Volcanology and Geothermal Research*.
- Yang, Y., and D. Forsyth (2006), Regional tomographic inversion of the amplitude and phase of Rayleigh waves with 2-D sensitivity kernels, *Geophysical Journal International* **166** (3), pp. 1148-1160.
- Yang, Y., Y. Zheng, J. Chen, S. Zhou, S. Ceylan, E. Sandvol, F. Tilmann, K. Priestley, T. M. Hearn, J. F. Ni, L. D. Brown, and M. H. Ritzwoller (2010), Rayleigh wave phase velocity maps of Tibet and the surrounding regions from ambient seismic noise tomography, *Geochem. Geophys. Geosyst.*, **11**, Q08010, doi: 10.1029/2010GC003119.
- Yao, H., R. D. van der Hilst, and J.-P. Montagner (2010), Heterogeneity and anisotropy of the lithosphere of SE Tibet from surface wave array tomography, *J. Geophys. Res.*, **115**, B12307, doi: 10.1029/2009JB007142.
- Yao, Z., R. Roberts, and A. Tryggvason (1999), Calculating resolution and covariance matrices for seismic tomography with the LSQR method, *Geophys. J. Int.*, **138**, pp. 886-894.
- Yi, G., H. Yao, J. Zhu, and R. D. van der Hilst (2010), Lithospheric deformation of continental China from Rayleigh wave azimuthal anisotropy, *Chinese J. Geophys.*, **53**, pp. 256-268, doi: 10.3969/j.issn.0001-5733.2010.02.004.
- Yin, An, Yu-Qi Dang, M. Zhang, Xuan-Hua Chen, and M. W. McRivette (2008), Cenozoic tectonic evolution of the Qaidam basin and its surrounding regions (part3): structural geology, sedimentation, and regional tectonic reconstruction, *GSA Bulletin*, **120**, pp. 847-876, doi: 10.1130/B26232.1.
- Yin, A. (2010), Cenozoic tectonic evolution of Asia: a preliminary synthesis, *Tectonophysics*, **488**, pp. 293-325, doi:10.1016/j.tecto.2009.06.002.
- Yuan, X., J. Ni, R. Kind, E. Sandvol, and J. Mechie (1997), Lithospheric and upper mantle structure of southern Tibet from a seismological passive source experiment, *J. Geophys. Res.*, **102**, B 12, pp. 27491-27500.
- Zelt, C. A. (1998), Lateral velocity resolution from three-dimensional seismic refraction data, *Geophys. J. Int.*, **135**, pp. 1101-1112.
- Zhao, C., B. L. N. Kennett, and T. Furumura (2003), Contrasts in regional seismic wave propagation to station WMQ in central Asia, *Geophys. J. Int.*, **155**, pp. 44-56, doi: 10.1046/j.1365-246X.2003.02000.x.

- Zhao, W., et al. (2011), Tibetan plate overriding the Asian plate in central and northern Tibet, *Nature Geosci*, 4(12), pp. 870-873, doi:10.1038/NGEO1309.
- Zhang, T. and T. Lay (1994), Analysis of short-period regional phase path effects associated with topography in Eurasia, *Bull. Seismol. Soc. Am.*, 84, pp. 119-132.
- Zhang, Z., X. Yuan, Y. Chen, X. Tian, R. Kind, X. Li, and J. Teng (2010), Seismic signature of the collision between the east Tibetan escape flow and the Sichuan Basin, *Earth. Planet. Sci. Lett.*, 292, pp. 254-264, doi:10.1016/j.epsl.2010.01.046.
- Zhang, Z., S. Klemperer, Z. Bai, Y. Chen, and J. Teng (2011), Crustal structure of the Paleozoic Kunlun orogeny from an active-source seismic profile between Moba and Guide in East Tibet, China, *Gondwana Research*, 19(4), pp. 994-1007.
- Zheng, Y., W. Shen, L. Zhou, Y. Yang, Z. Xie, and M. H. Ritzwoller (2011), Crust and uppermost mantle beneath the North China Craton, northeast China, and the Sea of Japan from ambient noise tomography, *J. Geophys. Res.*, 116, B12312.
- Zhou, Y., F. A. Dahlen, and G. Nolet (2004), Three-dimensional sensitivity kernels for surface wave observables, *Geophysical Journal International*, 158(1), pp. 142-168, doi:10.1111/j.1365-246X.2004.02324.x.
- Zhou, H. and M. Murphy (2005), Tomographic evidence for wholesale underthrusting of India beneath the entire Tibetan plateau, *Journal of Asian Earth Sciences*, 25(3), pp. 445-457, doi:10.1016/j.jseaes.2004.04.007.
- Zhu, L. and D. V. Helmberger (1998), Moho Offset Across the Northern Margin of the Tibetan Plateau, *Science*, **281**, pp. 1170-1172.
- Zhu, Y., and I. Tsvankin (2006), Plane-wave propagation in attenuative transversely isotropic media, *Geophysics*, 71, T17-T30, doi: 10.1190/1.2187792.
- Zor, E., E. Sandvol, J. Xie, N. Türkelli, B. Mitchell, A. Gasanov, and G. Yetirmishli (2007), Crustal Attenuation within the Turkish Plateau and Surrounding Regions, *Bull. Seism. Soc. Am.*, 97, pp. 151-161; DOI: 10.1785/0120050227.

LIST OF SYMBOLS, ABBREVIATIONS, AND ACRONYMS

RTM	Reverse Two Station Method
TSM	Two Station Method
TPWP	Two Plane Wave
TPWT	Two Plate Wave Tomography
TP	Tibetan Plateau
NKF	Norhtern Kunlun Fault zone
SKF	Southern Kunlun Fault zone
SGT	Songpan Ganzi Terrane
GPS	Global Positioning System
SKF	Southern Kunlun Fault zone
QT	Qiangtang Terrane
BNS	Bangong Nujiang Suture
JS	Jinsha Suture

DISTRIBUTION LIST

DTIC/OCP 8725 John J. Kingman Rd, Suite 0944 Ft Belvoir, VA 22060-6218	1 cy
AFRL/RVIL Kirtland AFB, NM 87117-5776	2 cys
Official Record Copy AFRL/RVBYE/Robert Raistrick	1 cy